Mitigating Wall Interference in Transonic Wind Tunnel Testing of Swept Wings

A Numerical Study on Flowfield Correction Using Wall Deformation in the Cryogenic Ludwieg Tube Göttingen

Tobias Dolipski

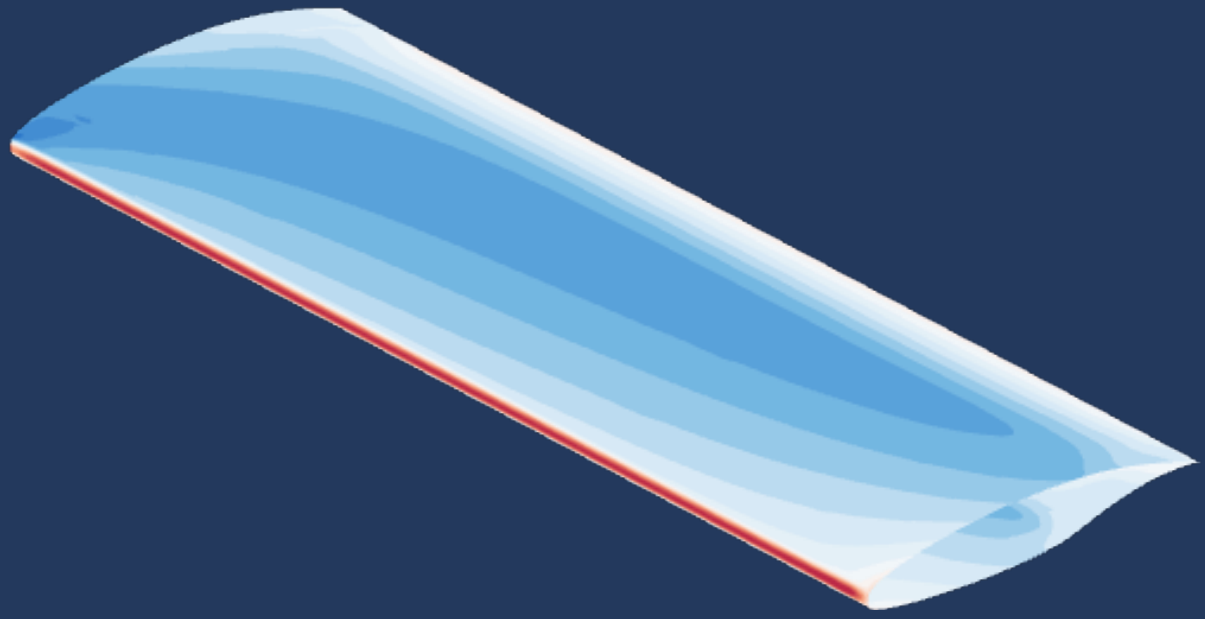

TU Delft

Mitigating Wall Interference in Transonic Wind Tunnel Testing of Swept Wings

A Numerical Study on Flowfield Correction Using Wall Deformation in the Cryogenic Ludwieg Tube Göttingen

Thesis report

by

Tobias Dolipski

to obtain the degree of Master of Science
at the Delft University of Technology
to be defended publicly on August 18, 2025, at 14:00

Thesis committee:

Chair:	Prof. Dr. L.L.M. Veldhuis	Flight Performance and Propulsion
External Examiner:	Prof. Dr. W.J. Baars	Aerodynamics
Supervisors:	Prof. Dr. M. Kotsonis	Aerodynamics
	Ir. M. Barahona Lopez	Aerodynamics
	Dr. A. Theiß	DLR Göttingen
	Dr. S. Hein	DLR Göttingen

Place:	Faculty of Aerospace Engineering, Delft
Project Duration:	October, 2024 - June, 2025
Student number:	6067867

An electronic version of this thesis is available at `http://repository.tudelft.nl/`.

Faculty of Aerospace Engineering · Delft University of Technology
Institute of Aerodynamics and Flow Technology · German Aerospace Center (DLR)

Abstract

This thesis presents a comprehensive numerical investigation of wall interference effects in transonic wind tunnel testing of swept-wing configurations, by the example of the Cryogenic Ludwieg Tube Göttingen (KRG) at the German Aerospace Center (DLR). By employing Reynolds-Averaged Navier–Stokes (RANS) simulations using the DLR TAU code and the Spalart–Allmaras turbulence model, the study quantifies how test section walls affect the spanwise flow homogeneity around a swept wing at high Reynolds numbers. A detailed analysis was conducted to isolate the influence of key flow parameters, like angle of attack, sweep angle, chord length, and Mach number, on wall-induced distortions.

The simulations reveal that vertical tunnel walls introduce significant spanwise pressure gradients, especially at higher sweep angles and larger chord lengths, i.e., aspect ratios. These effects are mitigated through a mesh deformation approach based on Radial Basis Functions, which enables the adaptive reshaping of tunnel walls to align with streamlines from an idealized, unbounded flowfield. The implementation of these deformed geometries resulted in substantial improvements in spanwise flow uniformity, reducing the root mean square errors in the pressure coefficient distribution by nearly 50% in critical test section regions. Not only is it possible to reduce spanwise gradients in the flowfield, but also to reduce the difference to infinitely swept conditions almost over the entire width of the test section.

Beyond identifying optimal strategies to reduce the influence of the walls on the flowfield, the thesis validates its numerical findings against existing experimental and numerical data. The proposed methodology offers a valuable toolset for pre-test planning and supports the development of more representative aerodynamic experiments, especially in the context of laminar-to-turbulent transition studies. These contributions provide a scientifically robust foundation for minimizing wall interference in transonic testing and support the advancement of research on laminar-to-turbulent transition.

Contents

Nomenclature

List of Abbreviations

AR	Aspect ratio
CFD	Computational Fluid Dynamics
CFI	Cross Flow Instability
DLR	German Aerospace Center
DNS	Direct Numerical Simulation
ETW	European Transonic Windtunnel
FV	Finite Volumes
ICAO	International Civil Aviation Organization
KRG	Cryogenic Ludwieg Tube Wind Tunnel Göttingen
LES	Large Eddy Simulation
LTT	Low Turbulence Tunnel TU Delft
NASA	National Aeronautics and Space Administration
NLF	Natural Laminar Flow
PSP	Pressure Sensitive Paint
RANS	Reynolds-Averaged Navier-Stokes
RBF	Radial Basis Function
RMSE	Root Mean Square Error
RST	Reynolds Stress Tensor
SA	Spalart Allmaras
T-S	Tollmien-Schlichting
TSP	Temperature Sensitive Paint
TWG	Transonic Wind Tunnel Göttingen

List of Symbols

α	Angle of attack
$\bar{\phi}$	Averaged quantity
δ	Boundary layer thickness
δ^*	Displacement thickness of the boundary layer
δ_{99}	Boundary layer thickness where the velocity reaches 99% of the freestream veloctiy
δ_{ij}	Kronecker delta
γ	Specific heat ratio
Λ	Sweep angle
$\Lambda_{c/4}$	Sweep angle at the quarter-chord line
Λ_{local}	Local sweep angle
μ	Dynamic viscosity
μ_t	Turbulent viscosity
ν	Kinematic viscosity
ω	Specific dissipation rate
ϕ'	Fluctuating quantity corresponding to the averaged quantity
ϕ''	Fluctuating quantity corresponding to the Favre averaged quantity
ρ	Density
ρ_∞	Freestream density
τ_w	Wall shear stress
$\tilde{\nu}$	SA viscosity
$\tilde{\phi}$	Favre averaged quantity
A	Cross-sectional area
a	Speed of sound
A_m	Cross-sectional area at the model
A_w	Cross-sectional area at the wake
c	Chord Length
C_D	Drag coefficient
C_{D0}	Zero-lift drag coefficient
C_{Dw}	Wave drag coefficient

C_f	Skin friction coefficient
C_L	Lift coefficient
C_p	Pressure coefficient
C_{D_0}	Zero-lift drag coefficient
d	Distance
D_B	Buoyancy drag
D_f	Skin friction drag
E	Total specific energy
k	Turbulent kinetic energy
l	Length
M_{dd}	Drag divergence Mach number
Ma	Mach number
Ma_{local}	Local Mach number
n_b	Number of boundary layer nodes
p	Static pressure
p_0	Total pressure
p_∞	Freestream static pressure
q_j	Heat flux
R	Residual or specific gas constant
Re	Reynolds number
Re_c	Chord-based Reynolds number
Re_u	Unit Reynolds number
s	Sum of radial basis functions
t	Time
T_0	Total temperature
T_s	Static temperature
Tu_x	Turbulence intensity of a quantity x
v	Velocity
v_∞	Freestream velocity
v_τ	Friction velocity
v_z	Velocity at the boundary layer edge in spanwise direction
v_{par}	Velocity parallel to the leading edge
$v_{perp,local}$	Local velocity perpendicular to the leading edge
v_{perp}	Velocity perpendicular to the leading edge
X	Tunnel-fixed coordinate in streamwise direction
x	Body-fixed line of flight component
x_0	Body-fixed initial line of flight component
x_{bj}	Boundary nodes coordinates
Y	Tunnel-fixed coordinate in width direction
y	Body-fixed wallnormal component
y^+	Dimensionless wall distance
Z	Tunnel-fixed coordinate in height direction, completing the right hand system
z	Body-fixed component perpendicular to the line of flight, completing the right hand system
z_0	Body-fixed initial coordinate

List of Figures

List of Tables

1 Introduction

1.1. Motivation

In 2022, direct emissions from aviation accounted for almost 4% of the European Union's greenhouse gas emissions.[1] This number, combined with the constant growth of air travel, makes the aerospace industry one of the key contributors to mitigating the impact of climate change. During ICAO's 41st assembly in 2022, the so-called "long-term global aspirational goal for international aviation of net-zero carbon emissions by 2050" was adopted.[2]. This agreement demonstrates the international aerospace industry's commitment to drastically reduce emissions and achieve carbon neutrality by 2050. This important yet equally ambitious goal requires radical improvements at the aircraft level in areas such as aircraft configuration, propulsion, systems, structures, materials, and aerodynamics. Regarding the latter, maintaining laminar flow over both lifting and non-lifting surfaces has significant potential for drag reduction. Extending the flow over a swept wing to 50% laminar would yield fuel savings of 15%.[3]

The parasitic drag, specifically the skin friction drag, is relevant in this context. It is known that for subsonic aircraft in cruise, skin friction drag constitutes half of an aircraft's total drag (Fischer and Ash 1974; Advisory Group for Aerospace Research and Development (AGARD) 1992). The skin friction drag can be drastically reduced by increasing laminar flow on the aircraft's surfaces. Compared to turbulent flow, laminar flow benefits from a less steep velocity gradient at the wall and therefore a lower wall shear stress (White 1991).

To increase the amount of laminar flow, the laminar-to-turbulent boundary layer transition has to be delayed. Natural Laminar Flow (NLF) is a promising method to delay the transition. The method consists of modifying the airfoil shape to increase the extent of laminar flow. Although it is not yet employed in large aerospace companies, significant research is being conducted in the field, for example, within the BLADE project (Gibson, Soucheleau, and Rogers 2021). The idea of employing NLF technology is to stabilize the boundary layer against the growth of various instabilities. On swept wings, crossflow instabilities are of particular relevance. However, the mechanisms driving transition are not yet fully understood (Rius-Vidales and Kotsonis 2021). To better understand the complex flow phenomena leading to transition, turbulent flow, and eventually an increase in skin friction drag, extensive research has been conducted in many companies and research institutions, including the German Aerospace Center (DLR) in Göttingen. This includes both experimental and numerical work, which frequently complement each other.

Experiments are often conducted under cryogenic conditions to achieve similarity to full-scale configurations. One facility where cryogenic conditions can be achieved is the Cryogenic Ludwieg Tube Wind Tunnel (KRG) at DLR Göttingen. It allows testing under transonic conditions with Mach numbers between 0.3 and 0.95, as well as Reynolds numbers of up to 60 million based on a chord length of $150\,\mathrm{mm}$, thus achieving the same Mach and Reynolds numbers as in full-scale applications (Rosemann 1995). However, only limited experience with swept wings has been gained in this tunnel (Egami et al. 2012). Wind tunnel

[1] Accessed 6 November 2024. European Commission (2024). *Reducing emissions from aviation*. https://climate.ec.europa.eu/eu-action/transport/reducing-emissions-aviation

[2] Accessed 6 November 2024. ICAO (2022). *Long term global aspirational goal (LTAG) for international aviation*. https://www.icao.int/environmental-protection/Pages/LTAG.aspx

[3] Accessed 15 November 2024. Delft Matters (2024). *Finding the least resistance*. https://delftmatters.nl/delft-matters-no-5-june-2024/serendipity/

testing poses challenges, as the conditions inside the test section differ from those of free flight. This trend increases when swept wings are tested instead of straight wings, as the spanwise velocity gradient is greatly influenced by the wind tunnel walls (Vatsa and Wedan 1989; Romano et al. 2013). The most recent numerical work to simulate the flow over a swept wing in the KRG was carried out by Köhler (2023). These numerical efforts are crucial for the success of experiments in the tunnel, as they determine the conditions under which accurate results can be obtained. Although boundary corrections are applied to the results obtained from a wind tunnel experiment to account for the presence of the wind tunnel walls compared to free flight, this is only possible to some extent because the interaction of the wind tunnel walls leads to effects that cannot be addressed by such corrections. For example, additional expansion waves form at the wall for high transonic Mach numbers, which influence the flowfield over the entire wing, as Birkemeyer (1999) demonstrated.

This study aims to quantify the influence of the wind tunnel walls on the flowfield and, thus, the deviation from unbounded, infinitely swept wing conditions. With this knowledge, it should be possible to determine parameter ranges under which experiments in the tunnel yield valuable results, i.e., results that represent the flow phenomena on a full-scale wing in free flight. These parameters include freestream-related quantities such as Mach or Reynolds number, model-related quantities like the angle of attack, sweep angle, or chord length, and quantities related to the test section, including adaptive walls. The scope is to close the knowledge gap on the influence of the KRG's test section walls on the spanwise homogeneity of the flowfield by performing three-dimensional RANS simulations on a swept wing under transonic conditions. This lays the foundation for further numerical and experimental investigations of instabilities on a swept wing, which will aid in the design of wings with increased laminar flow, thereby reducing fuel consumption and promoting a more environmentally friendly and economically viable operation of aircraft.

The remainder of this chapter lays the foundation for the work of this thesis. Section 1.2 introduces the flow in a boundary layer, and the laminar-to-turbulent transition process is explained. Section 1.3 introduces the theory of wing sweep and its importance for modern transonic aircraft. The difference between the flow over infinite and finite swept wings is explained, followed by an introduction to wind tunnel experiments and the influence of the walls on the flowfield, as described in Section 1.4.
Finally, Section 1.5 summarizes the findings of the literature study and, based on that, Section 1.6 states the research questions and objective of this thesis.

1.2. Boundary Layer Flows

The flowfield around a body can be divided into two regions. Small velocity gradients characterize the region located away from the body and can be considered essentially inviscid. The second region, located near the body's surface, is where velocity gradients become more significant, friction is substantial, and the flow is viscous. This thin layer of viscous flow, known as the boundary layer, was first discovered by Ludwig Prandtl in 1904, marking a significant advancement in the field of fluid dynamics. The following section provides a detailed examination of the flow behavior within the boundary layer.

1.2.1. Basics of Boundary Layers

The thickness of the boundary layer can be measured in various ways, with two approaches being especially relevant to this work. The classical way to determine the thickness, δ_{99}, is to define the thickness as the wall-normal coordinate where the velocity magnitude reaches 99% of the freestream value, i.e., $v(\delta_{99}) = 0.99 \cdot v_\infty$. The second important measure for determining the boundary layer's influence is the displacement thickness. It is defined as

$$\delta^*(x) = \int_0^\infty (1 - \frac{\rho(x,y)v(x,y)}{\rho_\infty(x)v_\infty(x)})dy, \tag{1.1}$$

where $v(y)$ is the local velocity at a given distance y from the wall and v_∞ is the freestream velocity. This thickness is a representation of the distance by which the inviscid streamlines are displaced due to the slower-moving fluid in the boundary layer (Anderson Jr. 2017).

From the shape of an exemplary boundary layer of a flat plate in Figure 1.1, it can be found that the boundary layer thickness varies with the distance from the leading edge x. A crucial measure for

determining skin friction drag is the shear stress, τ_w, which the fluid exerts on the wall. It is related to the velocity gradient as follows

$$\tau_w = \mu \cdot \frac{dv_x}{dy}|_{y=0}, \tag{1.2}$$

where μ is the dynamic viscosity, and the gradient of the velocity in the streamwise direction to the wall-normal coordinate is evaluated at the wall.

Normalizing the shear stress with the dynamic pressure yields the skin-friction coefficient, which is introduced as

$$C_f = \frac{\tau_w}{\frac{1}{2}\rho v_\infty^2}, \tag{1.3}$$

and the total skin-friction drag is determined by integrating the shear stress over the length l of the surface

$$D_f = \int_0^l \tau_w(x)dx. \tag{1.4}$$

Figure 1.1 displays a schematic boundary layer evolution over a flat plate for a laminar and a turbulent boundary layer. The shape and thickness of the boundary layer are indicated by the blue line, representing the boundary layer edge. The tangents indicate the shear stress at the wall to the velocity profiles, shown in red. It can already be found that the shear stress for a turbulent boundary layer profile is larger than for a laminar one. Following Equation 1.3 and Equation 1.4, this directly translates to more friction.

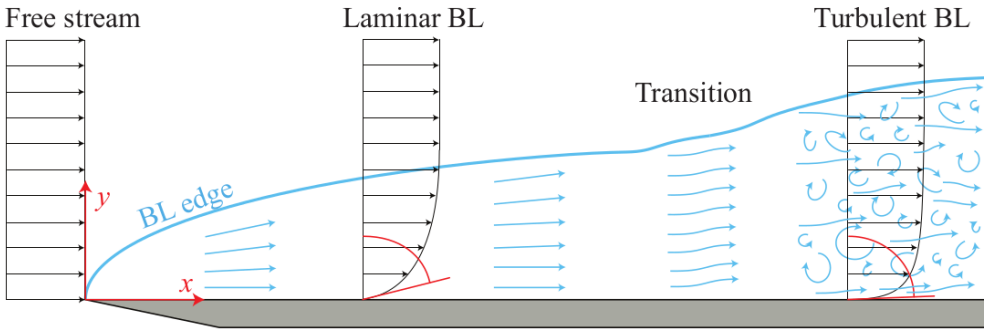

Figure 1.1: Schematic of boundary layer evolution over a flat plate and wall-normal velocity distributions for laminar and turbulent boundary layers. The shear stress is indicated by the tangents to the velocity profiles at the wall, shown in red (Serpieri 2018).

1.2.2. Laminar and Turbulent Flow

Following Eckert (2023), the boundary layer on an airfoil originates from the stagnation point, typically in a laminar state. In this state, the transfer of momentum is driven by the viscous shear stress of neighboring fluid layers on a molecular scale. As the boundary layer moves downstream, disturbances within it can amplify. The unstable growth of these disturbances can lead to the transition from a laminar to a turbulent state. In a turbulent state, the momentum transfer happens at a macroscopic scale.

The boundary layer thickness along a flat plate can be estimated following Schlichting and Gersten (2006) with Equation 1.5 and Equation 1.6 for a laminar and turbulent boundary layer, respectively. The laminar boundary layer thickness equation is derived from the Blasius solution (Blasius 1908) for a two-dimensional, steady, incompressible flow. For the turbulent boundary layer, the findings are based on empirical evidence. These equations show that a turbulent boundary layer grows faster than a laminar boundary layer for the same Re_x due to increased momentum mixing.

$$\delta(x) \approx \frac{5 \cdot x}{\sqrt{Re_x}} \tag{1.5}$$

$$\delta(x) \approx \frac{0.37 \cdot x}{\sqrt[5]{Re_x}} \tag{1.6}$$

The skin friction coefficient for a flat plate can be estimated by Equation 1.7 for the laminar and Equation 1.8 for the turbulent case (Schlichting and Gersten 2006).

$$C_f = \frac{1.328}{\sqrt{Re_x}} \quad (1.7) \qquad C_f \approx \frac{0.074}{\sqrt[5]{Re_x}} \quad (1.8)$$

When plotting the equations for the friction coefficient over the chord-based Reynolds number, as shown in Figure 1.2, it becomes evident that a large amount of laminar instead of turbulent flow can drastically decrease the skin friction coefficient of an aircraft. In particular, at $Re_c = 100 \cdot 10^6$, the turbulent skin friction coefficient can be 14 times the laminar one.

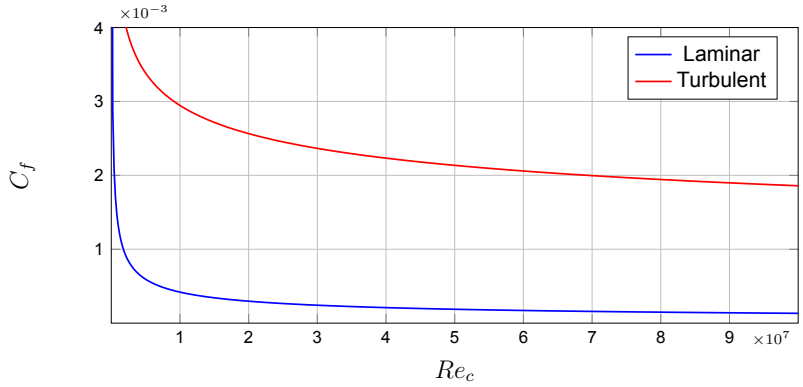

Figure 1.2: Skin friction coefficient of laminar (blue) and turbulent (red) flow over the chord-based Reynolds number.

Consequently, considerable effort is devoted to avoiding turbulent flow on surfaces by delaying the transition from laminar to turbulent flow. This can be accomplished through various flow control methods, of which, in this work, the focus is on NLF technology. One example of such technology is the NLF airfoil used in this work, which will be introduced in Section 2.1.1.

1.2.3. Laminar-Turbulent Transition

Above a certain Reynolds number, referred to as the *critical Reynolds number* (White 1991), the laminar flow becomes unstable. Perturbations in the flow entrain in the boundary layer and grow after reaching the critical Reynolds number. When these instabilities reach a sufficient amplitude, known as the critical amplitude, laminar flow breaks down to turbulence (Van Ingen 2008). The mechanism by which the flow transitions from laminar to turbulent can be manyfold, depending on surface and freestream conditions. The research primarily focuses on four instability mechanisms that lead to laminar-turbulent transition on swept wings, as described in Saric, Muylaert, and Dujarric (1999). Although the laminar-to-turbulent transition is not investigated in this thesis, it is essential to understand the streamwise instability of Tollmien-Schlichting (T-S) waves and the crossflow instability, which manifests as co-rotating vortices, in order to comprehend the work performed in this thesis, as it lays the foundation for experiments investigating transition. Thus, a brief introduction to both mechanisms is given in the following. An overview of these instabilities, together with the attachment-line and the Görtler instability, is schematically shown in Figure 1.3.

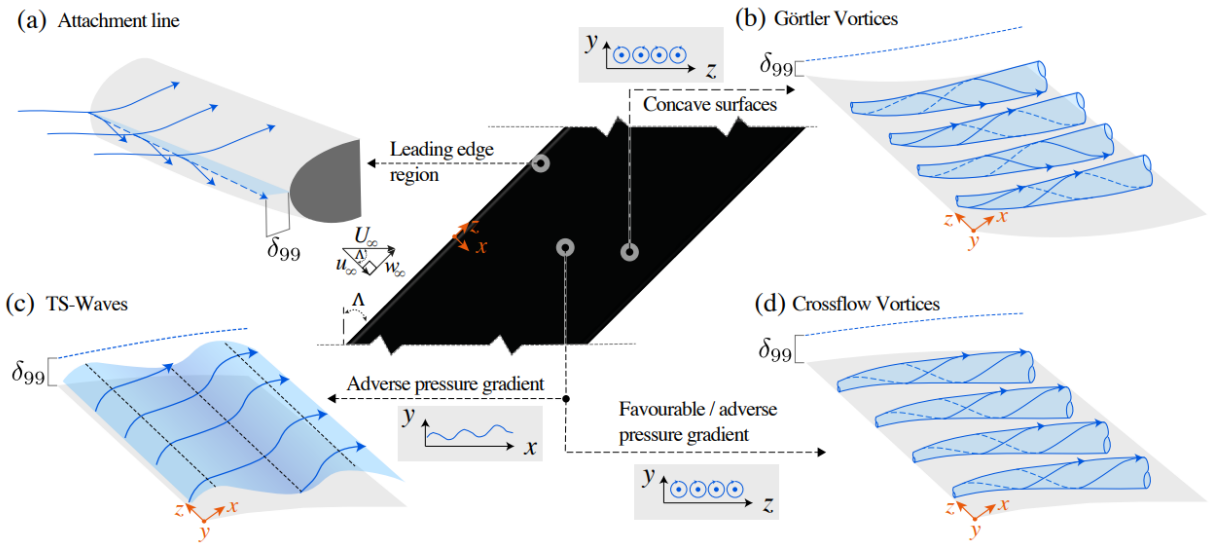

Figure 1.3: Schematic of different boundary-layer instabilities which can develop on a swept wing (Rius-Vidales 2022). (a) Attachment line instability or contamination. (b) Görtler instability. (c) Tollmien-Schlichting waves instability. (d) Crossflow instability.

Tollmien-Schlichting Instability

The early work of Prandtl (1921) and Taylor (1915) is essential for understanding the nature of the instabilities. In recent years, numerous authors have presented their work on T-S waves. For subsonic Mach numbers, the Tollmien-Schlichting instability manifests as streamwise waves, characterized by their two-dimensional nature and long wavelengths of roughly six times the boundary layer thickness. They are shown in Figure 1.3. As the waves move downstream, they are amplified until they become large enough for nonlinear effects to take over.

Figure 1.4 shows the transition process of a boundary layer initiated by T-S waves. The initially stable laminar flow develops into viscous instabilities, forming T-S waves that are amplified as they move downstream. Following, three-dimensional fluctuations in velocity and pressure develop. The following process is a breakdown of the three-dimensional structures. Finally, turbulent spots form, which then burst, resulting in a fully turbulent flow (Schlichting and Gersten 2006).

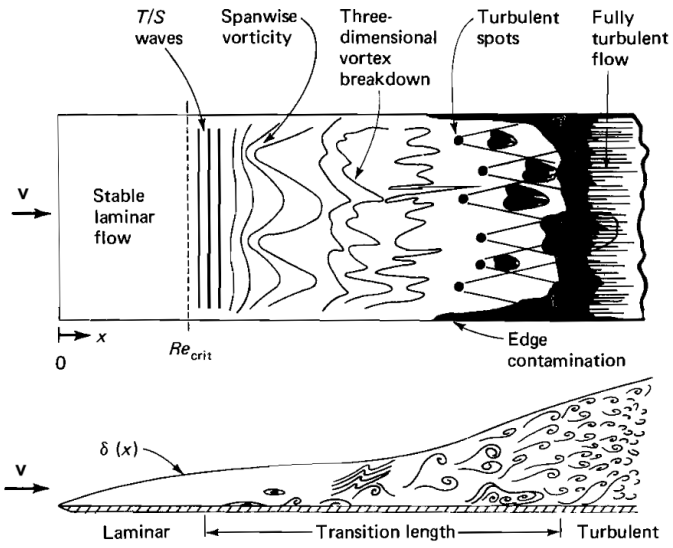

Figure 1.4: Transition process of a boundary layer, initiated by T-S waves (White 1991).

One possibility to delay this transition mechanism is to use NLF airfoils, as the T-S waves stabilize under a favorable pressure gradient and destabilize under an adverse pressure gradient (Wassermann and Kloker 2005). Following experiments by Liepmann and Nosenchuck (1982), it is also possible, for example, to control and reduce the unstable amplitudes of T-S waves using unsteady surface heating.

Crossflow Instability

The laminar-to-turbulent transition over a swept wing can be caused by the growth and breakdown of cross-flow instability (CFI) modes. For high sweep angles, this is the dominating transition mechanism (Joslin 1998). A fluid particle traveling along a streamline near the aerodynamic body is in a state of force equilibrium, orthogonal to the streamline and parallel to the model surface. The equilibrium is dictated by the pressure forces causing centripetal acceleration and by the centrifugal forces. This equilibrium does not hold within the boundary layer, which causes the fluid particle to exhibit a spanwise velocity component, resulting in a phenomenon known as cross-flow. Due to the no-slip condition at the wall and the inviscid nature of the flow outside the boundary layer, the boundary-layer velocity profile along the direction orthogonal to the inviscid streamlines is zero at the wall and the edge of the boundary layer, as shown in Figure 1.5a. The velocity profiles feature a point of inflection, which gives rise to inviscid instability modes (Bippes 1999). Following Rayleigh's theorem, the inflection point of the velocity profiles is a necessary criterion for the instability (S. Pope 2000).

Following Serpieri (2018), surface flow visualization experiments at the Low Turbulence Tunnel (LTT) in TU Delft have demonstrated a transition scenario characterized by sequences of streaks aligned with the flow direction. Figure 1.5b shows the CFI transition on a $45°$ swept wing at $Re = 1.3 \cdot 10^6$ performed in the LTT facility. The streaks of the vortices and the transition front are visualized. They cause a velocity change in spanwise direction and, therefore, of the wall skin friction. The cross-flow vortices modify the mean flow and, thus, the stability of the boundary layer. They enable a transfer of low-momentum flow from the lower regions of the boundary layer to the high-momentum regions and vice versa. This results in a modified boundary layer featuring a momentum modulation of the flow in the spanwise direction and in the development of strong velocity shears in the spanwise and wall-normal directions, which are highly unstable to secondary instability mechanisms (Serpieri 2018).

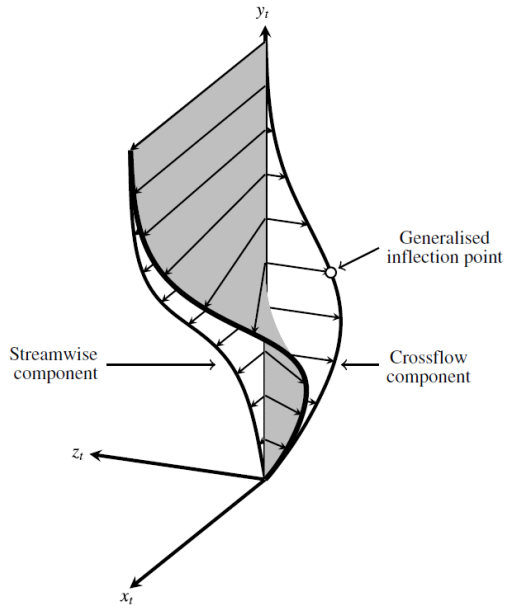

(a)

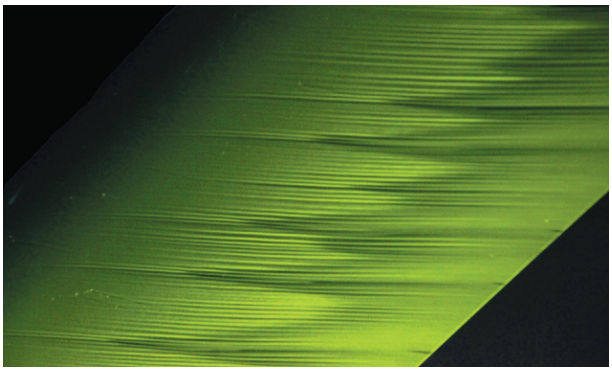

(b)

Figure 1.5: Cross flow instabilities (Serpieri 2018). (a) Typical crossflow velocity profile. (b) Fluorescent oil visualization on a 45°swept wing in the TU Delft LTT facility. Flow from the left. The darker areas show the turbulent region of the boundary layer. The CFIs' streak-like footprint on the wing surface is also captured.

1.3. Wing Sweep

German aerodynamicist Adolf Busemann first introduced the concept of swept wings in 1935 at the Volta congress in Rome, Italy (Meier 2005). As engines became more powerful and airplanes flew faster, transonic flight regimes became increasingly relevant to engineers. Busemann demonstrated that, when using swept wings, the aircraft could fly at higher Mach numbers before experiencing a significant increase in drag. Ever since the introduction of wing sweep on the Messerschmitt Me 262 and the de Havilland Comet, wing sweep has been widely adopted in the aerospace industry for both military and civilian applications.

Although there are several drawbacks to applying sweep on a wing, using wing sweep on transonic wings is essential for reducing drag. Some drawbacks include the increased structural weight resulting from a higher wingspan, the increased wing weight required to resist the aerodynamic twist that occurs during bending, the reduced effectiveness of control surfaces, and the increased manufacturing complexity. While no further emphasis will be laid on these aspects, more information can be found in Torenbeek (1982).
As Busemann showed, the reason to use swept wings regardless of the drawbacks is the higher drag divergence Mach number (Meier 2005), which will be explained in Section 1.3.2.

1.3.1. The Theory of Wing Sweep

In an experiment conducted in the high-speed wind tunnel at NASA Langley, Adler (1947) compared wings with different sweep angles at two transonic Mach numbers. All wings were compared for a fixed aspect ratio of two to isolate the effect of sweep from the impact of aspect ratio. The resulting drag polars are shown in Figure 1.6, where the drag and lift coefficients represent the drag and lift divided by the dynamic pressure and a reference area. For the lower Mach number of 0.750 in Figure 1.6a, the drag coefficient does not significantly change with a change in sweep angle. For the higher subsonic Mach number, shown in Figure 1.6b, it can be concluded that an increase in sweep angle decreases the drag coefficient at constant lift coefficient. Notably, a significant reduction in C_{D_0} is observed. This drag reduction at high Mach numbers is the reason for employing swept wings on an aircraft flying in the transonic regime.

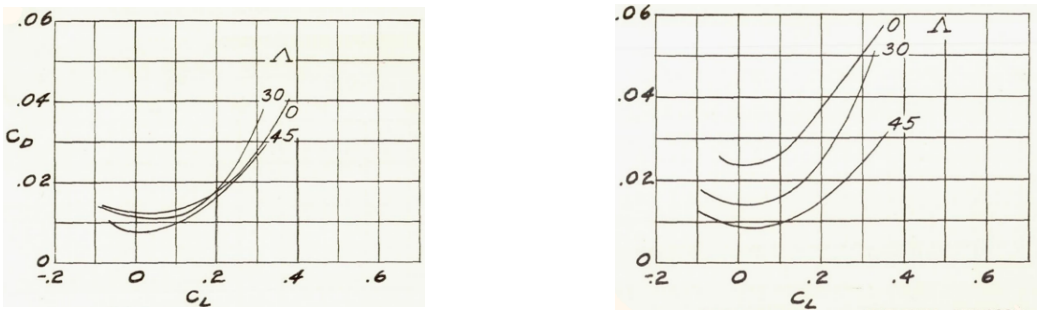

Figure 1.6: Drag polars of wings with different sweep angles and fixed aspect ratios using NACA 65-110 profiles in planes normal to the leading edge and AR = 2 (Adler 1947). (a) At Mach 0.750. (b) At Mach 0.925.

Figure 1.7 shows the top view of two non-tapered wings with infinite span. The wing in Figure 1.7a is in straight flow, while the wing in Figure 1.7b experiences the inflow at an angle Λ. As Obert (2009) points out, there are multiple definitions to measure the sweep angle Λ of a wing, the most common being measured at the quarter-chord line. The airfoil section perpendicular to the leading and trailing edge, marked blue in the figure, is defined as the *original* airfoil section. The *stretched* airfoil section, defined in the direction of the freestream velocity, is shown in orange. Both wings experience the same freestream velocity, v_∞. For the straight wing, the freestream velocity is also the velocity perpendicular to the leading edge. For the swept wing, the perpendicular velocity is reduced due to the decomposition of the freestream velocity into a component perpendicular, v_{perp}, and parallel, v_{par}, to the leading edge.

Obert (2009) uses two options to explain the delay of drag divergence on swept wings, first using the *original* airfoil shape and second using the *stretched* airfoil shape. First, as the velocity parallel to the *original* airfoil is reduced from v_∞ to the normal component v_{perp}, the increase in wave drag, which

Anderson Jr. (2017) describes as a form of pressure drag caused by the presence of a shock wave, is delayed to higher Mach numbers. The dissipative nature of shocks causes an increase in drag as the entropy rises, resulting in a portion of the total pressure being lost. Second, the freestream velocity v_∞ over the *stretched* airfoil results in lower velocity increases on the surface due to the reduced airfoil curvature of the *stretched* airfoil compared to the *original* airfoil, which is a geometric effect.

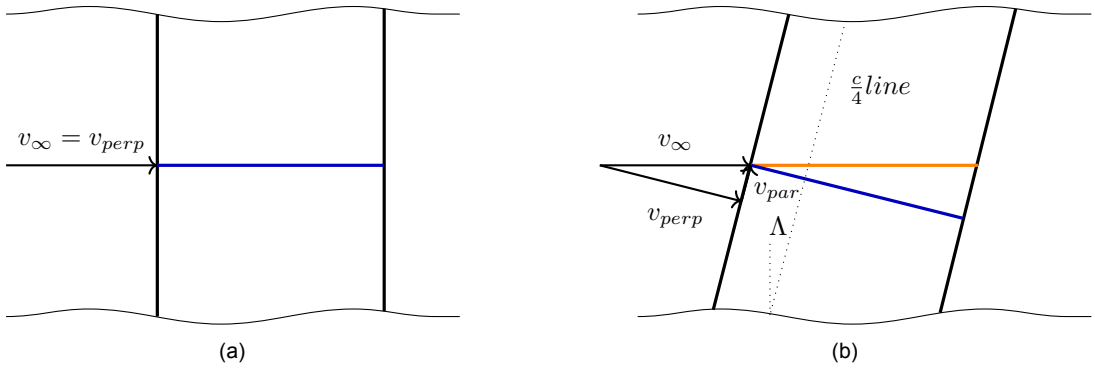

Figure 1.7: Infinite non-tapered wings in top-view. (a) Straight wing with *original* airfoil in blue. The freestream velocity is equal to the velocity perpendicular to the leading edge, due to the absence of sweep. (b) Swept wing with *original* airfoil in blue and *stretched* airfoil in orange. The freestream velocity is decomposed into a component perpendicular and parallel to the leading edge.

Following Vos and Farokhi (2015), although the unswept and swept wings experience the same freestream velocity, the absolute value of the pressure coefficient, which is defined in Equation 1.9, for the unswept wing will be higher due to a higher velocity increase and lower static pressure over the wing's surface. In return, this allows for higher freestream Mach numbers for the swept wing compared to the straight wing to reach the same Mach number on the wing's surface. Thus, the swept wing's drag divergence Mach number increases, which will be analyzed in more detail in the following section.

$$C_p = \frac{p - p_\infty}{\frac{1}{2}\rho_\infty v_\infty^2} \tag{1.9}$$

1.3.2. Effect of Wing Sweep on Drag Divergence Mach Number

Vos and Farokhi (2015) define the drag divergence Mach number as the Mach number at which the derivative of the drag coefficient with respect to the Mach number reaches

$$\frac{\delta C_D}{\delta Ma} = 0.1. \tag{1.10}$$

For Mach numbers lower than the drag divergence Mach number, the drag increases slowly with an increase in Mach number, a phenomenon known as drag creep. At Mach numbers higher than the drag divergence Mach number, the drag increases rapidly as the Mach number is further increased. This behavior is caused by the occurrence of shocks in the vicinity of the airfoil's surface, as already explained in more detail in Section 1.3.1.

Figure 1.8 shows how the wing's wave drag coefficient, C_{D_W}, changes with Mach number. Both wings for this example are tapered and exhibit a sweep angle at the quarter chord line of $\Lambda_{c/4} = 0°$ and $\Lambda_{c/4} = 45°$. The drag divergence Mach number is defined as shown in Equation 1.10 and marked in the figure as M_{dd}. It can be observed that an increase in Mach number results in an increase in the wing's wave drag coefficient. A significant increase in the drag divergence Mach number of the swept wing compared to the unswept wing is observed. This holds for an analytical approach following Torenbeek (1982) as well as for experimental data acquired by Johnson (1951).

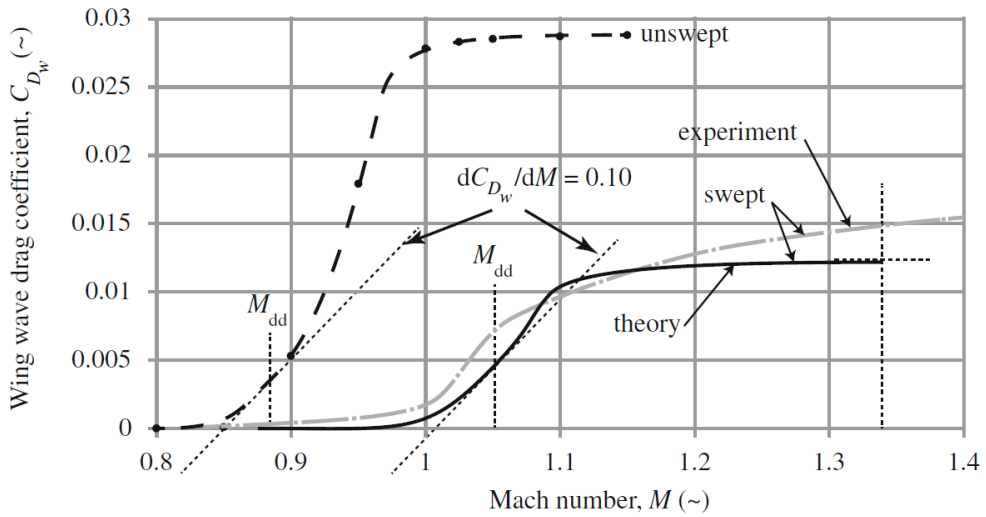

Figure 1.8: Wing wave drag coefficient versus Mach number for a 45°-swept (solid and dash-dotted lines) and unswept wing (dashed line). The drag divergence Mach number M_{dd} is defined in Equation 1.10 (Vos and Farokhi 2015). The theoretical and experimental values are derived and acquired by Torenbeek (1982) and Johnson (1951), respectively.

1.3.3. Flow over Infinite Swept Wings

This section considers inviscid flow over an infinite swept wing, which is approximately true for the region outside the boundary layer, where velocity gradients are small.

The shape of the streamlines around a swept wing differs from that around a straight wing. While the flow across an infinite straight wing does not feature a velocity component in spanwise direction, the flow across a swept wing features a chordwise and spanwise component. Figure 1.9 indicates how the isobars on a swept wing influence the motion of a fluid particle travelling over its surface. While the negative pressure gradient near the leading edge causes the particle's direction of motion to curve to the left (in the flow direction), the positive pressure gradient toward the trailing edge causes the direction of motion to curve back to the right (in the flow direction). The resultant streamlines differ for the suction and pressure surfaces, as the pressure distribution for both surfaces can be different.

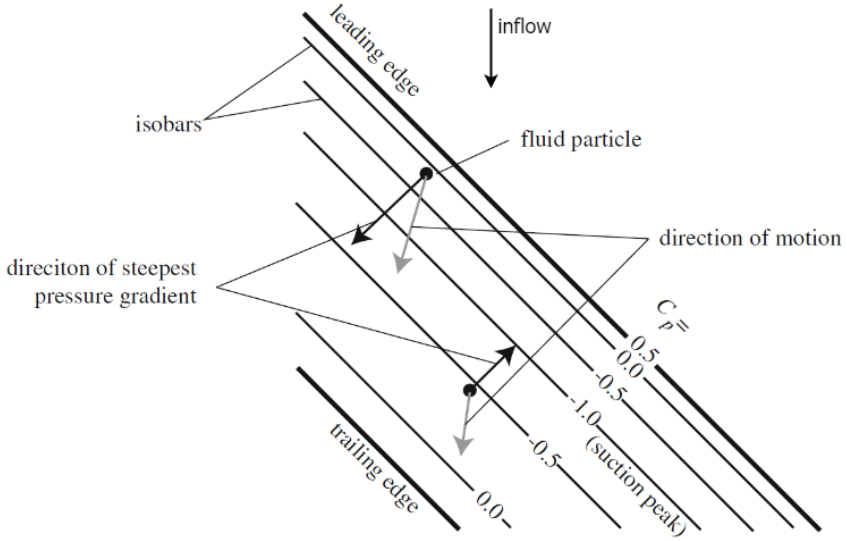

Figure 1.9: Direction of fluid particle motion due to isobar pattern on an infinite swept wing, where the isobars are drawn parallel to the leading and trailing edge (Vos and Farokhi 2015).

If the pressure distribution is known, which can, for example, be determined in a wind tunnel test or a numerical simulation, a calculation of the flow direction and thus the determination of the shape of the inviscid streamlines is possible. For this purpose, a constant velocity in the spanwise direction is assumed. The pressure coefficient can be calculated following Equation 1.9. With the expression for the speed of sound a, shown in Equation 1.11, and the ideal gas law in Equation 1.12, it is possible to derive the expression for the pressure coefficient shown in Equation 1.13, where γ is the specific heat ratio.

$$a = \sqrt{\gamma RT} \qquad (1.11) \qquad p = \rho RT \qquad (1.12)$$

$$c_p = \frac{p - p_\infty}{\frac{1}{2} Ma_\infty^2 \gamma p_\infty} = 2 \cdot (\frac{p}{p_\infty} - 1) \cdot \frac{1}{Ma_\infty^2 \cdot \gamma} \qquad (1.13)$$

The isentropic flow equations yield expression 1.14 for the pressure ratio, which can be substituted into Equation 1.13 to yield Equation 1.15.

$$\frac{p}{p_\infty} = (1 + \frac{\gamma - 1}{2} \cdot Ma_{local}^2)^{\frac{-\gamma}{\gamma - 1}} \qquad (1.14)$$

$$c_p = \frac{2}{Ma_\infty^2 \cdot \gamma}((1 + \frac{\gamma - 1}{2} \cdot Ma_{local}^2)^{\frac{-\gamma}{\gamma - 1}} - 1) \qquad (1.15)$$

Solving Equation 1.15 for the local Mach number results in

$$Ma_{local} = \sqrt{\frac{2}{\gamma - 1} \cdot ((\frac{c_p \cdot Ma_\infty^2 \cdot \gamma}{2} + 1)^{\frac{\gamma - 1}{-\gamma}} - 1)}. \qquad (1.16)$$

With the known relation $v = Ma \cdot a$, it is possible to determine the local velocity over the wing at any given point along the chord. The angle between the local flow component in the chordwise direction and the flow component in the spanwise direction is

$$\Lambda_{local} = arctan(\frac{v_{par}}{v_{perp,local}}). \qquad (1.17)$$

As the velocity parallel to the leading edge is constant, the velocity in the chordwise direction can be calculated at any point over the wing. Knowing the velocities, the shape of the streamlines over the wing can be determined by integrating the streamline equations $\frac{dz}{dx} = \frac{v_z(x)}{v_x(x)}$ as follows

$$z(x) = z_0 + \int_{x_0}^{x} \frac{v_z}{v_x(x')} dx', \qquad (1.18)$$

where x_0 and z_0 are initial coordinates, and x' is the coordinate used to integrate along the chord.

It must be noted that, although the stated literature presents the importance of the flow over infinitely swept wings, this case is idealized and does not exist on a real wing. Instead, the flow over finite swept wings is of importance, which will be introduced in the following section. Infinitely swept wing flow conditions are only roughly applicable to the spanwise sections further away from the wing root and wing tip.

1.3.4. Flow over Finite Swept Wings

The inviscid flow assumption is also considered for the flow over finite swept wings. The difference to the infinite swept wing lies in the spanwise component of the flow, which is not constant, as the wingtips, wind tunnel walls, or junction to the fuselage constrain the flow.

Figure 1.10 shows the isobars for two non-tapered, swept wings with different aspect ratios at zero lift. The dashed lines indicate lines parallel to the leading and trailing edges, which would be the isobars for the infinite swept wing. As can be found from both wings and in contrast to Figure 1.9, there is a significant curvature of the isobars, represented by the solid lines. While the isobars are roughly aligned with the leading edge in the middle part of the span, they curve forward at the wingtip and backward at the wing root.

In contrast to the infinitely swept wing, the streamlines over the wing can behave differently for each spanwise location. When analyzing the behavior of streamlines in a finite case, it is necessary to evaluate them at different spanwise locations to capture the flowfield accurately. Adding wind tunnel walls to the condition shown in Figure 1.10 makes the flow at the root and tip more challenging to predict, as the walls introduce viscous effects compared to free flight conditions. The influences of wind tunnel walls are explained in the following section.

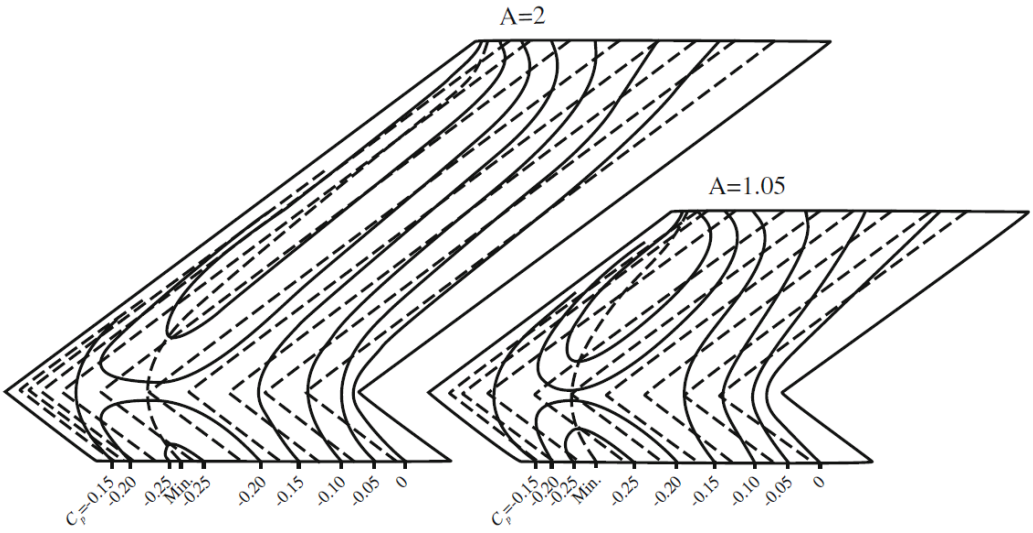

Figure 1.10: Isobar pattern over two 53° swept wings of different aspect ratios at zero lift. Straight dashed lines indicate parallels to the leading and trailing edge, the curved dashed line indicates the minimum pressure coefficient, and solid curved lines indicate isobars (Vos and Farokhi 2015).

1.4. Wind Tunnel Experiments and Wall Influence

Wind tunnel experiments are an integral part of the development of new technology, offering cheaper and more flexible possibilities compared to flight experiments (Malik and Bushnell 2012). Nevertheless, compared to numerical simulations, they are more expensive, and not all flow phenomena can be captured without influencing the flow, which is why they are often supplemented with numerical analyses (Ross 2023). In the following sections, the influence of the wind tunnel on the experimental results is explained.

1.4.1. Test Section Setup

Wind tunnels exist in various configurations and differ in their test section configurations, tunnel configurations, flow regimes, and flow properties (Barlow, Rae, and Pope 1999). A brief introduction to the differences regarding the test sections is given. The setup of the specific wind tunnel used during this thesis is introduced in Section 2.1.2.

In high-performance facilities, closed test sections are commonly used (Britcher and Landman 2023). As the name suggests, a closed test section features clearly defined walls acting as boundaries on the flow. These walls influence the flow compared to free flight, making boundary corrections necessary. As will be discussed in this section, these boundary corrections can only eliminate the influence of the walls to a certain extent. Optionally, the walls of a closed test section can be adaptive to allow for exact control of the boundary conditions at the wall. This method yields no efficiency losses, and the boundary conditions can be adjusted according to the conditions under which the model is tested. If applied correctly, this results in minimal or no correction being needed. However, this method cannot be applied to all cases, as an experimental setup with shocks present or with high-pressure gradients may cause difficulties in adjusting the walls, necessitating no correction (Barlow, Rae, and Pope 1999). An example of how to apply the possibility of adaptive walls in a test section is shown in Figure 1.11a and Figure 1.11b for a longitudinal-section and cross-sectional view of the KRG's adaptive test section.

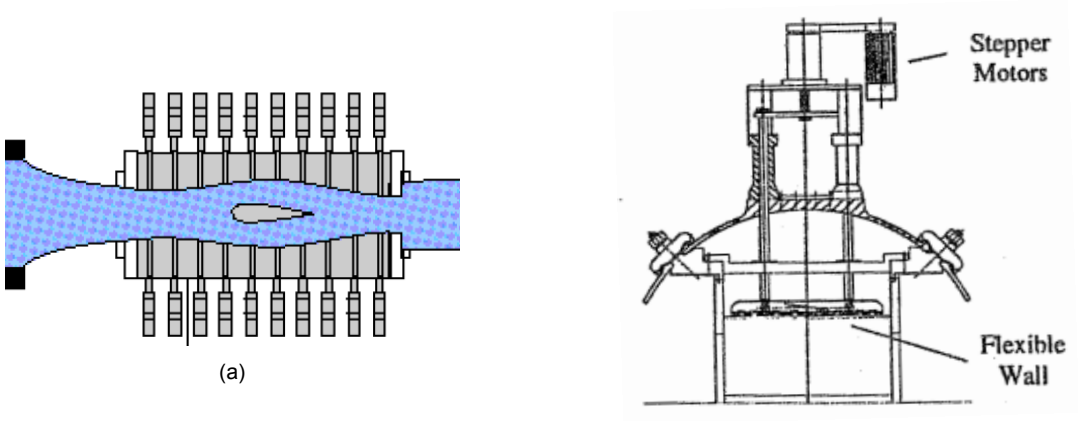

(a) (b)

Figure 1.11: Sectional views of the adaptive test section of the KRG. (a) Longitudinal-section view of the test section with adaptive walls and an airfoil (Koch et al. 2008). (b) Cross-sectional sketch of the adaptive wall test section of the KRG, adjustable by stepper motors (Rosemann 1995).

1.4.2. Boundary Corrections

As mentioned in the previous section, the flow conditions in a wind tunnel often do not represent free-flight conditions. This is why boundary corrections are applied to the results of a wind tunnel experiment to account for the effects within the tunnel. After correcting the wind tunnel data in a flow with matching Reynolds and Mach numbers, the results obtained during the measurements can be used to determine the forces and moments on the full-scale aircraft in free flight. Following Barlow, Rae, and Pope (1999), the most common correction methods are based on the so-called method of images, the measured variable method, and panel methods. These boundary corrections are derived based on the assumption of a small model compared to the test section and an infinitely long test section. Therefore, the linearized potential flow equations are applicable. This enables a superposition of all corrections to arrive at the final effects. A brief introduction to the relevant boundary corrections for this thesis is given in the following. However, these corrections yield valuable results only when the flow in the tunnel and the flow in free flight are similar, requiring small differences between the two cases. As Birkemeyer (1999) showed, the side walls can impact the flow in the tunnel to such an extent that even applying known corrections to the obtained data no longer accurately represents the flow in free flight. This is why it is essential to understand the influence of the walls on reducing their impact on the flow.

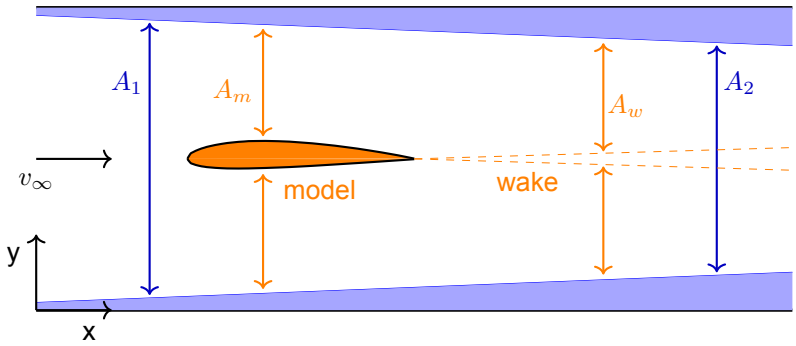

Figure 1.12: Sketch of the effects within the test section that are addressed by boundary correction procedures. The decrease in effective cross-sectional area from A_1 to A_2 due to a thickening of the boundary layer at the tunnel walls is indicated in blue. The blockage effects are shown in orange, where the change in effective cross-section due to the presence of the model and the wake is indicated.

Buoyancy

This effect refers to the variation in static pressure along the test section, even when no model is present. As the boundary layer develops on the walls of the test section, the effective area in the tunnel decreases,

as shown in Figure 1.12. Due to continuity, the velocity in the test section increases, and the static pressure decreases. This pressure gradient is manifested by increased pressure drag, which can be calculated from the static pressure along the tunnel $p(x)$ and the tunnel's cross-sectional area along the tunnel $A(x)$ as follows

$$D_B = \int_0^l A(x) \frac{dp(x)}{dx} dx. \tag{1.19}$$

A common solution to eliminate or reduce the impact of buoyancy is to build a slightly diverging test section so that the effective area in the test section remains constant even with a thickening boundary layer (Britcher and Landman 2023).

Blockage
This effect is a boundary influence due to the displacement of streamlines around non-lifting bodies, wakes, or slipstreams, and is sketched orange in Figure 1.12. It can be distinguished into solid, wake, and slipstream blockages. The solid blockage results from the volume occupied by the model in the test section and, for an airfoil, depends on both the model size and thickness. Following continuity, the velocity increases because compared to free flight, the tunnel walls limit the displacement of the flow (Britcher and Landman 2023). The wake blockage has the same effect as solid blockage, but is somewhat more complicated to estimate, as it depends on the volume occupied by the wake of the model, which in turn depends on the shape of the model itself. As the velocity in the wake of a body is lower than in the freestream, the flow around the wake is accelerated, in accordance with the principle of continuity. The opposite applies to slipstream blockage because the flow in the slipstream of, for example, a propeller is accelerated. This causes a decrease in velocity around the slipstream. All three blockage effects lead to a change in velocity around the model, which, following (Barlow, Rae, and Pope 1999), on a cylinder with $0.6\,$m diameter in a $3\,$m wide testsection, is increased by $3.3\,\%$. It can be mathematically represented and calculated as flow singularities through the superposition of a source and sink, modeling the object placed in a freestream and mirrored at the walls to account for boundary effects.

1.4.3. Wall Influence

Although the aforementioned corrections try to eliminate the discrepancies between wind tunnel and free flight, there are deviations between the two that cannot be compensated for by the corrections. This section introduces the influence of tunnel walls on the flowfield, which cannot be compensated for by the aforementioned corrections. It is distinguished between the horizontal and the side walls of the test section, as well as the corner effects that result from an interference at the junction of the walls. A general overview of wall influences and interference effects can be found in Goethert (1961).

Horizontal Walls
One influence of the flowfield is related to the horizontal walls of the test section. As Birkemeyer (1999) and Ganzer (1985) show, the effects are mainly inviscid and can be reduced when the wall contour follows a streamline of the unbounded condition. For a total elimination of their impact, the horizontal walls would have to be deformed along a streamline of the free flight condition, while also respecting the displacement thickness of the walls' boundary layer. However, as Birkemeyer (1999) showed, deforming the walls only following the inviscid streamlines yields close alignment with the unbounded case, especially for the middle section of the tunnel. This procedure is highly relevant to this work and can be applied to numerous applications, especially when numerical situations are performed in advance of the experiments to determine the shape of the streamlines. Another possibility for defining the shape of the walls is described by Ganzer (1985), where a calculation of pressures is used to create equilibrium at the walls. A similar approach is later described in Section 2.1.2 for the KRG. Results from different wind tunnels show that transonic blockage can be avoided when compared to straight, undeformed walls (Ganzer 1985). Due to mechanical complexity, the adaptation is usually not possible in three dimensions. Nevertheless, a two-dimensional adaptation works well because the pressure distribution does not vary significantly in the spanwise direction (Goethert 1961). The relatively easy procedure is the reason why the use of two-dimensional adaptive horizontal tunnel walls is well established, including in the KRG. An example of the deformation is shown in Figure 1.13. Especially for experiments with unswept wings, these adaptation procedures yield excellent results at an acceptable increase in complexity. The wall contour can then only be changed in the longitudinal direction, i.e., in the freestream direction, but not in a cross-sectional direction, i.e., perpendicular to the freestream direction.

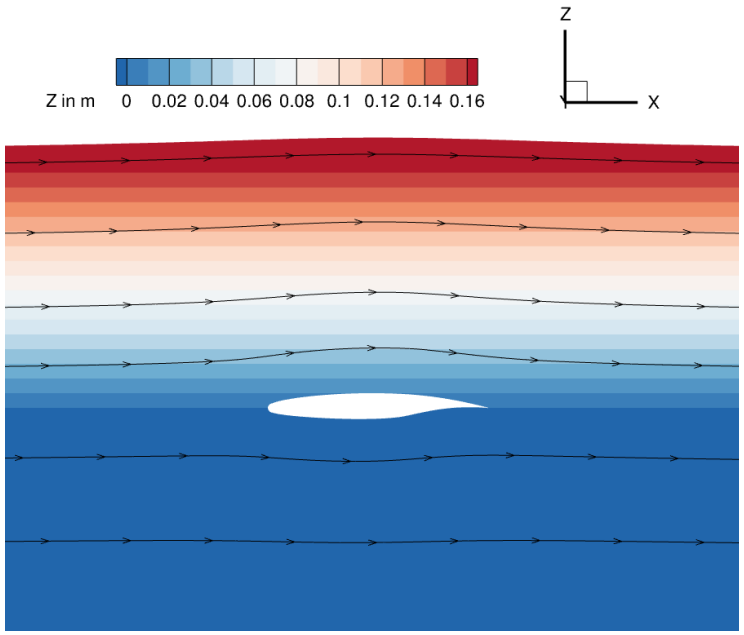

Figure 1.13: Cross-sectional view of the KRG in the X-Z-plane, with an unswept airfoil and deformed upper and lower walls. The walls are deformed to match the streamline shape of the unbounded case at the same Z-location. Six exemplary streamlines are shown.

For three-dimensional models or swept wings, the horizontal walls would have to be adapted in three dimensions to eliminate their effect. Compared to the unswept wing, the flow over a swept wing exhibits a spanwise gradient, which increases the complexity of the flowfield and the adaptation procedure. Adapting the horizontal walls three-dimensionally requires extensive control hardware while only marginally increasing the accuracy of the measurements, as Birkemeyer (1999) shows. To reduce the complexity of building and operating the tunnel, it is possible to simplify the problem by using a two-dimensional wall contour that matches the streamline at only one spanwise location, and additionally, to account for the displacement thickness of the wall's boundary layer. This neglects the fact that the wall contour would have to be adapted separately for every Y-location. Birkemeyer (1999) showed that the results aligning closest with the infinitely swept wing conditions are achieved for choosing the spanwise location in the middle of the test section.

Side Walls

As shown in Section 1.3, the flow field differs between the infinitely swept wing and the finite swept wing conditions. Bounding a swept wing experiment by straight vertical tunnel walls causes an alternation of streamlines by spanwise flow non-uniformity and by interference effects on the wing's surface.

As shown by Birkemeyer (1999), side wall interferences in experiments with non-swept wings are caused by viscous effects. The side wall boundary layer is altered due to the pressure influence of the wing. This causes a change in cross-sectional area (e.g., pronounced growth of the boundary layer in the region of a shock), and a spreading of shock and expansion waves that can reach into the flowfield. Strong shocks can lead to a detachment of the boundary layer and cause eddies to form, which in turn reduces the region of two-dimensional flow in the tunnel. This situation is sketched in Figure 1.14. In an experiment, Ganzer, Stanewsky, and Ziemann (1984) demonstrated that the aspect ratio is the most significant parameter influencing the effect of interference. While strong interference effects were observed for a CAST 7 profile with AR < 2, they decayed asymptotically in the middle of the test section for AR > 2. However, experiments with a NACA 0012 profile showed significantly less interference effects, indicating a dependence on the airfoil shape as well. For a simulation with a Mach number of $Ma = 0.755$ and Reynolds number of $Re = 8 \cdot 10^6$, Birkemeyer (1999) showed that the pressure distribution in a tunnel with straight walls differs from the unbounded simulations slightly. In the middle of the test section, the shock position is shifted by $\Delta x/c = 0.03$ upstream compared to the unbounded case. When using an inverse

design of the tunnel wall, where the streamline of the wall boundary layer is used as the wall contour, the pressure distribution of the bounded case aligns closely with that of the infinite wing.

Hoang and Bui (2019) performed experimental and numerical analyses for a straight wing, determining interference effects with and without tunnel walls. From the simulations, it is shown that although the lift coefficients in the middle section of the wing exhibit a difference of less than 2% between the cases at moderate angles of attack, this difference increases to more than 10% when the angle of attack is increased and the wing approaches the tunnel wall. This work suggests that the effect of tunnel walls will vary significantly with variations in geometric and flow variables. Nevertheless, it is also implied that a change in the experimental setup can diminish the effect of the tunnel walls.

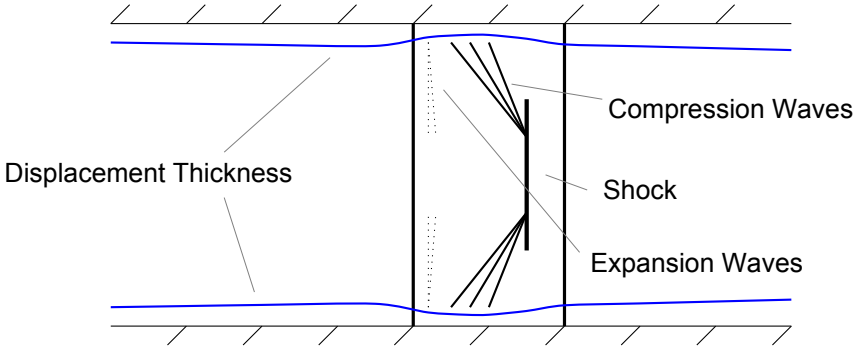

Figure 1.14: Side wall interference on a straight wing, following Birkemeyer (1999). The wall boundary layer is indicated in blue.

In addition to the two-dimensional viscous interference explained above, interference due to the three-dimensional behavior of the streamlines occurs for swept wings, as demonstrated by early work by Rogers and Hall (1960). Vatsa and Wedan (1989) performed numerical simulations on a $20°$ swept NACA 0012 wing inside a wind tunnel, focusing on the difference between viscous and inviscid side walls. It was demonstrated that both inviscid and viscous sidewall simulations exhibited a relatively close alignment of the pressure coefficient with the experiment in the middle of the span. Towards the tunnel walls, the alignment with experimental data becomes less accurate. This is caused by the larger pressure gradients towards the tunnel walls and the more complex flow phenomena that result. As shown in Figure 1.15, the movement of the streamlines is suppressed by the walls. This causes a compression in the leading edge area of the more upstream end of the wing and an expansion at the leading edge of the more downstream end of the wing. These compression and expansion waves influence the flowfield over the entire wing. Following Birkemeyer (1999), the isobar pattern over the suction surface of a wing bounded by straight tunnel walls differs significantly from the infinitely swept wing condition. A drop in pressure between the more upstream end of the wing and the more downstream end of the wing is a result of the compression and expansion waves shown in Figure 1.15.

Again, contoured sidewalls increase the spanwise flow uniformity over a swept wing significantly, especially towards the aft section of the airfoil, as Serpieri (2018) showed for a flow in slow freestream of $v_\infty = 25\,\frac{\mathrm{m}}{\mathrm{s}}$ at moderate Reynolds number ($Re = 2.12 \cdot 10^6$). Contouring the walls can be achieved using stepper motors, as explained in more detail in Section 2.1.2, or by utilizing so-called liners. These liners are devices designed to direct the flow in a wind tunnel's test section, and can, for example, be manufactured of plywood (Romano et al. 2013).

The design of contoured side walls for a swept wing in transonic flow is explained by Birkemeyer (1999). Numerical simulations for an infinitely swept wing were performed to extract the streamlines around the wing. Based on the contour of the streamlines, a three-dimensional mesh was generated. These results do not account for the displacement thickness of the wall's boundary layer. Nevertheless, the pressure distribution shows close alignment with the infinitely swept conditions, with the shock location shifted upstream by $\Delta x/c = 0.035$. When taking the wall boundary layer into account during wall deformation, which is done in an iterative procedure, no difference is noted compared to the infinitely swept wing conditions. Only very close to the wall, the isobars slightly curve towards the walls. As explained for the horizontal walls, this procedure is very complex to realize in three dimensions. Additionally, adjusting or

manufacturing the wall for every test point is very costly. One design point can be chosen to determine the ideal side wall contour for a configuration. This configuration is then used for all test points, although the flowfield is not precisely the same. Birkemeyer (1999) showed that the difference between a test point outside the design point can be slight compared to that of a non-contoured wall, when the freestream conditions do not vary significantly. For larger deviations or geometric changes, a separate evaluation has to be performed.

Romano et al. (2013) designed and tested contoured side walls for experimental campaigns studying receptivity mechanisms in the RECEPT project. Similar to the approach of Birkemeyer (1999), the shape of the side walls was determined by extracting the streamlines from the unbounded simulation. Although the isobars on the pressure side of the wing were parallel to the leading edge, the suction side did not guarantee such behavior, especially when approaching the tunnel walls. Nevertheless, the work demonstrated that the developed model is suitable for measuring the linear receptivity characteristics of a swept-wing boundary layer associated with the excitation of cross-flow instability modes.

Despite the successful application of liners and deformation of wind tunnel walls, it remains uncertain how the application of such measures will affect the results in a different facility under different geometric and inflow conditions. The KRG's test section, for example, features a significantly smaller cross-section than the Transonic Wind Tunnel Göttingen (TWG), used in Birkemeyer (1999).

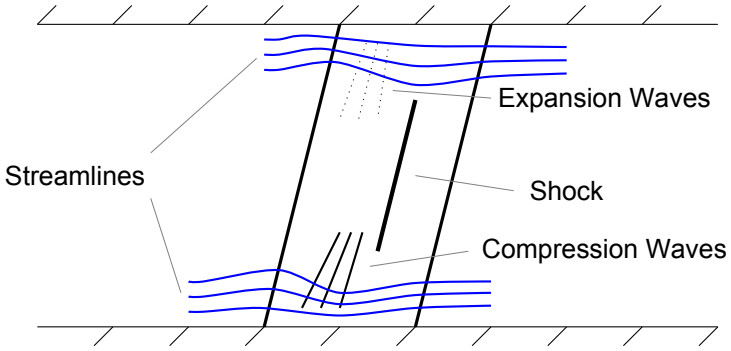

Figure 1.15: Side wall interference on a swept wing, following Birkemeyer (1999).

Corner Flows

A combination of both flows on the horizontal and side walls yields additional interference. This consists mainly of a corner boundary layer and secondary effects. The superposition of the boundary layers of the horizontal and side walls forms the boundary layer in the corner, which, as a result, thickens. The thicker boundary layer leads to a deceleration of the flow in the corners of the test section, which can influence the downstream flowfield (Shang and Hankey 1977).

Additionally, vortical structures can form in the corners, which are known as secondary effects. These secondary flow structures are shown schematically in Figure 1.16. It can be found that the velocity vectors point towards the corner and then away from the corner along the walls. If no countermeasures are applied, these corner flows may interact with shocks or simply influence the flowfield due to the presence of an alternated boundary layer (Hirt 2015; Shang and Hankey 1977). To avoid the influence of these structures in the flowfield, Hirt (2015) performed experiments in a supersonic wind tunnel at NASA Glenn Research Center. Therefore, eight corner fillet configurations, as illustrated in Figure 1.16, were tested. The fillets were made from a moldable material and differed in three parameters: the radius, the length, and the taper length from the square corner to the fillet radius, i.e., the distance from the start point of the fillet upstream to the location of constant radius. It was found that different fillet geometries cause variations in the boundary layer thickness at the corner and the tunnel centerline, resulting in a reduction in thickness at the corner and an increase in thickness at the centerline. Overall, the largest radii yielded the best combination of reducing boundary layer thickness in the corner while minimizing impacts on the tunnel centerline. The shorter fillet lengths resulted in thinner corner boundary layers, whereas the taper had no significant effect on the flow.

Despite the promising application of fillets to reduce corner flows, it is deemed too time-intensive to determine the exact geometric conditions required to impact the flow positively in this thesis.

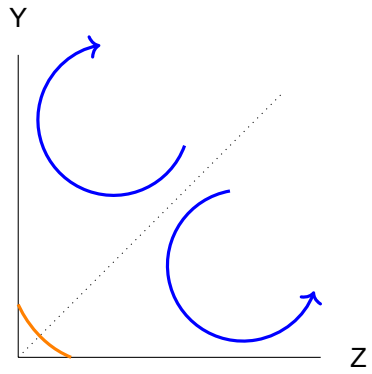

Figure 1.16: Schematic illustration of secondary flow structures in the corner of a wind tunnel test section, following Hirt (2015). The fillet is indicated in orange.

1.5. Discussion and Outline

The literature of the previous sections frames the knowledge gap of the research topic. To achieve carbon-neutral air transportation by 2050, extensive research is being conducted on drag reduction through the use of laminar flow. This requires a delay of laminar-to-turbulent transition and a detailed understanding of boundary layer stability. As today's transport aircraft typically fly at high subsonic Mach numbers, swept wings are essential for delaying the increase in wave drag at higher Mach numbers. To better understand the transition mechanisms on swept wings, numerical and experimental research is performed at DLR. Cryogenic facilities, such as the KRG, are used to achieve conditions similar to those of free flight. Nevertheless, the conditions in the test section of a wind tunnel differ from the unbounded case in free flight. The influence of the tunnel walls on the flowfield, which classical boundary corrections cannot correct, is of particular interest in this thesis. Birkemeyer (1999) performed studies on the influence of the horizontal and vertical walls on the flowfield and methods to reduce their influence, which are of specific relevance to this thesis.

In general, it can be noted that only very limited knowledge is available for swept wing experiments in the KRG. The only experiment conducted with a swept wing in this tunnel was performed by Egami et al. (2012) for the development of temperature-sensitive paint (TSP), where the scope of the experiment was not to quantify the influence of the tunnel walls on the flowfield, but to determine the influence of surface roughness on crossflow instability.

Nevertheless, it remains unknown under what conditions experiments with swept wings in the KRG can be performed to achieve results that represent the free-flight case. Thus, this study aims to numerically determine the influence of the tunnel walls on the spanwise flow homogeneity over a swept wing and to identify measures that can be taken to yield results closer to freestream conditions.

1.6. Research Questions and Objective

The literature review in the previous sections frames the research gap. Following that, research questions and the research objective can be derived.

1. **What is the effect of the side, top, and bottom wind tunnel walls on the spanwise flow homogeneity**
   (a) compared to an infinite-span swept wing?
   (b) with and without a shock present in the test section?
2. **How does a change in model- and freestream-related parameters affect the results from the first research question?**
   (a) Angle of attack
   (b) Sweep angle
   (c) Chord length
   (d) Mach number
3. **What other measures can be used to decrease the influence of the wind tunnel walls on the flow?**

The previous research questions frame the main research objective of this master's thesis:
To assess and quantify the influence of the vertical walls of the Cryogenic Ludwieg Tube Wind Tunnel Göttingen on the spanwise flow homogeneity for a swept wing by performing three-dimensional RANS simulations with the DLR TAU code.

To do so, the work is structured as follows. First, the experimental setup in the KRG is explained, providing an understanding of why the numerical work is structured in this manner. A brief introduction to the numerical simulation using the DLR TAU code is provided. Then, the meshing of different computational domains is explained. What follows is work on the validation and verification of the simulations based on experimental data, previously run simulations, and grid convergence studies. A major part of the thesis is based on mesh deformation, which is explained in the methodology chapter.
The results will be presented in a structured manner, starting with those for the setup that is currently achievable in the KRG's test section without any necessary adaptations, i.e., deformations. Next, results for simulations with deformed walls are presented. Specifically, the results with deformed inviscid and deformed viscous walls are presented. A brief section on alternative options for mitigating wall influences is presented before the conclusions are drawn, and recommendations for future work are provided.

2

Methodology

This chapter describes the methodology used for the following work. At first, the setup for experiments in the KRG is described. This includes a description of the airfoil used in the study, the working principle of the KRG, and two experimental test cases. The data for these test cases was acquired during experiments with an unswept wing in the KRG, performed by Koch et al. (2008). Furthermore, the numerical methodology is explained, with a focus on the DLR solver TAU, the hybrid meshing technique Chimera, and the difference in the choice of turbulence models. The following section outlines the validation and verification of the chosen method. The validation is performed by comparing numerical results with experimental results for an unswept wing in the KRG. The validation is assessed based on a comparison of numerical results with simulations performed by Köhler (2023) and a grid convergence study for two- and three-dimensional cases. Finally, mesh deformation is introduced, utilizing the TAU solver's built-in function to deform the surfaces and volumes of a grid. This deformation is used to deform the vertical and horizontal walls of the KRG's test section. Following the literature introduced in Section 1.4.3, a deformation can reduce the impact of the walls on the flowfield in the test section if applied correctly.

2.1. Experimental Setup in the KRG

This section provides insight into the KRG setup and two experimental test cases. The following illustrates the NLF airfoil used in this work, describes the KRG's architecture and working principle, and explains the experimental setup of experiments on an unswept wing conducted at the KRG. These introductions are essential for setting up the numerical simulations performed in this thesis and lay the foundation for interpreting the results obtained.

2.1.1. The LV2F Airfoil

The LV2F is an NLF airfoil, whose contour is shown in Figure 2.1. This airfoil has been investigated both experimentally and numerically in the KRG. Exemplary pressure distributions for an experiment and numerical simulations are displayed in Figure 2.11. Hence, the airfoil is a suitable choice for exploring the feasibility of conducting experiments with the LV2F airfoil in swept-wing configurations.

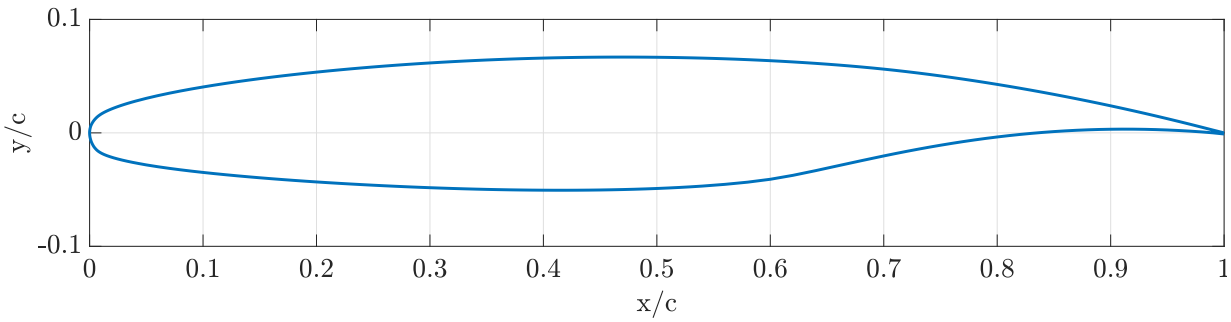

Figure 2.1: LV2F profile contour normalized by the chord length.

The goal of an NLF airfoil is to generate a low amount of drag by extending laminar flow while maintaining good high-lift characteristics. Thus, the shape is usually characterized by a relatively smooth upper surface. This facilitates a favorable pressure gradient on the surface, which is associated with a high amount of laminar flow due to a delay of the onset of Tollmien-Schlichting instabilities. For this reason, the aerospace industry puts effort into understanding and improving the technology. Airbus initiated its development effort in the 1990s but still needs to apply the technology to its aircraft (Hansen 2010).

2.1.2. The KRG Wind Tunnel

The KRG is a blow-down wind tunnel based on the Ludwieg-Tube concept for high Reynolds number research in transonic flow. Low temperatures of down to $100\,\mathrm{K}$ and high stagnation pressures of up to $1\,\mathrm{MPa}$ are achieved to realize Reynolds numbers of up to 60×10^6 based on a chord length of $150\,\mathrm{mm}$ (Rosemann 1995). Under these cryogenic conditions, it is possible to achieve dynamically similar conditions in transonic flow, with Mach numbers ranging from 0.3 to 0.95. Achieving these conditions is possible since the Mach and Reynolds numbers can be controlled independently of each other by adapting the pressure and the temperature.

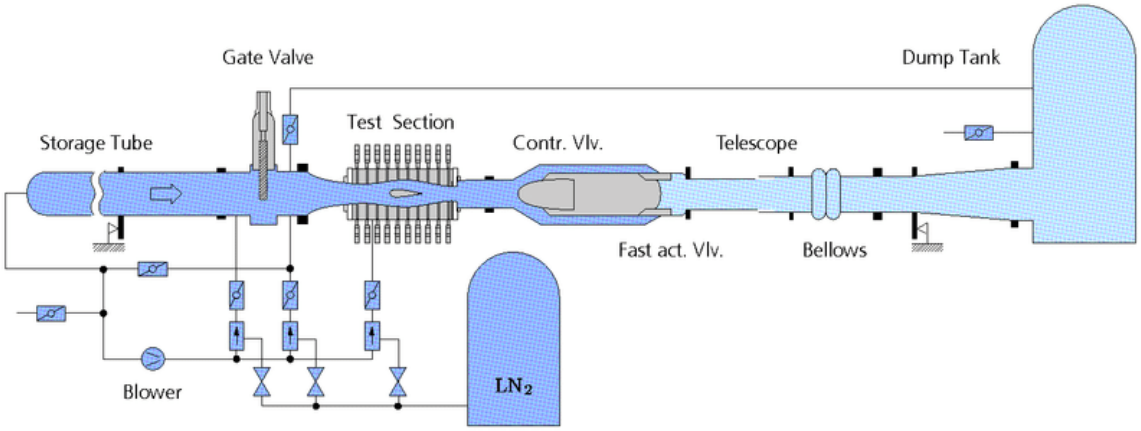

Figure 2.2: Schematic illustration of the Cryogenic Ludwieg Tube Göttingen (Koch et al. 2008).

Figure 2.2 shows a schematic illustration of the KRG. A long storage tube is necessary to enable significant runtimes, which for the KRG is roughly $130\,\mathrm{m}$ long (Rosemann 1995). Downstream of the storage tube, a gate valve is located to enable modifications in the test section without emptying the storage tube before a run, and to facilitate independent temperature control for both the flow and the model. Just upstream of the gate valve, the total temperature and pressure are measured, which, without losses, is the total pressure and temperature in the test section, too.
The test section is shown in Figure 2.3, where the aerodynamic object under study is placed. To increase the mean velocity and reduce the turbulence intensity level in the test section, a convergent nozzle with a contraction ratio of 3.6 connects the storage tube and the test section (Britcher and Landman 2023; Rosemann 1995). The increased flow quality is a result of the acceleration of the flow, which reduces the turbulent boundary layer height that develops in the long storage tube in front of the test section. The turbulence intensity level with respect to a quantity x is defined as

$$Tu_x = \frac{\sqrt{\overline{(x-\overline{x})^2}}}{\overline{x}} = \frac{\tilde{x}}{\overline{x}}. \tag{2.1}$$

Typically, turbulence intensity is expressed in terms of velocity. However, in cryogenic and transonic facilities like the KRG, measuring this quantity is challenging. Instead, the turbulence intensity level is expressed in terms of the total pressure or total temperature. For a Reynolds number of Re=$30 \times 10^6\,\mathrm{m}^{-1}$, a total temperature of $T_0 = 283\,\mathrm{K}$ and a Mach number of Ma = 0.78, the turbulence intensity level with

respect to the total pressure is $Tu_{p_0} = 0.0008$. Compared to the Transonic Cryogenic Tunnel at NASA Langley, this is over three times lower.
To compensate for the effects of the boundary layer created by the long build-up in the storage tube, the nozzle features a boundary layer bleed system. This system, depending on the boundary layer thickness, prevents the boundary layer from entering the test section. Just downstream of the test section entry, the static pressure is measured on the vertical walls and averaged across five pressure taps. The test section's cross-section is $0.4 \times 0.35\,\mathrm{m}^2$, and its length is $2.0\,\mathrm{m}$. The upper and lower walls are adaptive in two dimensions to control the pressure contour and achieve optimal flow conditions for the wind tunnel model, as explained in Section 1.4.3. The wall's contour is adjusted so that the velocity component normal to the wall, even in the absence of the wall, is zero. Thus, the influence of the upper and lower walls on the flowfield can be minimized. Due to the short runtime of the tunnel, using an iterative approach to determine the correct wall contour would require numerous iterations to achieve an interference-free result. To determine the correct wall contour, a single-step method can be employed to avoid costly iterative adaptations, utilizing the Cauchy integral formula, as presented by Rosemann (1995). The Cauchy integral formula allows the calculation of velocity components at any point within a closed curve by integrating the velocity components on that curve. Finally, it can be shown that the result of the Cauchy integral is only determined by singularities outside the closed curve, which represent the wall influence. This adaptation is not possible for the side walls. As shown in Section 1.4, expansion waves and shocks occur at the walls for high Mach numbers. This significantly influences the results of the experiment over the entire wing. Nevertheless, the boundary corrections introduced in Section 1.4.2 are not necessary to apply, as the horizontal walls can be deformed to eliminate the blockage and buoyancy effects.
The expansion downstream of the test section minimizes the losses in the tunnel. Downstream of the valves, the dump tank is located, which is maintained at atmospheric or lower pressure to create a pressure difference between the upstream and downstream sections of the test section.

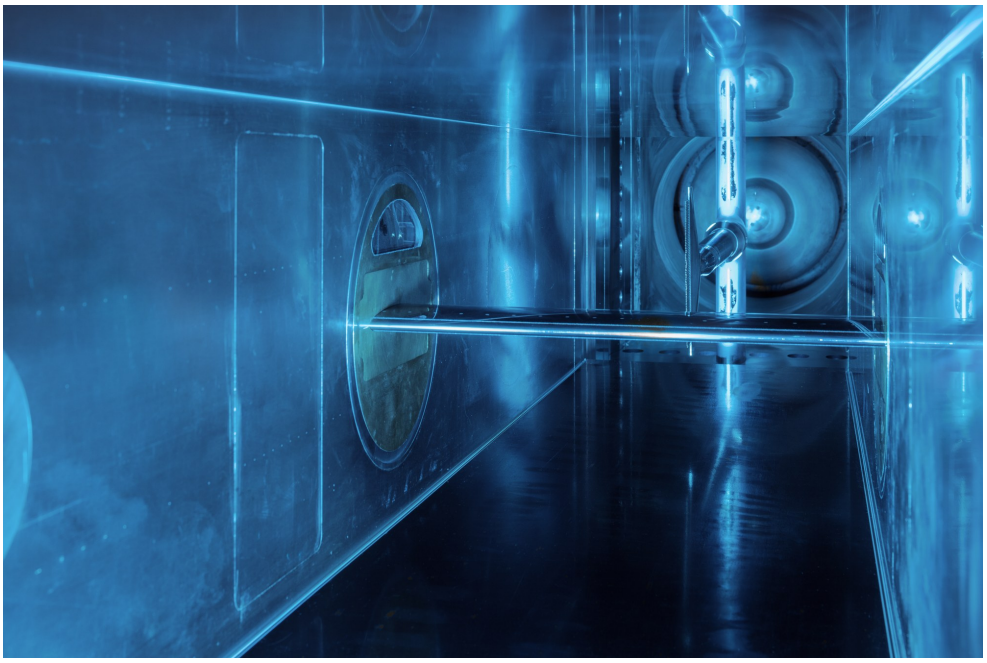

Figure 2.3: Test section of the Cryogenic Ludwieg Tube Göttingen[4]. View in flow direction with an unswept wing installed between the vertical walls. In the background, the wake rake and the control valve are visible.

Before the run, the storage tube and components upstream of the fast-acting valve are charged to the desired pressure. Liquid nitrogen is used to cool down this part of the facility. To initiate the run, the flow is triggered by opening the fast-acting valve, which causes expansion waves to travel upstream in the storage tube. This accelerates the fluid in the opposite direction, i.e., downstream. The usable runtime

[4]Accessed 23 May 2025. DLR (2025). *Cryogenic Ludwieg Tube Wind Tunnel, Göttingen (KRG)*. https://www.dlr.de/en/research-and-transfer/research-infrastructure/large-scale-research-facilities/cryogenic-ludwieg-tube-wind-tunnel-gottingen-krg

is limited to when the expansion waves return to the test section after being reflected at the end of the tube. Within this time window of 0.4 to 0.8 s, the conditions in the test section remain constant, allowing measurements to be taken. To ensure constant conditions, the actual test time is limited to roughly 0.1 s.

2.1.3. Test Cases of Interest

The results of the non-swept experiments performed in the KRG with the LV2F profile (Koch et al. 2008) are crucial for this thesis, as they validate the approach of using the TAU code. As the results of those experiments are restricted, the report cannot be cited in full length. However, the experimental setup and selected data can be shown. The experiment is performed with a non-tapered, unswept wing using the LV2F profile in the KRG. This section gives background information on the results obtained for the two-dimensional data, which is later compared to the numerical simulations for validation purposes.
Various inflow conditions are tested, of which two are presented in Table 2.1 for comparison with the numerical results. The cases are chosen so that one Mach number results in subsonic conditions, and the other in transonic conditions. Both cases are used to validate the numerical setup.

Table 2.1: Physical properties of experiments used for a comparison with the simulations (Koch et al. 2008). The experiment number corresponds to the identifier in the reference.

Experiment number	α in °	Ma	Re ($\cdot 10^6$)	T_s in K
With a shock on the pressure ($x/c \approx 0.65$) and suction side ($x/c \approx 0.7$)				
No015	0.0	0.7598	7.62	230.6
Without a shock				
No174	0.0	0.6993	9.01	173.5

Although the experiments are conducted on an NLF airfoil, which typically exhibits a large portion of laminar flow over its surface, the pressure measurements from the experiments deviate from those of the numerical simulations. As Köhler (2023) showed, the pressure coefficient distribution from the numerical simulations for a flow with a transition point in the aft part of the airfoil deviates from the experimental results. Instead, the pressure coefficient distributions from the fully turbulent simulations feature closer alignment with the measured pressure. The reason for the disagreement between the pressure data and the actual flow over the wing can be found in Figure 2.4. The figure shows experiment No174 (Koch et al. 2008), where the flow originates from the left. The model was equipped with temperature-sensitive paint to detect the laminar and turbulent regions of the flowfield. Although most of the flow around the wing is laminar until a chord length of roughly 70%, which is noticeable by the lighter colors, there are two turbulent wedges in the middle of the span, which start at the leading edge. Those turbulent regions appear as darker wedges in the TSP images. The red box indicates the positioning of the pressure taps. Those pressure taps are included on the surface of the airfoil to measure the pressure. Although they are staggered, i.e., not aligned in the chordwise direction to avoid influencing the downstream measurement, an influence of the downstream taps by the upstream taps can not be wholly avoided. In this case, the pressure taps are located entirely in a turbulent region. Thus, the measured pressure will align more closely with the simulation of a fully turbulent flow than with a laminar flow. This is later shown by a simulation, whose pressure coefficient distribution is shown in Figure 2.15.

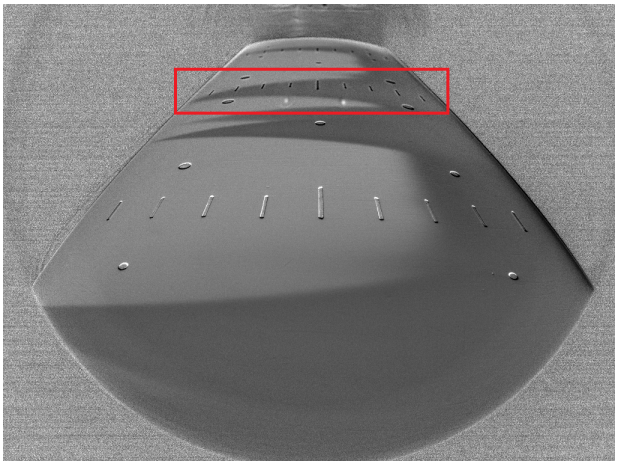

Figure 2.4: TSP measurements of experiment No174 with flow from the left (Koch et al. 2008). The flow transitions from laminar to turbulent at roughly 70% of the chord length (transition to darker color). For some spanwise locations, turbulent wedges form at the leading edge and travel downstream (dark wedges in the middle of the wing). The pressure taps are located in the middle of the span, where a turbulent wedge is formed.

2.2. Numerical Simulations with the DLR TAU Code

Numerical simulations using the DLR TAU code are employed as the research method in this thesis. Regarding fundamental research on laminar-to-turbulent transition, free-flight experiments are too expensive to be used on a regular basis. Experiments in wind tunnels can offer a more feasible approach, especially with wind tunnels operating at flight Reynolds and Mach numbers. Nevertheless, as shown in Section 1.4, there are limitations to the data that can efficiently be acquired by experimental work. As described by many authors, such as Ross (2023), a collaboration between computational fluid dynamics (CFD) and experimental work often yields the most valuable outcomes in a design process. This is why, nowadays, the use of CFD in the aerospace industry is crucial for understanding complex flow phenomena. Compared to a wind tunnel or full-scale experiment, CFD is hazard-free, cheap, and can be less complex (Anderson 1995). This effect is even more pronounced when cryogenic tunnels are used and limited knowledge is available for testing swept configurations in the tunnel. Thus, the use of CFD is considered the most appropriate method for investigating the unknown effects of the configuration in the tunnel.

The physical properties of a fluid are governed by three fundamental principles: the conservation of mass, the preservation of momentum, and the conservation of energy. The Navier-Stokes equations are a set of partial differential equations that describe the motion of viscous fluids. In CFD, these equations are approximated by discretized algebraic equations that can then be solved numerically (Anderson 1995).

This thesis utilizes the DLR TAU CFD code, specifically the version 2024.1.0, developed by the Institute of Aerodynamics and Flow Technologies (DLR 2024). The following section provides insight into the working principle of numerical simulations using the DLR TAU code. Initially, the finite volume discretization scheme is introduced, which is essential for understanding the meshing chosen for this work. Following this, various numerical grids are explained, and the Chimera approach is introduced, which is adopted in this work to minimize remeshing effort. A brief introduction to turbulence modeling in RANS simulations is provided, along with an overview of the concept of convergence in a simulation.

2.2.1. Discretization

The TAU solver uses a Finite-Volume (FV) discretization scheme, where the flow domain is subdivided into non-overlapping control volumes called cells, whose different forms will be explained in Section 2.2.2. The spatial discretization essentially breaks the continuous physical domain into cells, over which the flow variables are approximated. The flow variables are stored at the vertices of the grid, which is referred to as cell vertex spatial discretization (DLR 2024). Compared to cell-centered grids, this method typically incurs the cost of increased computational complexity but provides more accurate gradient approximations, especially near boundaries or in turbulent regions. For each control volume, the divergence theorem is applied to convert the volume integrals into surface integrals. This converts the fluxes into integrals

over the control surface (Ferziger and Peric 2002). Since these integrals cannot be computed analytically for complex flows and geometries, numerical approximation methods are used. The numerical scheme determines how the values from neighboring cells are used to approximate the fluxes. The TAU code uses upwind and central schemes for spatial discretization (DLR 2024). For upwind schemes, the flux at a control surface is approximated by using information from the upwind cell, which helps to stabilize the solution and reduce oscillations. Central schemes calculate the flux by averaging the values at neighboring cells, leading to higher accuracy but potentially less stability in the presence of sharp gradients. The simulations in this thesis are performed with a central scheme.

2.2.2. Numerical Grid

The numerical grid is a discrete representation of the geometric domain of the problem to be solved. The TAU code uses a finite volume scheme, as introduced in Section 2.2.1. The geometric domain of the problem is covered by a grid, consisting of non-overlapping cells. These grids have different topologies, which, for the purposes of this work, can be structured, unstructured, or hybrid.

Structured grids are characterized by all internal cells having a similar topology and the same number and type of connections. These cell shapes are usually quadrilateral in two dimensions and hexahedral in three dimensions. The advantage of structured grids lies in the more efficient memory usage and lower computing time per element compared to unstructured grids. Additionally, the effects of inserting errors, such as numerical diffusion, are reduced by aligning the cell faces orthogonal or parallel to the flow (Ferziger and Peric 2002). This is why structured grids are often used in regions where high-quality data is necessary, and the flow has a distinct mean flow direction. In this thesis, this is the case along the wind tunnel walls and wing surfaces, where achieving a high cell density is crucial. This is necessary to capture the strong velocity gradients in the boundary layer. At the same time, it is possible to easily increase the spacing of the grid cells as the distance to the wall increases, which maintains computational efficiency. On the contrary, creating structured cells around complex geometries is more challenging, and the computational cost increases.

In contrast, unstructured grid elements can have neighboring elements with an arbitrary topology, and there is no general rule governing their connectivity with neighbors. The cell shapes are usually triangular in two dimensions and tetrahedral in three dimensions (Ferziger and Peric 2002). Due to the unstructured nature of the elements, the numerical errors are usually much larger than for structured grids because the cell faces are not orthogonal to the mean flow direction. Despite their downsides, unstructured grids are commonly applied in numerical simulations due to their much higher flexibility, which also makes automatic grid generation easier for complex geometries, as used in this thesis for the volume of the tunnel test section (Wendt et al. 2009).

Overset Grids

Hybrid grids combine structured and unstructured elements. The method employed in this thesis is the Chimera approach, and its primary advantage is the high flexibility it allows for. It is possible to obtain high accuracy in refined regions while maintaining efficiency and simplicity in simpler regions (Wendt et al. 2009). Most simulations in this thesis are based on hybrid overset grids, which consist of structured elements near the tunnel walls and wing surfaces to accurately resolve the boundary layer, and unstructured elements in regions outside the boundary layer or further away from the walls, allowing for high flexibility. Nonetheless, the method has several shortcomings, including increased cost due to interpolation and reduced accuracy resulting from a mismatch in cell sizes between the meshes. Both meshes have to overlap at least one cell in order to get a converged solution, as shown in Figure 2.5. Without sufficient grid overlap, interpolation points may not have been allocated to a donor cell, so that the interpolation is not possible. The flow data at these so-called orphaned points will remain at farfield conditions, resulting in non-physical flow behavior at the block boundaries. An example of a correct interpolation region is shown in Figure 2.6. Here, interpolation occurs in the overlapped region of both meshes, indicated by the approximately squared box surrounding the airfoil. The shape of the interpolation region can be arbitrary and is chosen to be square. This enables a simple use for different combinations of wing geometries. During the simulation, outside the interpolation region, the flow equations are solved for the background mesh. The flow equations are solved for the child mesh inside the interpolation region. Hence, the background mesh inside the interpolation zone does not influence the results. The same applies to the child mesh outside the interpolation region.

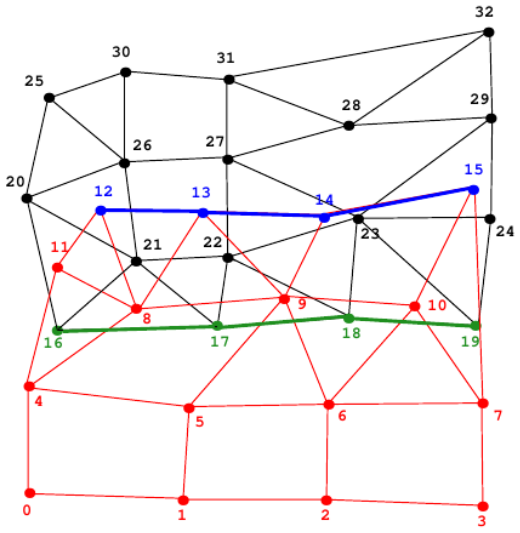

Figure 2.5: Overset grids system (DLR 2024). In red and black: first and second grid, respectively. In green and blue: the overlapping region where at least one cell has to overlap in order to get a converged solution.

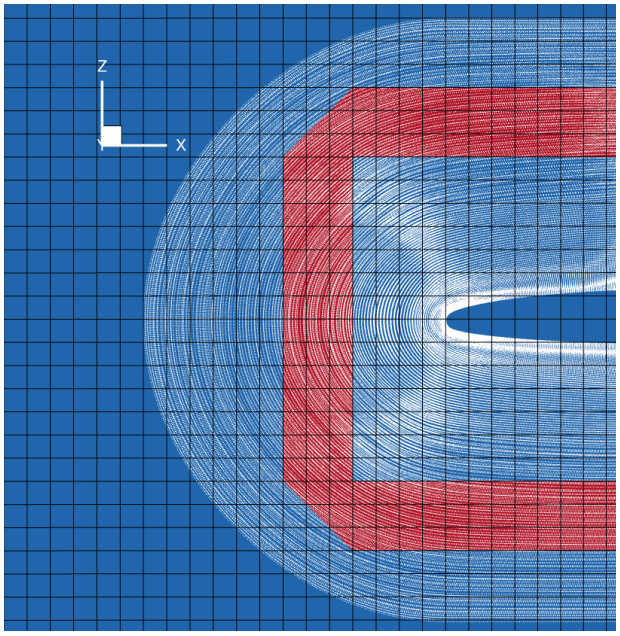

Figure 2.6: Overlapping background grid (blue with back lines) and child grid (white dotted lines) showing the interpolation region (red). The interpolation region follows a user-defined box.

Wall Functions

The dimensionless wall distance y^+ is a crucial measure in CFD for determining the near-wall behavior of the flow. A major part of the turbulence production happens at $y^+ < 20$, whereas the wall shear can only be accurately computed if $y^+ \approx 1$ for the first cell (Ferziger and Peric 2002). The dimensionless wall distance is defined as

$$y^+ = \frac{y \cdot v_\tau}{\nu} = \frac{y \cdot \sqrt{\frac{\tau_w}{\rho}}}{\nu} = \frac{y \cdot \sqrt{\frac{1}{2} C_f v_\infty^2}}{\nu}, \tag{2.2}$$

where y is the absolute distance from the wall, v_τ the friction velocity, τ_w the wall shear stress, and ν the kinematic viscosity. From Equation 2.2 it can be found that for a given flow, there is a certain absolute wall distance corresponding to the before-mentioned dimensionless wall distance of $y^+ = 1$. This absolute wall

distance should be aimed for as the first cell height to accurately compute the wall shear.
Although the first cell height for the computations corresponded to $y^+ = 1$, the simulations did not converge. This difficulty often arises in high Reynolds number flows, where resolving the viscous sublayer necessitates a very fine mesh near the wall. To enable convergence, wall functions are employed in this thesis by setting the ”use wall function” parameter in TAU. Wall functions provide a boundary condition at solid walls, enabling flow solutions that are independent of the location of the first grid node. The boundary condition prescribes the wall shear stress and enforces no penetration at the wall while allowing coarser near-wall meshes with higher y^+ values. In TAU, the wall function implementation is based on directly prescribing the viscous fluxes at the wall boundary. The inviscid fluxes across the wall disappear, and the wall cells, whose nodes are located on the boundary, require a suitable specification of viscous fluxes. For the hybrid wall function boundary condition, the wall shear stress vector τ_w is projected onto the wall-parallel direction, and the wall-normal component is neglected. The RANS equations are then only solved down to the first grid node and matched with an adaptive wall function solution at the first grid node above the wall $v_{RANS}(y_\delta) = v_{WF}(y_\delta)$.

2.2.3. Turbulence Models

As shown in Section 1.2, most flows in engineering applications are turbulent. Often, knowing only a few quantitative flow properties, such as the average forces on a body, is enough instead of resolving these turbulent structures entirely. In this case, performing expensive direct numerical simulations (DNS) or large eddy simulations (LES) can be avoided. Instead, cheaper Reynolds-Averaged Navier-Stokes (RANS) approaches solve the Navier-Stokes equations for the steady mean solution.

The derivation of the RANS equations is based on the Navier-Stokes equations. For a Newtonian, compressible fluid with constant specific heats and no external body forces, the governing equations for mass, momentum, and energy are

$$\frac{\partial \rho}{\partial t} + \frac{\partial}{\partial x_j}(\rho v_j) = 0, \tag{2.3}$$

$$\frac{\partial}{\partial t}(\rho v_i) + \frac{\partial}{\partial x_j}(\rho v_i v_j) = -\frac{\partial p}{\partial x_i} + \frac{\partial \tau_{ij}}{\partial x_j}, \tag{2.4}$$

$$\frac{\partial}{\partial t}(\rho E) + \frac{\partial}{\partial x_j}\left[(\rho E + p) v_j\right] = \frac{\partial}{\partial x_j}\left(\tau_{ij} v_i - q_j\right), \tag{2.5}$$

where v is the velocity, x the position, t the time, and τ_{ij} the viscous stress tensor. For a Newtonian fluid, it is given by

$$\tau_{ij} = \mu\left(\frac{\partial v_i}{\partial x_j} + \frac{\partial v_j}{\partial x_i}\right) - \frac{2}{3}\mu\delta_{ij}\frac{\partial v_k}{\partial x_k}, \tag{2.6}$$

where μ is the constant dynamic viscosity and δ_{ij} is the Kronecker delta. E is the total specific energy and q_j is the heat flux.

To close the system of equations, the equation of state for an ideal gas is used

$$p = \rho R T, \tag{2.7}$$

where R is the specific gas constant.

In turbulent flows, the instantaneous flow variables exhibit random fluctuations. These can be decomposed using Reynolds decomposition:

$$\phi(x,t) = \overline{\phi}(x) + \phi'(x,t), \tag{2.8}$$

where $\overline{\phi}$ is the time-averaged component and ϕ' the fluctuating component. The time average is defined as:

$$\overline{\phi} = \lim_{T\to\infty} \frac{1}{T}\int_0^T \phi(t)\, dt. \tag{2.9}$$

For compressible flows, it is more appropriate to use Favre averaging (density-weighted averaging)

$$\tilde{\phi} = \frac{\overline{\rho\phi}}{\overline{\rho}}, \qquad \phi'' = \phi - \tilde{\phi}, \tag{2.10}$$

where $\tilde{\phi}$ is the Favre-averaged quantity and ϕ'' the corresponding fluctuation.

Applying Reynolds and Favre averaging to the compressible Navier–Stokes equations yields the compressible Reynolds-Averaged Navier–Stokes (RANS) equations. These include additional terms that arise due to the averaging process and account for the effects of turbulence. In particular, the momentum equations contain the Reynolds stress tensor (RST)

$$-\overline{\rho v_i'' v_j''}, \tag{2.11}$$

which introduces a closure problem. To model this term, the Boussinesq hypothesis (Boussinesq 1903) is commonly employed

$$-\overline{\rho v_i'' v_j''} \approx \mu_t \left(\frac{\partial \tilde{v}_i}{\partial x_j} + \frac{\partial \tilde{v}_j}{\partial x_i} \right) - \frac{2}{3}\rho k \delta_{ij}, \tag{2.12}$$

where μ_t is the turbulent viscosity, and k is the turbulent kinetic energy.

The resulting compressible RANS equations form a closed system only when completed by appropriate turbulence models. Standard models include the Spalart–Allmaras (SA) model or the k–ω model. These models are essential for predicting turbulent transport phenomena and enable accurate simulation of compressible flows.

Spalart-Allmaras Model
The Spalart-Allmaras (SA) turbulence model is an eddy viscosity model introduced by Spalart and Allmaras (1992). It solves one transport equation for a single scalar variable, the SA viscosity $\tilde{\nu}$ (DLR 2024):

$$\frac{\partial \tilde{\nu}}{\partial t} + v_j \frac{\partial \tilde{\nu}}{\partial x_j} = c_{b1}(1 - f_{t2})\tilde{S}\tilde{\nu} - (c_{w1} f_w - \frac{c_{b1}}{\kappa^2} f_{t2})(\frac{\tilde{\nu}}{d})^2 + \frac{1}{\sigma}(\frac{\partial}{\partial x_j}((\nu + \tilde{\nu})\frac{\partial \tilde{\nu}}{\partial x_j}) + c_{b2}\frac{\partial \tilde{\nu}}{\partial x_i}\frac{\partial \tilde{\nu}}{\partial x_i}), \tag{2.13}$$

with v_j being the mean velocity components, d the distance to the closest wall, $\tilde{S}$ the modified vorticity magnitude, $c_{b1}, c_{b2}, c_{w1}, \kappa, \sigma$ constants, and f_w, f_{t2} being empirical functions. Once solved for the SA viscosity, it can be used to compute the eddy viscosity $\nu_t = \tilde{\nu} f_{v1}$, where f_{v1} is another empirical function. The eddy viscosity can then be used in the RANS equations to determine the Reynolds stress tensor (RST). The model is robust and computationally efficient because it only requires one transport equation to be solved. However, it is, for example, less suitable for simulating flow reattachment (Wendt et al. 2009).

$k - \omega$ Model
The $k - \omega$ SST model by Menter is a two-equation eddy viscosity model that solves the transport equations for the turbulent kinetic energy k and the specific dissipation rate ω (DLR 2024):

$$\frac{\partial k}{\partial t} + \frac{\partial V_j k}{\partial x_j} = P_k - \beta^\star k\omega + \frac{\partial}{\partial x_j}((\nu + \sigma_k \nu_t)\frac{\partial k}{\partial x_j}), \tag{2.14}$$

$$\frac{\partial \omega}{\partial t} + \frac{\partial V_j \omega}{\partial x_j} = \frac{\gamma}{\nu_t} P_k - \beta\omega^2 + \frac{\partial}{\partial x_j}((\nu + \sigma_\omega \nu_t)\frac{\partial \omega}{\partial x_j}) + 2(1 - F_1)\frac{\sigma_{\omega 2}}{\omega}\frac{\partial k}{\partial x_j}\frac{\partial \omega}{\partial x_j}, \tag{2.15}$$

where P_k is the production of turbulent kinetic energy, $\beta^\star, \sigma_k, \gamma, \beta$ constants, ν_t the turbulent viscosity, and F_1 a blending function which switches between the $k - \omega$ and $k - \epsilon$ model, which is a different turbulence model which will not be used in the present work. The turbulent viscosity can then be used to determine the RST in the RANS equations. The SST model is computationally more expensive than the SA model, but it yields good results for boundary layer flows, even in regions with flow separation.

2.2.4. Convergence

The error in a numerical simulation refers to the difference between the true solution of the mathematical problem, which is usually unknown, and the numerical solution obtained from the simulation (Ferziger and

Peric 2002). In other words, it describes how close the numerical solution is to the true solution.
The residual R of a numerical simulation measures how well the numerical solution satisfies the governing equations of the problem. It is defined as the imbalance that remains when the numerical solution is substituted into the original equations. A small residual indicates that the numerical solution is close to satisfying the governing equations, but it does not necessarily imply a small error.

A numerical simulation needs to satisfy spatial and temporal convergence (Wendt et al. 2009). The spatial convergence is verified by performing calculations on successively refined grids. The solution should then converge to a grid-independent solution. This process is referred to as a grid convergence study and is performed in this thesis by comparing at least three refined meshes, where the two finer grids are expected to yield the same solutions, while the coarsest mesh may exhibit different solutions. Additionally, the temporal convergence is studied to determine the necessary residual for a converged solution. When temporally converged, the solution should not differ from a solution with an even lower residual. The temporal convergence is studied by comparing the results of a simulation at different residuals.

2.3. Method Validation and Verification

This section explains the validation and verification steps performed for this thesis. For validation purposes, a comparison is made with experimental data gathered in the KRG using an unswept LV2F profile. The verification is performed by comparing the simulations with previous results from a numerical study conducted by Köhler (2023) and through grid convergence studies. As sufficient data has been obtained for the experiments, verification is performed under the same conditions as validation, in accordance with the experimental data. The method and computational domains used in this work differ significantly from the ones used by Köhler (2023). The cited work did not use the Chimera approach to combine the structured and unstructured parts of the grid. Instead, a re-meshing was performed for every variation in geometry. Due to a wide range of geometries and computational domains used in the present work, the Chimera approach was chosen to combine a variety of background and child grids. The following sections provide insights into the chosen computational domains, mesh generation, and simulations performed for the grid convergence studies.

2.3.1. Computational Domain

As was already mentioned in Section 2.1.2, the test section of the KRG is $2\,\text{m}$ long, $0.4\,\text{m}$ wide, and at the entrance of the test section $0.35\,\text{m}$ high. The horizontal walls can be adapted two-dimensionally. In the following, two computational domains are chosen. Both domains are limited to the geometry of the test section and do not include other parts of the tunnel, such as the storage tube or the contraction. This is done because sufficient convergence was achieved by simulating the test section alone, and to reduce computational time and cost by reducing the domain size. Although this introduces inaccuracies due to an inaccurate representation of the entire tunnel, the author suspects only a minor deviation. Due to the contraction, the flow quality and direction are aligned with the tunnel walls, and the difference is considered small. The part of the tunnel that is used for the computations is shown in a lighter color in Figure 2.7. The origin of the coordinate system is located in the middle (Y- and Z-location) of the test section entry. The most forward point of the wing is located at $P_1(0.93\,\text{m},\ -0.2\,\text{m},\ 0\,\text{m})$.

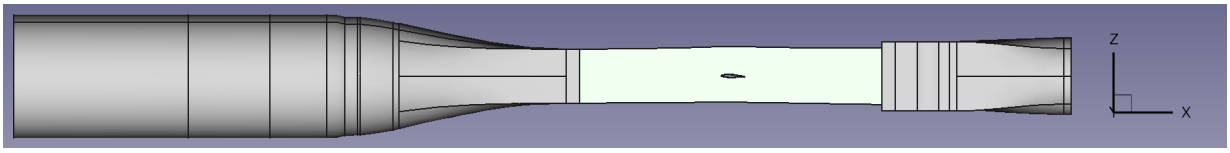

Figure 2.7: KRG model with storage tube, contraction, test section, and diverging part in the X-Z-plane. The relevant section for the domain is shown in a lighter color, spanning from the test section entry upstream to the test section exit downstream.

At first, a domain is chosen that represents the test section's geometry in X- and Y-directions, but does not represent the test section's Z-direction correctly, and has the upper and lower walls placed at a significant distance from the wing of roughly 13 times the chord length. The shape of the domain can be found in Figure 2.8a and will be referred to as "Domain 1" in the following chapters. Extending the distance

of the horizontal walls from the wing isolates the effect of the side walls and the horizontal walls on the flowfield because the influence of the horizontal walls is essentially eliminated. For this domain, the impact of the vertical, i.e., side walls, on the flowfield can be studied. Although this does not represent the actual geometry of the KRG's test section, it is representative of a test section where upper and lower walls can be adapted in three dimensions, as this, when done perfectly, eliminates the influence of those walls on the flowfield.
The second domain represents the actual test section's geometry, where the X- and Y-components are identical to the ones in Domain 1, but the Z-component differs. Instead of placing the upper and lower walls at a distance, they are placed at the actual location in the test section, as shown in Figure 2.8b. This domain, further referred to as "Domain 2", represents the current possibilities in the KRG and combines the effects of vertical and horizontal walls on the flowfield.
In both domains, the surfaces of the wing are simulated as viscous walls. The wind tunnel walls are simulated as either inviscid or viscous, depending on the section for which the results are presented. The type of walls used will be indicated in each section. Finally, both domains use a reservoir-pressure inflow and an exit-pressure outflow as in- and outlet conditions, respectively. The reservoir-pressure inflow defines the turbulent intensity, total pressure, and total temperature. The exit-pressure outflow defines a measured static pressure and the corresponding measurement location inside the domain. The measurement point is $P_2(0.5\,\text{m}, 0\,\text{m}, 0\,\text{m})$, i.e., the point of measurement is located upstream of the wing, at one quarter of the test section length and in the middle between the side tunnel walls and the upper and lower tunnel walls. This point is appropriate, as in reality, the pressure in the tunnel is measured shortly after the entry into the test section. By specifying the total and static pressures, the Mach number is implicitly defined because it can be calculated using the isentropic flow equations.

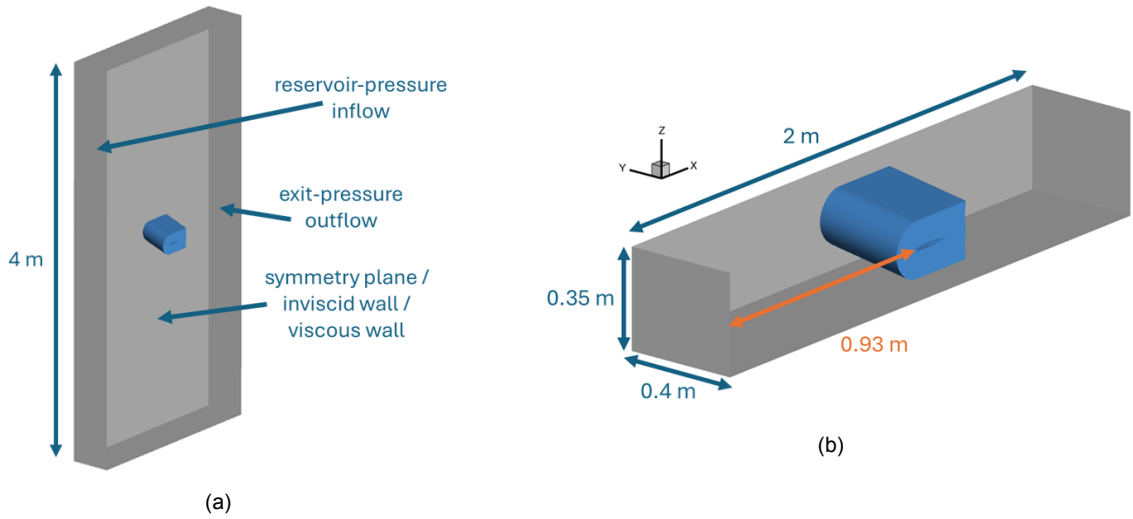

Figure 2.8: Computational domains used in this thesis. The child grid is indicated in blue. The lengths of the domain are indicated with blue arrows. The distance between the leading edge of the wing at the inboard wall and the entry to the test section is indicated in orange. (a) With extended horizontal walls to eliminate their influence. (b) Representing the actual test section geometry.

For comparison, results based on computations on Domain 1 and 2 are presented alongside infinitely swept wing computations, which are based on a domain introduced in Köhler (2023). The shape of the domains differs significantly, as the domain used for the infinitely swept wing simulations is circular, as shown in Figure 2.9, and uses a farfield condition. The mesh is based on the same child mesh used for Domains 1 and 2, extended to the farfield by unstructured cells. The distance of the farfield to the airfoil is roughly 100 times the chord length of the wing.
The main difference between the domains lies in the nature of the inflow. While the flow must enter the test section horizontally for the reservoir-pressure inflow used in this work, the flow can enter the circular domain with a farfield condition at any angle. Thus, the circular domain will represent the unbounded condition for an infinitely swept wing closer. The curvature of the streamlines in the unbounded case will be larger, and thus, the perceived angle of attack will be larger than for the simulations performed in

this thesis, even at the same geometric angle of attack. To compare the flowfield around the wings, this difference must nevertheless be taken into account, which is achieved by comparing the perceived angle of attack for simulations on different domains with the same geometric angle of attack. The location to assess the angle of attack is the measurement point P_2 shown above, where the X- and Z-velocities are compared to determine the local angle of the flow. The infinitely swept wing simulations based on the domain of Köhler (2023) are consequently repeated with the reduced inflow angle of attack in the farfield. The results are, for example, shown in Figure 2.11 and Figure 2.16.

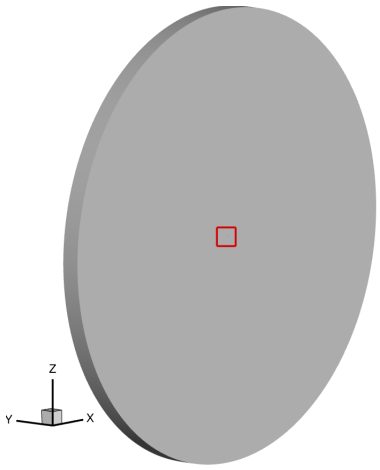

Figure 2.9: Computational domain based on Köhler (2023) used for the infinitely swept wing simulations. The position of the wing is indicated in red.

If not stated otherwise, a central scheme is employed as a discretization method for the convective fluxes of the RANS equations, the one-equation Spalart-Allmaras turbulence model is used, and a multigrid method is used to accelerate the convergence. All simulations are performed under the assumption of fully turbulent flow.

2.3.2. Two-Dimensional Mesh Generation

Simulations with a two-dimensional mesh are performed first, which are compared to the results from experiments (Koch et al. 2008) and simulations performed on a grid by Köhler (2023). The simulations are referred to as two-dimensional because an unswept wing is simulated with only one cell in the spanwise direction. This cell in the spanwise direction is necessary for TAU to perform computations.

A grid convergence study is performed for this two-dimensional case to prove the independence of the solution from the computational mesh. Therefore, simulations with the same parameters are performed on different computational meshes, which differ in the number and spacing of grid cells. The computational domain, with extended horizontal walls, as shown in Figure 2.8a, is chosen for this simulation. Since the two-dimensional wall adaptation, which can be performed in the KRG, eliminates the effects of the upper and lower walls on the flowfield, this domain is suitable in this case.

The domain consists of two grids, which are combined by the Chimera method, and shown in Figure 2.10. The background grid, which meshes the tunnel with its extended horizontal walls, comprises $400\,000$ unstructured cells and is created using the meshing software Fidelity Pointwise[5]. The child grid, which meshes the airfoil, consists of structured cells and is created with the meshing program MegaCads (Brodersen 1999). For the grid convergence study, the child grid is modified to obtain grid-independent solutions, as this will have a larger effect on the result than modifying the background grid. The number of cells for each computational grid is shown in Table 2.2, where the different number of cells stems from a change in wall-normal and wall-tangential direction. The grid convergence study is performed using the parameters of experiment No015, which are shown in Table 2.1, since the Mach number is sufficiently high. The shock that forms above the surface of the airfoil is expected to produce high gradients

[5]Accessed 27 May 2025. Cadence (2025). *Fidelity Pointwise for CFD Meshing*. https://www.cadence.com/home/tools/system-analysis/computational-fluid-dynamics/fidelity.html

in the flow field, allowing for adequate testing of convergence. This allows the use of the mesh for all subsequent simulations because the Mach number for all subsequent simulations will not be higher than that for experiment No015.

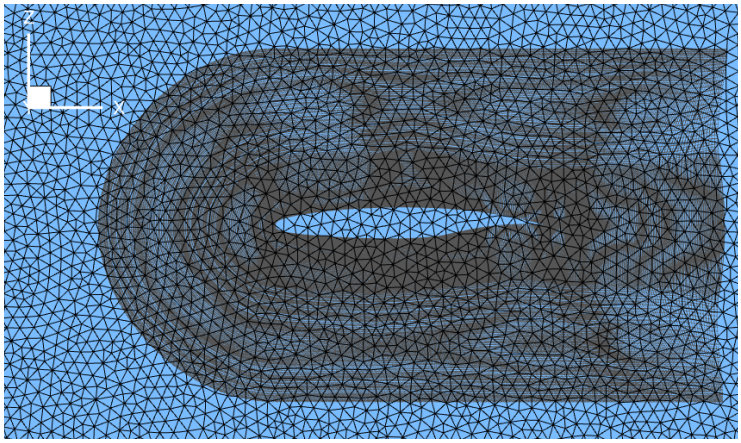

Figure 2.10: Unstructured background mesh (black on blue) and structured child mesh (grey) shown with the airfoil in the X-Z-plane for two-dimensional simulations. The combination of both meshes is done with the Chimera method.

The chosen grid Reference features 527 points in the wall-tangential direction on both the upper and lower surfaces, with a denser spacing at the leading and trailing edges, as well as at the expected shock location. The boundary layer features 51 points in the wall-normal direction, followed by 101 points until the boundary of the child mesh. The structured mesh extends around the airfoil by roughly two-thirds of the chord length.

Table 2.2: Number of cells for the computational grids of the airfoil for the grid convergence study of two-dimensional simulations.

Computational Grid	Coarse	Reference	Fine
Number of cells	171 072	196 992	209 152

2.3.3. Two-Dimensional Simulations

The simulations are performed on the computational grid referred to as Reference, introduced in Section 2.3.2. In addition to the boundary conditions explained in Section 2.3.1, the simulations are performed using Euler walls, i.e., walls without viscous effects, as the horizontal tunnel walls, and symmetry planes as side walls. The solver settings are given in Appendix A.

In a first step, the grid convergence study for the two-dimensional case is performed. For the grid convergence studies, the pressure coefficient distributions over the airfoil's surface obtained from different computational grids are compared. The reason why the pressure coefficient distribution and no integral quantity, such as lift or drag coefficient, are compared lies in the fact that this approach does not cancel out local effects. For example, the lift coefficient can be overall constant but increased towards the leading edge and reduced towards the trailing edge.
As Figure 2.11 shows, the pressure coefficient distribution of the three meshes, Coarse, Reference, and Fine, align closely for almost the entire wing. The most significant difference is observed in Figure 2.12 at the location of the shock on the upper surface for $0.65 < x/c < 0.75$, where the pressure coefficient distributions of the finer and reference meshes align nearly perfectly. In contrast, the coarser mesh results in a slight shift upstream of the shock location. Hence, the reference mesh can be used for further simulations, as the spacing of the grid cells is sufficiently fine for a grid-independent solution.

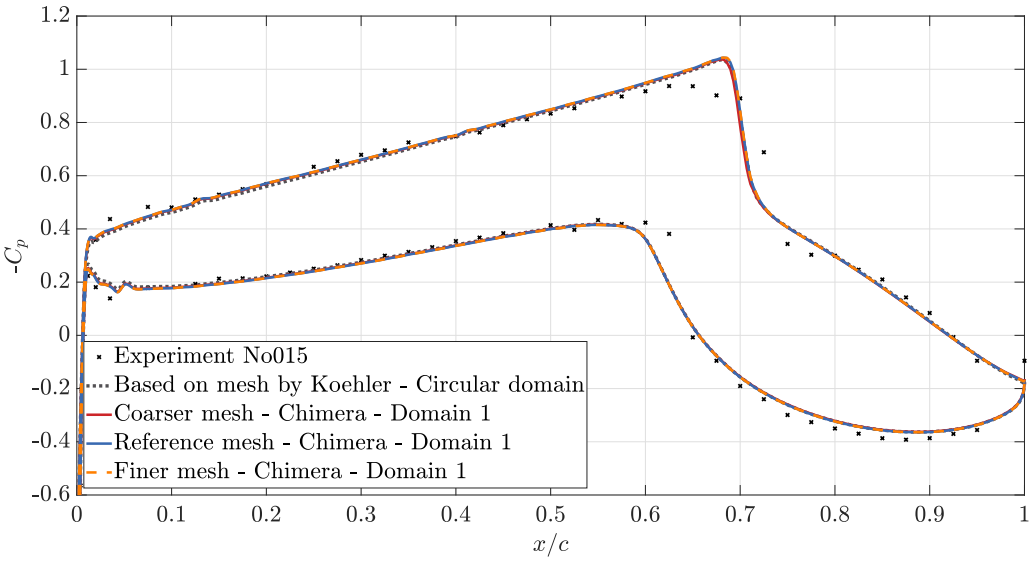

Figure 2.11: Pressure coefficient distributions for the two-dimensional spatial grid convergence study with the grid parameters shown in Table 2.2 and the parameters of experiment No015 shown in Table 2.1. The simulations based on the grid by Köhler (2023) are corrected for the angle of attack to match the angle of attack perceived by the airfoil in the test section of the tunnel.

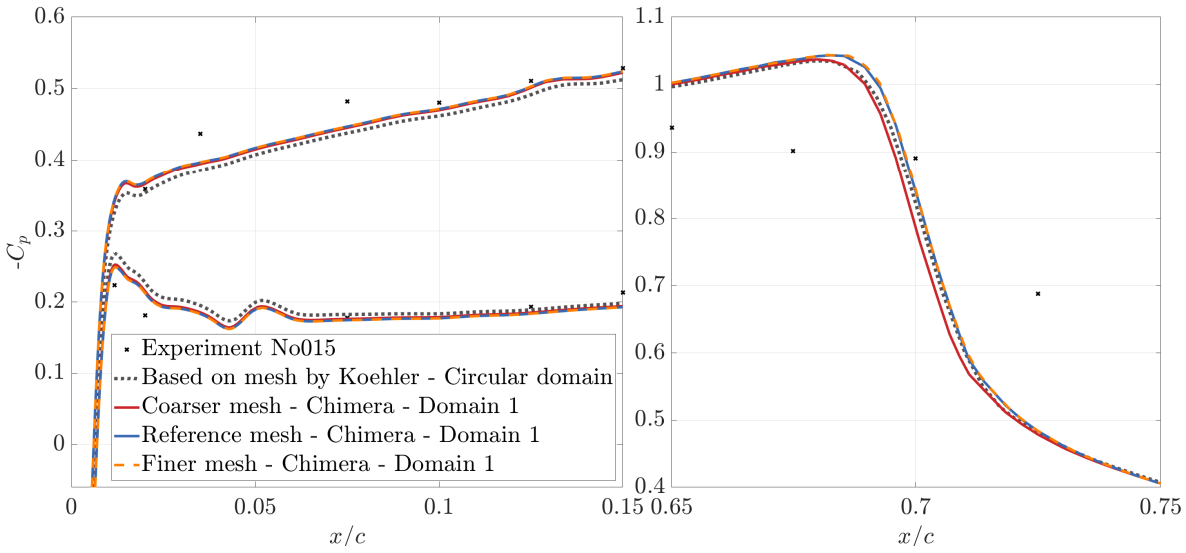

Figure 2.12: Zoom-In of Figure 2.11

Overall, close alignment with the experimental data is observed. The most significant disagreement is in the region of the shock on the wing's suction surface. Compared to the experimental data, the simulations differ on the suction side for $0.6 < x/c < 0.75$ and on the pressure side for $0.6 < x/c < 0.65$. The difference might stem from the experiment or have numerical reasons, such as the modeling of turbulence, which will be discussed later. During the experiment, even slight deviations from the reference Mach number or the angle of attack can already cause a significant alteration in the pressure on the wing. Additionally, the discrete measurement of pressures introduces inaccuracies when attempting to determine the correct location of the shock. The pressure coefficient curve in the front part of the pressure surface of the wing is shown in Figure 2.12. What stands out is the wiggly trend of the pressure in the forward-most 5% of the

airfoil. As this could be related to numerical issues, the close alignment of the trend with the experimental data suggests a physical reason behind the behavior.

Notably, the difference between the reference mesh and the simulations performed by Köhler (2023) is interesting to observe. The shock location of the reference mesh is shifted slightly downstream by $\Delta x/c = 0.0008$. Also noticeable is the difference in pressure coefficient from the simulations performed with the reference mesh and the mesh from Köhler (2023) in the front of the airfoil, particularly for $x/c < 0.15$, which is displayed in Figure 2.12. Here, the simulations performed within this thesis overpredict the lift compared to those in previous studies. The difference to the results obtained based on the grid by Köhler (2023) is thought to be twofold. First, the computational grids on which the simulations were performed differ, particularly in terms of the Chimera setup. Although a grid convergence study was performed for both grids, slight deviations may still occur. This effect is believed to be small, and the difference in the computational domain, as explained in Section 2.3.1, accounts for the primary difference in pressure coefficient distribution. To account for this effect, the simulations performed based on a grid by Köhler (2023) are corrected for by an angle of attack, specifically, the angle of attack at the farfield conditions is reduced by $\Delta\alpha = -0.1198°$. The difference between the pressure coefficient distributions most likely stems from the inaccuracies in this correction procedure, as iterations would be necessary to eliminate the error completely.
What stands out in Figure 2.11 and Figure 2.12 are the wiggles in the pressure coefficient, especially pronounced on the pressure surface at $0.01 < x/c < 0.07$, on the suction surface at $0.12 < x/c < 0.14$, and on the suction surface at $0.41 < x/c < 0.43$. As will be observed in the following two- and three-dimensional simulations at various angles of attack, sweep angles, chord lengths, and Mach numbers, these wiggles are consistently present in all simulations. The wiggles on the pressure surface can even be found in the experimental data. Since these wiggles occur in all cases and the simulations are performed fully turbulent, it is likely that they are caused by an imperfect specification of the airfoil shape. Minor imperfections in the location of single points can cause the surface of the airfoil to feature minor bumps, which can lead to pressure oscillations.

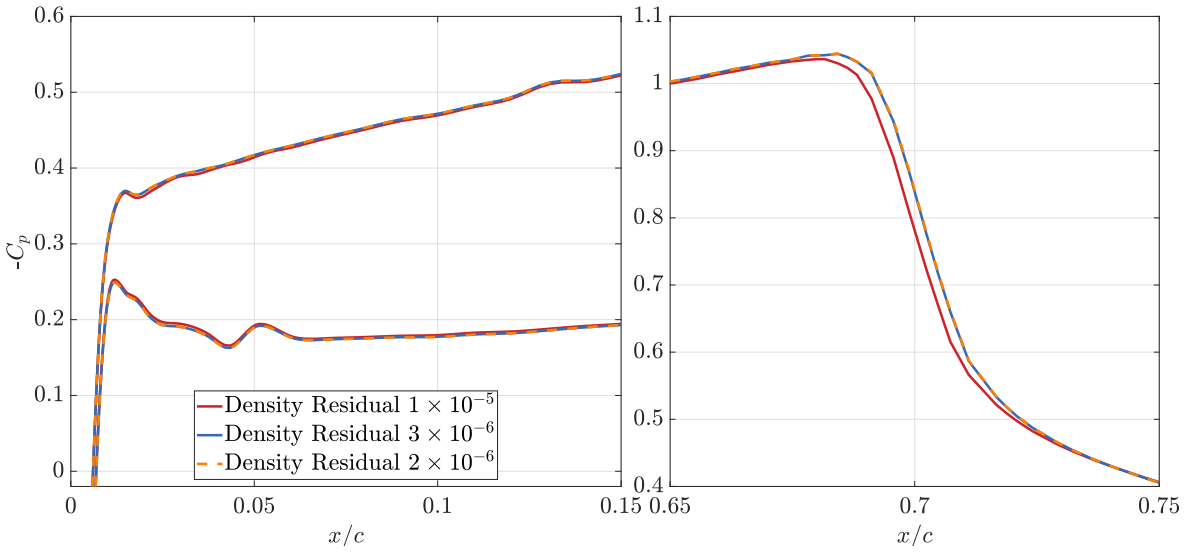

Figure 2.13: Pressure coefficient distributions plotted along the normalized chord length for the two-dimensional temporal convergence study with the parameters of experiment No015.

In addition to the grid convergence study, the convergence history, i.e., the temporal convergence, is examined to determine the minimum residual required for a converged solution. Figure 2.13 shows the pressure coefficient distributions for simulations performed with the Reference grid obtained from the grid convergence study. The chosen results are for density residuals that are low enough to align closely overall. The only noticeable difference between the curves is in the location of the shock on the suction surface of the airfoil, specifically within the range $0.65 < x/c < 0.75$. Figure 2.13 shows the regions in the

front and at the location of the shock, closer. The solution for a density residual of 1×10^{-5} has not yet converged. From these simulations, it is found that the density residual should be at least 3×10^{-6}. A lower residual will no longer increase the accuracy of the pressure coefficient distribution. The corresponding plot for the density residual, the lift coefficient C_L, and the drag coefficient C_D over the number of iterations is shown in Figure 2.14 with a logarithmic scale.

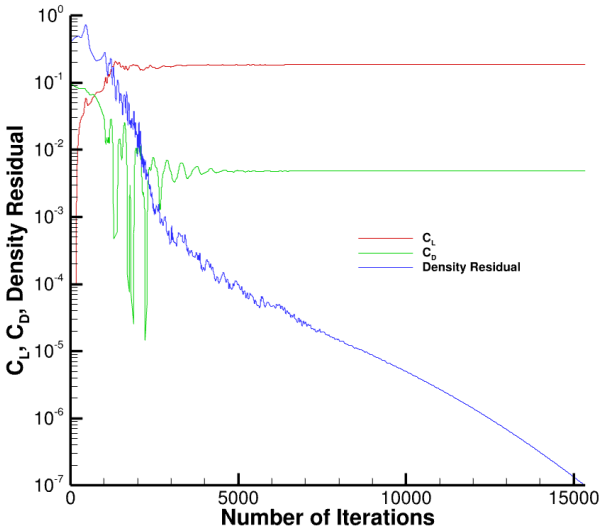

Figure 2.14: Lift coefficient, drag coefficient, and density residual for the number of iterations plotted logarithmically for the two-dimensional convergence history with the parameters of experiment No015. A density residual lower than 3×10^{-6} will not further increase the accuracy of the pressure coefficient distribution.

Additionally, several simulations are performed to verify the approach in three dimensions, using the Chimera technique, and with a different turbulence model:

First, a three-dimensional simulation with an unswept wing is performed. The child grid is extruded in the Y-direction with 40 equally spaced cells, resulting in a total of 7.8 million structured cells. The background grid of the tunnel is meshed with half the grid spacing in the Y-direction. Euler walls are used as side walls in the tunnel, as opposed to the symmetry planes used for two-dimensional simulations. Nevertheless, the wing is still unswept in these simulations. As is clearly visible in Figure 2.15, the pressure coefficient distributions from the two- and three-dimensional simulations extracted in the middle of the tunnel align almost perfectly. This verifies that the chosen approach can be transferred to three dimensions.

A verification of the Chimera method is performed by comparing the pressure coefficient distributions with those from a simulation where the child grid is meshed within the domain of the background grid in Fidelity Pointwise. The connections between the structured and unstructured cells are thus created during the mesh generation, making the Chimera approach superfluous. The same spacing for the unstructured cells was used as for the background grid during the Chimera approach. As the structured cells must be connected to the outer cells, a slightly higher total number of cells is obtained compared to the Chimera approach ($622\,168$ vs. $596\,992$). As shown in Figure 2.15, the difference between using and not using the Chimera approach is minimal, which verifies the approach to use overset grids as a means to achieve geometry variations quickly.

To show the influence of the turbulence model on the results, an additional simulation is performed with the $k-\omega$ turbulence model. From Figure 2.15 it is evident that the choice of turbulence model has an impact on the pressure coefficient distribution, especially at the shock location on the suction surface, where the location of the shock is moved upstream by $\Delta x/c = 0.009$. Köhler (2023) showed that the simulations performed with the $k-\omega$ turbulence model align slightly closer with the experimental data, although the difference between the two turbulence models is small. For the three-dimensional simulations, both turbulence models will be used and compared. However, as the Spalart-Allmaras model is computationally less expensive, it is used dominantly before a comparison with the $k-\omega$ model is performed.

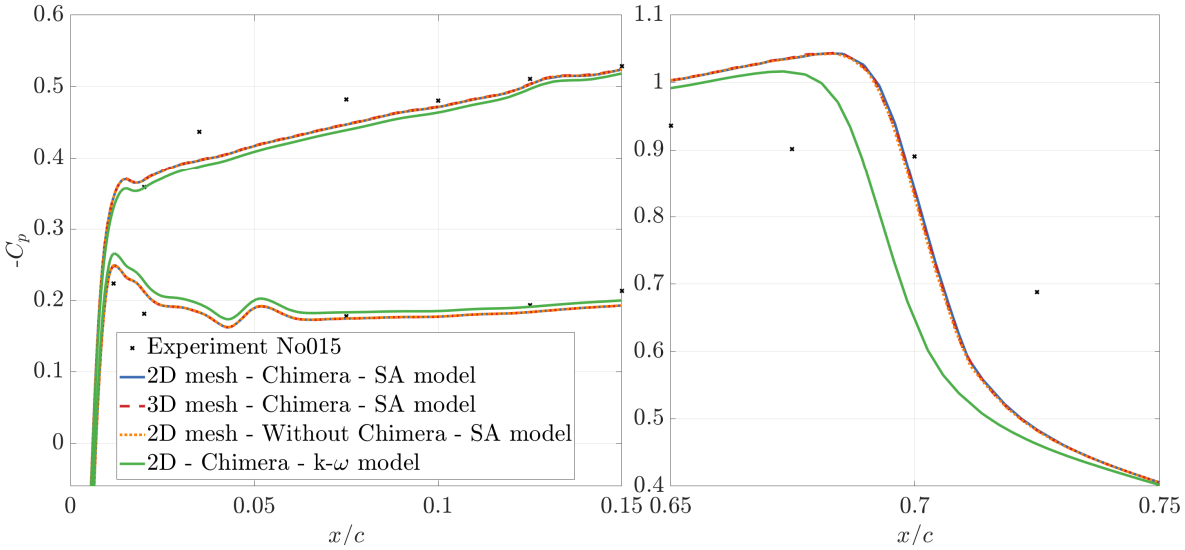

Figure 2.15: Pressure coefficient distributions for different numerical studies. The conditions of the simulations align with experiment No015. The two-dimensional mesh from the grid convergence study, shown in Figure 2.11 (blue), is compared with a corresponding three-dimensional mesh (red), a two-dimensional mesh without the Chimera approach (orange), and a simulation using an alternative turbulence model (green).

The validation and verification are performed for the parameters used in experiment No174. For validation purposes, Figure 2.16 shows close alignment of the experimental results and the numerical results. As mentioned for the simulations performed with the parameters of experiment No015, the differences can stem from experimental or numerical inaccuracies. A grid spatial and temporal convergence study is not performed separately for this case. Instead, the grid found for the grid convergence study of case No015 is used. As case No174 only features subsonic flow, case No015 was determined as the more critical case, and the convergence study was performed there. It is assumed that the grid convergence study holds for lower Mach numbers, and thus, case No174, too. As was the case for experiment No015, one verification step for the numerically obtained results is to compare them to the results obtained by a simulation based on the mesh by Köhler (2023). As mentioned earlier, the angle of attack for these simulations was corrected in this case by $\Delta\alpha = -0.1320°$.

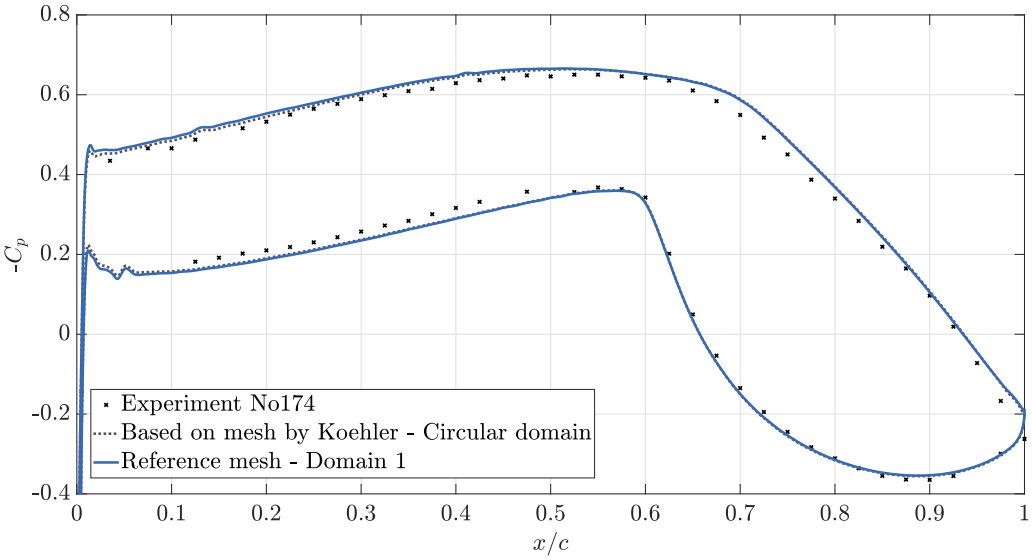

Figure 2.16: Pressure coefficient distributions for the two-dimensional spatial grid convergence study with the parameters of experiment No174, shown in Table 2.1. The simulations based on the mesh by Köhler (2023) are corrected for the angle of attack to match the perceived angle of attack of the airfoil in the test section of the tunnel.

2.3.4. Three-Dimensional Mesh Generation for Inviscid Walls

The same two-dimensional structured grid around the airfoil, as shown in Section 2.3.2, is used in the subsequent three-dimensional simulations. For all subsequent simulations and meshes, the three-dimensional simulations incorporate a sweep angle. A grid convergence study is now performed to determine the spacing in the Y-direction and the width of the cells of the background grid. The domain with extended horizontal walls, as introduced in Section 2.3.1, is used. In this way, the influence of the horizontal walls is eliminated, allowing for an isolated evaluation of the vertical wall's effect on the flowfield. Nevertheless, the placement of the horizontal walls at a considerable distance is a simplification, as the current setup in the KRG's test section does not allow for a three-dimensional adaptation, which would ideally result in the total elimination of the wall's influence on the flowfield.

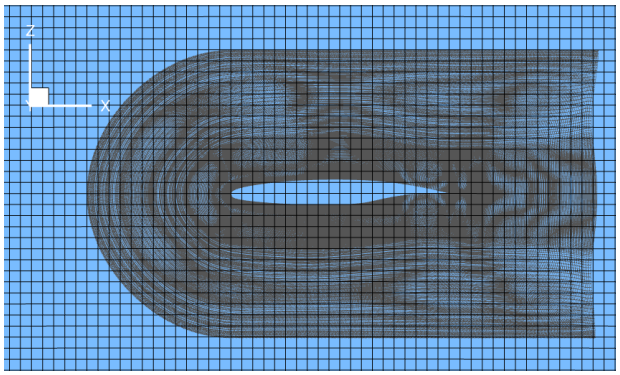

Figure 2.17: Unstructured background mesh (blue with black lines) and structured child mesh (grey dotted lines) shown with the airfoil in the X-Z-plane, i.e., in a longitudinal section view, for three-dimensional simulations with inviscid walls. The combination of both meshes is done with the Chimera method.

The domain consists of a background grid, created using BETA CAE Systems' ANSA[6], and the child grid Reference, created with MegaCads, as introduced in Section 2.3.2. The Chimera approach is used to combine the two grids, as shown in Figure 2.17. The background grids consist of equally spaced cells in the entire domain. As the wind tunnel walls are considered inviscid, no wall boundary layer needs to be captured, and therefore, a denser spacing at the tunnel walls is not required for this mesh. The number of cells for each background grid and wing grid is shown in Table 2.3 and Table 2.4, respectively.

Table 2.3: Number of cells for the computational grids of the background mesh for the grid convergence study of three-dimensional simulations with inviscid tunnel walls.

Computational Grid	Coarse	Reference	Fine
Number of cells	6 028 123	10 301 204	36 846 161
Corresponding max. cell size	10 mm	7.5 mm	5 mm
Max. cell size normalized to the tunnel width	0.0250	0.0188	0.0125

Table 2.4: Number of cells in spanwise direction for the computational grids of the child mesh for the grid convergence study of three-dimensional simulations with inviscid tunnel walls.

Computational Grid	Coarse	Reference	Fine
Number of cells in spanwise direction	60	80	100
Corresponding max. cell size	6.67 mm	5 mm	4 mm
Max. cell size normalized to the tunnel width	0.0167	0.0125	0.0100

[6]Accessed 27 May 2025. BETA (2025). *ANSA Pre Processor*. https://www.beta-cae.com/ansa.htm

The mesh generation is valid for all chord lengths, angles of attack, and sweep angles tested in this work. While a variation of these geometric conditions is applied, the background grid remains unchanged, and the child grid is adapted to fulfill the requirements. For a variation in chord length, the two-dimensional child grid is scaled by a factor in the X- and Z-directions. For a variation in angle of attack, the grid is rotated around the leading edge of the airfoil by the desired angle of attack. Finally, the sweep angle is introduced by the extrusion to a three-dimensional grid. To do so, the two-dimensional grid is extruded along a vector pointing along the direction that is to become the leading edge of the wing. Thus, the chord length and profile shape will remain defined in the tunnel X-direction and not perpendicular to the leading edge. The airfoil defining the chord length for all swept cases is the orange, stretched one in Figure 1.7. This streamwise-aligned section is chosen because the analysis of the pressure in the following will be done in streamwise-aligned planes. Nevertheless, it is essential to note that, from a construction point of view, a leading edge normal section is typically defined. The three-dimensional mesh generation is applicable to both unswept and swept cases. A three-dimensional view of the child grid is shown in Figure 2.18.

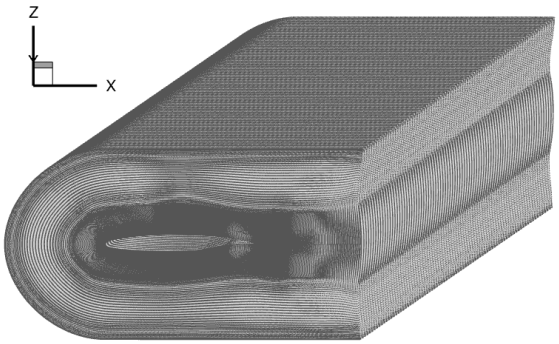

Figure 2.18: Structured child grid with an angle of attack of $\alpha = 0°$, a sweep angle of $\Lambda = 25°$, and a chord length of $c = 150$ mm. The mesh is extruded along a vector in the X-Y plane.

2.3.5. Three-Dimensional Simulations for Inviscid Walls

The verification of the results on the three-dimensional grids is performed with the grids introduced in Section 2.3.4. Euler, i.e., inviscid, horizontal, and vertical tunnel walls are used. The solver settings are given in Appendix A. The conditions under which the grid convergence studies are performed are close to those of experiment No174, but exhibit a sweep angle to introduce a more spanwise invariant flow. The chosen Mach number results in a subsonic flowfield, which is appropriate, as the results presented for these cases in Section 4.1 are for a subsonic flowfield. In the following document, the side walls are referred to as the inboard wall, which is the right wall in flow direction, and the outboard wall, which is the left wall in flow direction. The nomenclature ”inboard” and ”outboard” is used similarly to that of an aircraft, where the outboard section of the wing is positioned more downstream due to the wing sweep. Thus, in this thesis, the leading edge of the wing at the outboard wall is positioned downstream of that at the inboard tunnel wall.

Initially, a spatial grid convergence study is performed for the three-dimensional case with inviscid walls. Similarly to the two-dimensional cases, the spatial and temporal convergence is determined by comparing pressure coefficient distributions instead of an integral quantity, for which the reason is given in Section 2.3.3. As Figure 2.19 shows, the pressure coefficient distributions align closely, even when examining the curves closely. Thus, all three results are grid independent. Nevertheless, the reference grids are chosen over the coarser grids for the subsequent simulations. This is done to find a compromise between acceptable numerical cost and acceptable inaccuracies introduced by using the Chimera approach. As shown in Figure 2.17, the difference in cell sizes between the background and child grid is clearly noticeable. The effects of this difference on the solution are explained in Section 2.2.2. Thus, a moderate difference in cell sizes is chosen for the subsequent simulations, although a coarser background grid results in a grid-independent solution, as shown in Figure 2.19.

Compared to the infinitely swept wing condition, the pressure coefficient distribution aligns overall well, although it features some differences, especially in front of the pressure side and in the middle of the suction side of the wing. The differences will be closely examined in Section 4.1.

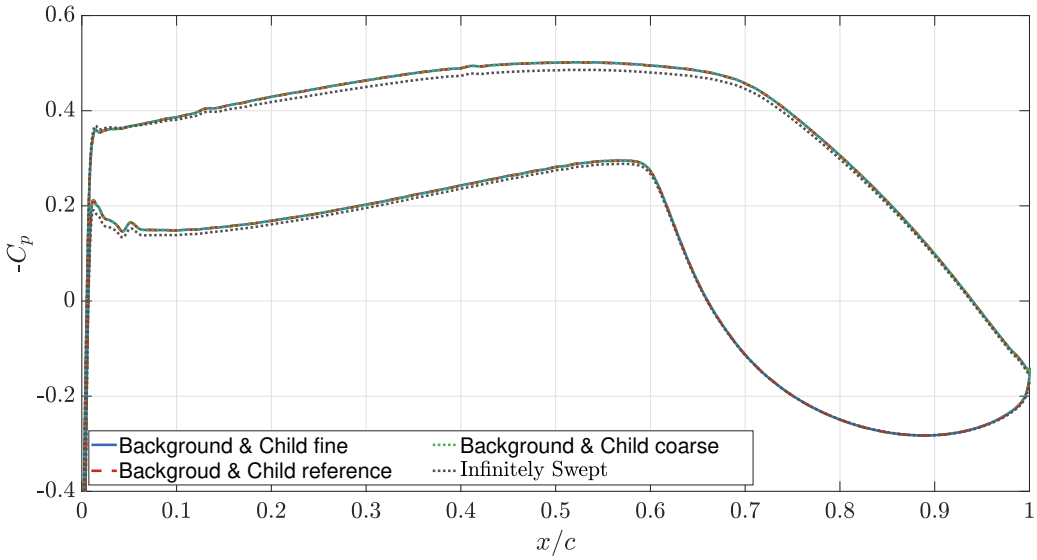

Figure 2.19: Pressure coefficient distributions for the spatial grid convergence study with inviscid tunnel walls. The pressure coefficient distributions are extracted at 50% of the tunnel width. The simulations are performed for $\alpha = 0°$, $\Lambda = 25°$, $c = 150\,\text{mm}$, $Ma = 0.65$, and $Re = 7 \times 10^6$.

For the same conditions, a temporal convergence study is performed. Following the temporal convergence study of the two-dimensional case in Section 2.3.3, the convergence is achieved for density residuals lower than 3×10^{-6}. To accelerate the convergence, the *pressure switch weighting factor* is reduced from 50 to 4 during the simulation. This factor is related to the matrix dissipation used for the three-dimensional simulations. Matrix dissipation is a numerical technique that incorporates artificial dissipation terms, thereby enhancing convergence and stability. The pressure switch is a component of the dissipation scheme that locally adjusts dissipation to reduce it where unnecessary and increase it where higher pressure gradients occur. Initially, the dissipation is increased to stabilize the solution, where, for a sufficiently low residual, the switch is reduced to prevent smoothing out physical gradients in the flowfield. Reducing this factor during the simulations temporarily increases the residual before the simulation converges further (DLR 2024).

2.3.6. Three-Dimensional Mesh Generation for Viscous Walls

For the viscous case, both computational domains introduced in Section 2.3.1 are used. First, the grid for the domain with extended horizontal walls is explained. Like in the case with inviscid tunnel walls, the background grid is created using BETA CAE Systems' ANSA. For the viscous case, the boundary layer evolving along the tunnel walls needs to be captured, especially in the region of the wall-wing junction. Therefore, the grid cells are spaced densely at the walls and expand towards the middle of the tunnel until they reach their maximum size. A so-called layer mesh captures the region close to the wall. The layers mesh consists of prism cells, which are indicated in Figure 2.20. The thickness of the boundary layer and, consequently, the corresponding thickness of the layer mesh are determined based on measurements from experiments conducted in the tunnel (Koch et al. 2008). The parameters used for the meshing of the background grid are shown in Table 2.5. The cell sizes of the volume grid in the middle of the tunnel are chosen corresponding to the case with Euler walls in Section 2.3.4. The layers mesh is constructed to achieve a y^+ at the wall of roughly one. The last cell height of the layers mesh is determined by the first cell height, the growth factor, and the number of layers, such that it matches the cell size of the volume cells. Thus, the number of layers decreases for the finer mesh, as the last cell height has to be smaller to match the size of the cells in the volume.

Table 2.5: Number of cells for the computational grids of the background mesh for the grid convergence study of three-dimensional simulations with viscous tunnel walls. The data for the volume mesh and the layers mesh are listed separately.

Computational Grid	Reference	Fine
	Volume Mesh	
Number of cells	21 841 405	51 463 619
Corresponding max. cell size	7.5 mm	5 mm
Max. cell size normalized to the tunnel width	0.0188	0.0125
	Layers Mesh	
First cell height	0.001 mm	0.001 mm
Growth factor	1.2	1.2
Number of layers	50	48

The corresponding wing mesh for the viscous study is created according to the procedure described in Section 2.3.4, and visualized in Figure 2.18. The grid spacing in the Y-direction of the tunnel is adapted, allowing for the appropriate capture of the boundary layer, especially in the region of the wall-wing junction. Therefore, the child grid features denser spaced cells close to the walls of the tunnel and less dense cells in the middle of the test section. The parameters for the grid convergence study are shown in Table 2.6.

Table 2.6: Number of cells in spanwise direction for the computational grids of the child mesh for the grid convergence study of three-dimensional simulations with viscous tunnel walls.

Computational Grid	Coarse	Reference	Fine
Number of cells	49 248 000	59 097 600	68 947 200
Number of cells in spanwise direction	250	300	350
Corresponding max. cell size	7.4 mm	7.4 mm	7.4 mm
Max. cell size normalized to the tunnel width	0.0185	0.0185	0.0185

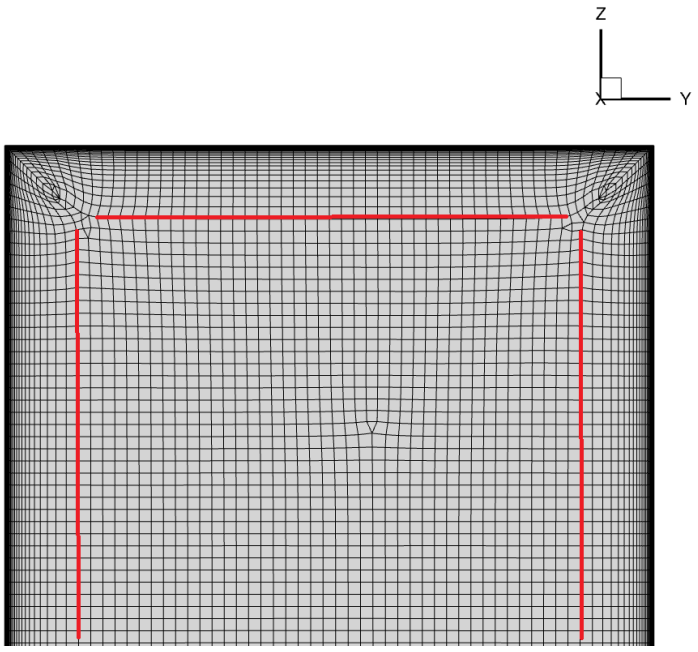

Figure 2.20: Mesh for the three-dimensional grid convergence study in the Y-Z plane, highlighting the layers mesh in red to capture the boundary layer.

The second domain shown in Figure 2.8b is also used for viscous simulations, where the same grids are used as for the first domain introduced above. This includes the child grid Reference, introduced in Table 2.6, and the layers mesh Reference, introduced in Table 2.5. This domain is used to study the combined effects of horizontal and vertical walls, which more closely represent the KRG's test section.

2.3.7. Three-Dimensional Simulations for Viscous Walls

The verification of the cases with viscous walls instead of Euler walls follows the same pattern as described in Section 2.3.5, just using viscous tunnel walls instead of inviscid ones. Thus, all cases shown in this section feature a sweep angle. The solver settings are given in Appendix A. The conditions under which the grid convergence study is performed are similar to those of experiment No015. However, a sweep angle is used to increase the spanwise inhomogeneity of the flowfield.

The results for the spatial grid convergence study are shown in Figure 2.21. The pressure coefficient distributions are extracted at 90% of the tunnel width, towards the outboard tunnel wall, and thus on the more downstream part of the wing. Instead of extracting the pressure coefficient at the middle of the test section, extracting it towards one of the walls ensures consistency in the grid convergence study for all locations in the tunnel. As viscous walls are employed, the gradients of the flowfield towards the walls are significantly higher than in the middle of the test section. Thus, comparing the pressure coefficient distributions of different meshes at the walls will ensure that actual grid-independent solutions are obtained. Overall, the pressure coefficient distributions align closely with each other. However, the coarsest mesh, consisting of the reference background grid and the coarse child grid, exhibits some differences from the other curves, particularly on the suction surface near the front of the wing, specifically for $0.1 < x/c < 0.4$. This indicates that the grid-independent solutions are obtained for the reference background grid paired with the reference child grid. The comparison to infinitely swept wing conditions is performed at a later stage in Chapter 3.

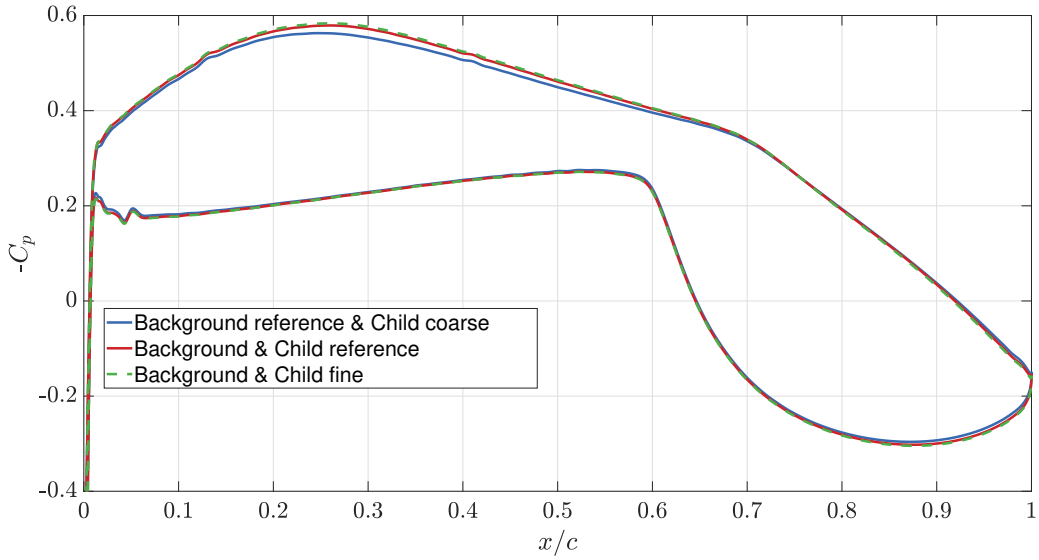

Figure 2.21: Pressure coefficient distributions for the grid convergence study with viscous tunnel walls. The pressure coefficient distribution is extracted at 90% of the tunnel width, i.e., close to the outboard wall. The simulations are performed for $\alpha = 0°$, $\Lambda = 25°$, $c = 150\,\text{mm}$, $Ma = 0.78$, and $Re = 7 \times 10^6$.

In addition to the spatial convergence study, the temporal convergence is evaluated. A residual lower than 5×10^{-6} will no longer increase the accuracy of the simulations, similar to the results of the two-dimensional case and three-dimensional case with inviscid walls.

2.4. Mesh Deformation

Changing the volume grid according to surface deflections can be achieved in two ways: the first would be a re-meshing of the entire domain, which can be very time-consuming. With the numerous parameter

combinations tested in this thesis, re-meshing would be improper. Instead, the TAU deformation tool is used to deform the volume grid. This method has downsides, primarily that only small perturbations can be handled to achieve a high-quality grid (DLR 2024). The working principle is explained below.

The algorithm was introduced by de Boer, van der Schoot, and Bijl (2007). It is developed for unstructured grids and is based on interpolating the displacements of boundary nodes to the entire mesh using radial basis functions (RBFs). Radial basis function interpolation is used to determine the displacement of internal nodes based on the displacement of structural nodes on the interface. The interpolation function $s(X)$ describes the displacement in the entire domain and is approximated by a sum of basis functions and a polynomial $p(X)$

$$s(X) = \sum_{j=1}^{n_b} \alpha_j \, \phi(\|X - X_{b_j}\|) + p(X), \tag{2.16}$$

where $X_{b_j} = [x_{b_j}, y_{b_j}, z_{b_j}]$ are the boundary nodes, n_b is the number of boundary nodes, p is a polynomial, and ϕ is a radial basis function. Interpolation conditions determine the coefficients α_j and the polynomial p. For a more detailed explanation, refer to de Boer, van der Schoot, and Bijl (2007). A thin plate spline is employed for $s(X)$ for the deformation in this thesis, which is considered both accurate and robust.

The deformation approach follows a scheme similar to one that is introduced by Birkemeyer (1999) and Romano et al. (2013). At first, quasi-two-dimensional simulations are performed. They are called quasi-two-dimensional because, although they feature a sweep angle, the mesh only exhibits one cell in the spanwise direction. The conditions are as if the wing were infinitely swept. From these infinitely swept wing conditions, certain streamlines are extracted. These streamlines are then used to determine the displacement of the nodes on the interfaces, i.e., the upper, lower, and side walls. The displacement is an input for the TAU deformation tool, which uses 2000 points per surface for the upper and lower wall and 5000 points per surface for the side walls to specify the displacement. The prisms of the wall boundary layer's mesh are displaced as a whole to ensure high-quality cells. The rest of the domain is displaced until a distance of roughly 40% of the tunnel width to ensure that the deformation of one wall has no influence on the deformation of the opposite wall.

The choice of streamlines for the horizontal walls is easier than that for the vertical walls. As the KRG's horizontal walls are only adaptive in two dimensions, one deformation is chosen for the upper and lower walls, respectively, and applied to all spanwise locations. This means that a streamline from the infinitely swept wing is extracted, which, at the X-location of the test section entry, is located at the same Z-location as the upper or lower wall of the test section. The perfect deformation for an unswept wing, considering inviscid tunnel walls, then follows this streamline.Figure 2.22 proves this concept by comparing pressure coefficient distributions of a simulation performed on Domain 1 with the horizontal walls placed far away from the unswept wing to the simulations performed on Domain 2 with deformed upper and lower walls. The minor differences in shock location can be attributed to the discrete input of deformation points. Although the input of the deformation tool utilizes 2000 points for deforming the upper and lower walls, and the resulting actual deformation is believed to be close to the specified input, the discrete specification results in an imperfect deformation that cannot precisely represent all gradients.

When including viscous instead of inviscid walls, the displacement thickness of the wall's boundary layer must be taken into account. For the simulations performed in this thesis, the displacement thickness of the upper and lower walls' boundary layer is extracted from the TAU solution for each simulation separately. The displacement thickness of the boundary layer is obtained from simulations with Domain 1 and then applied to cases with Domain 2. Theoretically, the displacement thickness will change for the new simulation, and its correct value must be determined through an iterative procedure. For simplicity, this is not performed in the presented work. Figure 2.23 shows a flow chart of the deformation procedure, with the red part indicating the missing iterative procedure.

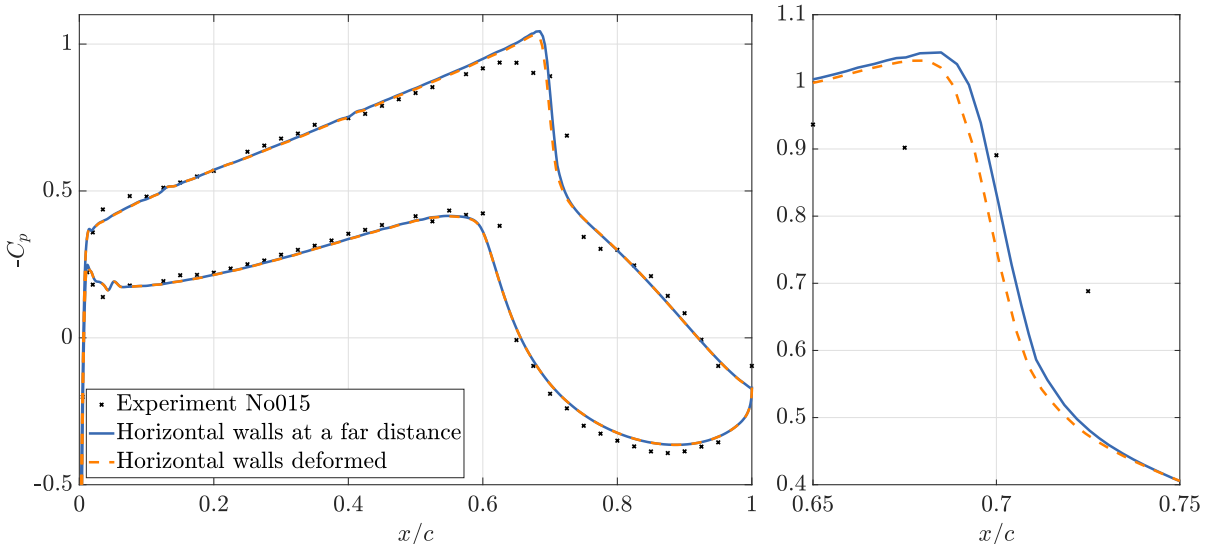

Figure 2.22: Pressure coefficient distributions over the normalized chord length of an unswept wing for a two-dimensional grid with the parameters of experiment No015 (Table 2.1). A comparison is made between the simulation with horizontal walls on Domain 1 and the deformed horizontal walls on Domain 2 to demonstrate that the deformation of the horizontal walls is working as intended.

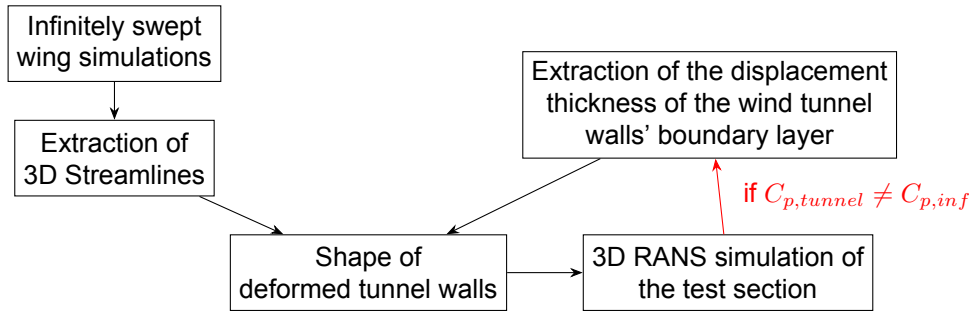

Figure 2.23: Flow chart of deformation procedure. The red loop indicates the iterative procedure that is missing from this thesis due to a reduction in complexity.

The deformation of the side walls follows the same procedure but is somewhat more complex. Currently, there is no possibility in the KRG to adapt the side walls; therefore, deformations are being explored as an approach to mitigate the impact of the side walls on the spanwise homogeneity of the flow. A possibility for testing with deformed walls would be to 3D print the shape of the walls and then apply it to the test section's walls in the KRG. Thus, the shape of the walls can be arbitrary, and, in contrast to the upper and lower walls, three-dimensional. When extracting the streamlines from the infinitely swept wing computations for different Z-locations above and below the wing, it is evident that the deformation of the streamlines is larger the closer the wing is approached. Especially in close vicinity to the wing, a discontinuity arises. This discontinuity arises because two particles traveling just over the suction and pressure surfaces will not meet at the trailing edge again, as the spanwise movement of the streamlines over the suction and pressure sides of the wing differs. Hence, specifying a three-dimensional deformation while taking the streamlines close to the airfoil into account leads to high gradients. Representing this deformation with the TAU deformation tool is impossible, as TAU uses continuous functions to determine the displacements. As a result, a simplification is necessary to obtain a valid deformation, specifically one that yields cells with positive volumes. Hence, a simplified deformation is specified, where not all streamlines are taken into account, which is explained below.

A fully three-dimensional deformation provides an accurate representation of the flowfield. Nevertheless, the deformation cannot be fully three-dimensional because the deformation tool is incapable of producing a valid mesh when large discontinuities arise in the flowfield. Instead, the streamlines are extracted from the infinitely swept wing simulations at Z-locations from the top to the bottom of the domain in steps of 0.05 m for 2 m > Z > 0.1 m and -0.1 m > Z > -2 m, whereas the spacing is decreased to 0.005 m for 0.1 m > Z > 0.06 m and -0.06 m > Z > -0.1 m. Hence, the streamlines extracted closest to the wing are located at $Z = \pm 0.06$ m, which corresponds to a distance of roughly $1/3c$ above or below the wing's surface. This value is chosen because the movement of a particle along a streamline is small enough to yield a deformed mesh with only positive volume cells. Figure 2.24 shows a comparison of the shape of different streamlines. The previously mentioned streamline at $Z = 0.06$ m is shown in dark blue, and the streamline at $Z = 0.15$ m is shown in light blue. The comparison highlights the larger gradients close to the airfoil. This figure illustrates the shape of the streamlines in two dimensions, giving the impression that the streamline at $Z = 0.06$ m is not continuous, which is not the case. Additionally to the shape of the streamlines extracted from the infinitely swept wing simulations, i.e., the specified deformation, the actual shape of the inboard wall after the deformation is shown in red for the location $Z = 0.06$ m and in orange for the location $Z = 0.15$ m. The location of the leading and trailing edges of the wing is indicated with two vertical lines. Although the overall alignment between the specified and actual deformation is large, the strong gradients cannot be represented accurately.
The shape of the streamlines at the locations $Z = \pm 0.06$ m is then used for the deformation closer to the airfoil, until a Z-location of $Z = \pm 0.01$ m, which roughly represents the location of the highest thickness of the wing. With this procedure, it is possible to reduce the gradient of deformations near the airfoil; however, it introduces inaccuracies. It is essential to note that the region between the positive and negative Z-values $0.01 > Z > -0.01$ will be adjusted by the deformation tool, as no deformation is specified in this region.

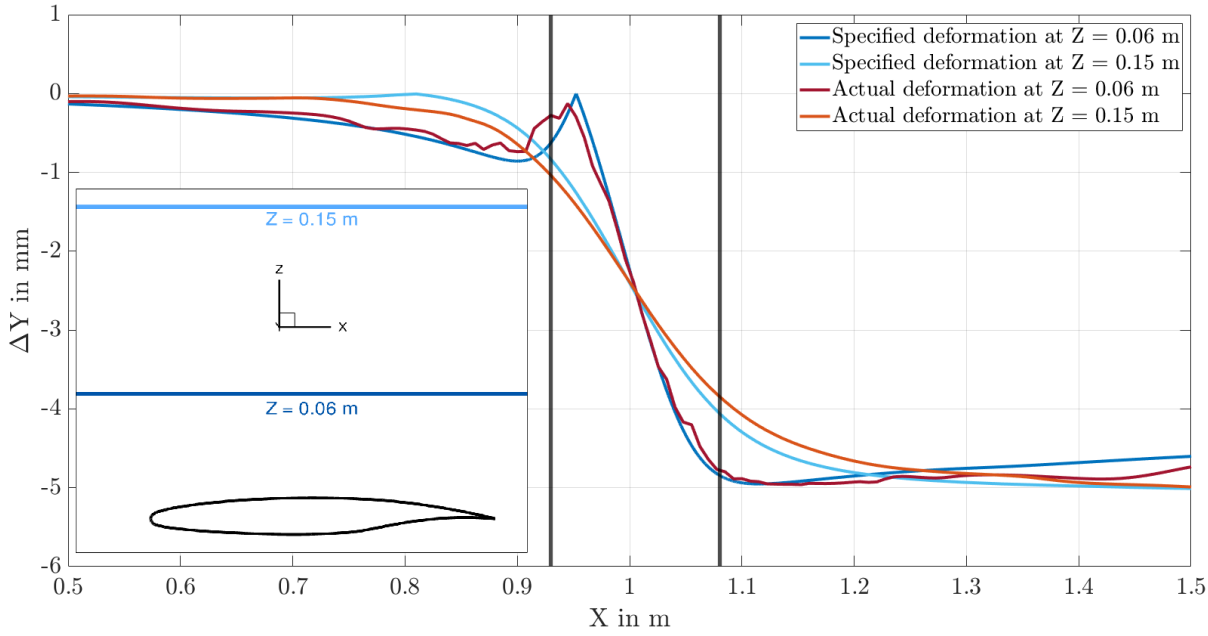

Figure 2.24: Shape of two streamlines extracted from the infinitely swept wing simulations, shown in blue, compared to the actual shape of the deformed inboard wall for the inviscid wall shown in red and orange. The location of the wing is indicated by two vertical lines, representing the location of the leading and trailing edges. A sketch of the location of the extracted streamlines is shown in the bottom left.

Figure 2.25 shows the shape of the deformed inviscid side walls. The two black lines indicate the location of the leading and trailing edges. It can be observed that, for the inviscid case, the shape of the deformation for both walls is identical, simply shifted in the X-direction to account for the different locations of the leading edges at the inboard and outboard walls. Using the same deformation for both side walls is a simplification, as the upstream part of the wing will influence the downstream part and vice versa. Consequently, the shape of the deformation should be different to account for this non-uniform blockage.

As explained above, an iterative procedure, which would be required to account for the non-uniform blockage in this case, is not performed in this thesis due to time constraints.

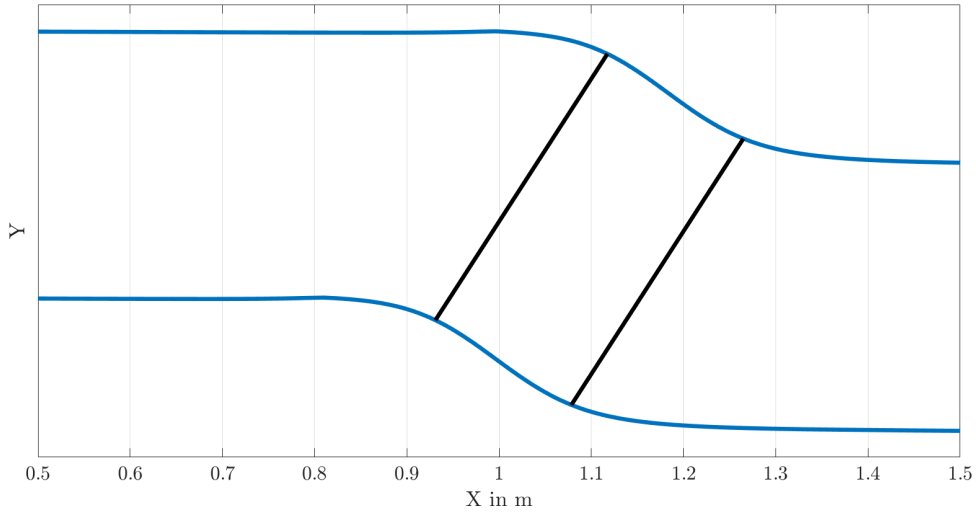

Figure 2.25: Exemplary shape of the inboard and outboard deformed side wall for the inviscid case. The black lines indicate the locations of the leading and trailing edges between the walls.

Similarly to the upper and lower walls, the displacement thickness of the wall's boundary layer must be taken into account for the deformation of the side walls when viscosity is introduced at the walls. The boundary layer developing close to the airfoil features large variations in thickness, as a favorable pressure gradient leads to an increase in local velocity near the wall. The increased momentum transport toward the wall reduces the thickness of the boundary layer. In contrast, when the flow encounters an adverse pressure gradient, the boundary layer tends to thicken. This effect results in large gradients in the deformation, which cannot be accurately represented without resulting in cells with negative volumes, as described above. To avoid this, an exemplary displacement thickness is extracted at a Z-location of $Z = 1\,\mathrm{m}$ and applied to all Z-locations, i.e., the deformation due to the displacement thickness of the boundary layer is assumed to be two-dimensional. It is essential to note that this procedure is a limitation of the method used in this work; however, it can be adapted when 3D printing liners for an experiment.

Other effects related to employing deformed side walls, such as reducing the separation at the walls, are illustrated in the simulations with viscous tunnel walls, as shown in Section 4.2.

3

Results with Undeformed Side Walls

The KRG's test section, as described in Section 2.1.2, is capable of adapting the horizontal walls to eliminate their influence on the flowfield. The vertical walls, however, can not be adapted. This leads to a significant influence of the vertical walls on the flowfield in the test section, especially for swept wing experiments, which cannot be easily accounted for by the correction methods introduced in Section 1.4.2. Unless stated otherwise, the simulations are performed with the same parameter settings as those used in the grid convergence study introduced in Section 2.3.7. Specifically, viscous walls are modeled as the walls of the test section and the surface of the airfoil. A reservoir-pressure inflow and an exit-pressure outflow are employed. A central scheme is used as the discretization method for the convective fluxes of the RANS equations, and the Spalart-Allmaras turbulence model is utilized. A comparison of turbulence models will be shown for deformed vertical walls in Section 4.2.1. A fully turbulent boundary layer is assumed on the surfaces. The solver settings are shown in Appendix A.

A motivation of the test conditions is given by Köhler (2023), who studied the effect of the angle of attack, the sweep angle, the chord length, the Mach number, and the Reynolds number on the flowfield of an infinitely swept wing. A summary of the parameters studied during this thesis is given in Table 3.1, where not all combinations of parameters are actually shown in this document.
Following Köhler (2023), the analysis is limited to angles of attack that are representative of free-flight conditions. As the angle of attack is increased, the velocity perpendicular to the leading edge is increased on the suction side of the wing and reduced on the pressure side. The velocity component parallel to the leading edge remains constant. Hence, a larger angle of attack yields opposite effects for the two sides of the wing. For angles of attack higher than $\alpha = 2°$ and the studied Mach number of $Ma = 0.65$, a shock forms close to the leading edge on the suction surface of the wing. As the shock prevents an isolated study of the influence of the angle of attack on the flowfield, the subsequent analysis is limited to $\alpha = 2°$. The sweep angle is the main driver of spanwise inhomogeneities. As Köhler (2023) showed, the spanwise movement of inviscid streamlines is increased significantly when increasing the sweep angle. Nevertheless, the goal is to study the effects on swept wings in the KRG, which necessitates a certain sweep angle. Consequently, sweep angles of $\Lambda = 5°$ to $\Lambda = 25°$ are chosen. A higher chord length results in a higher spanwise displacement of the flow over the wing. This is to be expected because the pressure gradient acting on the velocity component perpendicular to the leading and trailing edges acts on the flow for a larger distance. Thus, in addition to the baseline length of $c = 150\,\text{mm}$, two smaller chord lengths are studied to examine the possibility of reducing the potential influence of the walls on the flowfield. To study subsonic and transonic flows, two different Mach numbers are chosen by Köhler (2023). As the sweep angles studied in this thesis are moderate, a Mach number of $Ma = 0.65$ is chosen for the cases without shocks in the flowfield. To represent transonic conditions, the Mach number is increased to $Ma = 0.78$. Increasing the Mach number even further results in shock-induced flow separation, which negatively influences the flowfield and makes a thorough analysis of the flowfield difficult. As the Reynolds number has a direct influence on the displacement by the boundary layer, it is to be expected that a change in Reynolds number influences the pressure distribution along the wing. However, for high Reynolds numbers, an asymptotic behavior is to be expected (Schlichting and Gersten 2006), which Köhler (2023) showed for his analysis. Hence, it is possible to limit the subsequent analysis to a single Reynolds number, thereby reducing the number of parameter combinations.

The baseline case for the simulations shown in the previous sections and chapter is for $\alpha = 0°$, $\Lambda = 15°$, $c = 150\,\text{mm}$, $Ma = 0.65$, and $Re = 7 \times 10^6$, as these conditions are close to the conditions used during the experiment, the sweep angle is moderate, and the Mach number results in a subsonic flowfield, which makes an assessment without shocks possible.

Table 3.1: Parameters that are studied in the following chapters based on a pre-selection by Köhler (2023).

Angle of attack	$0°$	$2°$	
Sweep angle	$5°$	$15°$	$25°$
Chord length	$50\,\text{mm}$	$100\,\text{mm}$	$150\,\text{mm}$
Mach number	0.65	0.78	
Reynolds number	7×10^6		

3.1. Results without Horizontal Walls

As the general influence of the tunnel walls on the flowfield inside the test section is unknown, it is essential to distinguish between the effects caused by the horizontal and side walls. This section presents results from simulations conducted on Domain 1, as illustrated in Figure 2.8a. This domain differs from the test section's geometry only in the Z-direction, and, instead of placing the horizontal walls at their true location, they are placed at a considerable distance of roughly 13 times the chord length. This way, the isolated effects of the side walls can be studied without considering the effect of the upper and lower tunnel walls. Although this is not representative of the actual test section geometry, the knowledge acquired from the results will greatly influence the choice of parameters. In Section 3.2, simulations based on Domain 2 will be performed to couple the effect of horizontal and side walls on the flow.

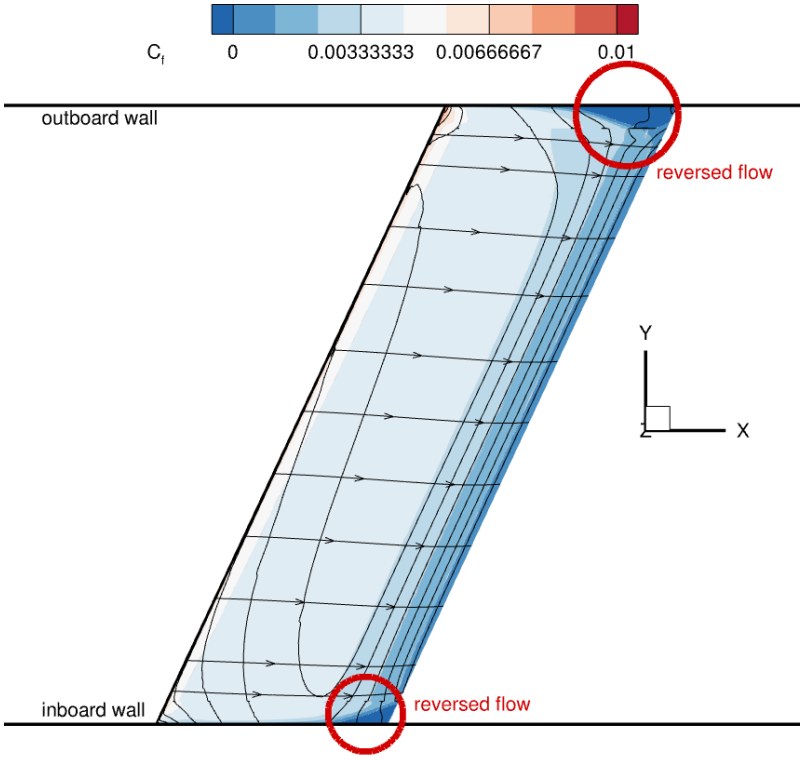

Figure 3.1: Inviscid streamlines for different spanwise locations on the suction surface of the wing, shown in the X-Y-plane. The color map indicates the friction coefficient, with the region of flow reversal highlighted in red. The dark lines indicate regions of constant pressure. The simulations are performed for $\alpha = 0°$, $\Lambda = 25°$, $c = 150\,\text{mm}$, $Ma = 0.65$, and $Re = 7 \times 10^6$.

Figure 3.1 shows the setup for a simulation with $\alpha = 0°$, $\Lambda = 25°$, $c = 150\,\text{mm}$, $Ma = 0.65$, and $Re = 7 \times 10^6$. This case is chosen with a large sweep angle, together with the smaller Mach number, to show the effect of the spanwise inhomogeneity and to isolate the effects from the occurrence of shocks. The colormap indicates the friction coefficient on the suction side of the wing between the two tunnel walls. The lines indicate constant pressure. The streamlines at the boundary-layer edge are visualized for different spanwise locations. Regions of flow reversal can be identified for friction coefficients less than zero and are indicated by a red circle. It is evident that the streamlines exhibit significant curvature around the region of reversed flow, thereby altering the flowfield. This ultimately leads to a deviation of the streamlines at the boundary-layer edge from their original shape and from the shape of the streamlines in the middle of the tunnel. This indicates that the flowfield varies across the tunnel width, making measurements sensitive to the measurement location. Moreover, it means that the flowfield at the walls will influence the flowfield in the entire test section. Comparing different simulations, it can be found that the higher the angle of attack, sweep angle, chord length, and Mach number, the larger the region of reversed flow at the outboard tunnel wall. Generally speaking, achieving a large region with similar flow conditions in the spanwise direction is easier to achieve with less flow reversal. The choice of turbulence model will greatly affect the results for the recirculation region. Thus, a comparison between the SA and the $k - \omega$ model will be performed in Section 4.2.1. The further analysis in this thesis examines the differences in the flowfield at various spanwise planes compared to each other and to the infinitely swept wing case. The flowfield with introduced countermeasures, such as deformed side walls, can then be compared to determine the possibility of achieving conditions similar to those of the infinitely swept wing case over a wide span in the tunnel. Additionally, it can be observed that the pressure coefficient for the suction surface of the wing aligns closely with the theoretical distribution that was introduced in Figure 1.10. The isobar pattern is shifted aft for the part of the wing that lies close to the inboard wall, and is moved forward for the part that is close to the outboard wall. The reasons for this behavior are explained in Section 1.3.4.

After this general introduction to the flowfield of the simulations with viscous tunnel walls and undeformed side walls, a closer examination of the effects of angle of attack, sweep angle, chord length, and Mach number is performed in the following sections.

3.1.1. Influence of the Angle of Attack

This section discusses the effects of a change in angle of attack on the flowfield inside the KRG's test section. First, the pressure coefficient distributions for $\alpha = 0°$ are shown in Figure 3.2, which, compared to the previous figure, features a lower sweep angle to show the effect of the angle of attack more pronounced. The freestream and geometric conditions are indicated in the figure caption. Analog to the spanwise planes shown in Figure 3.1, the pressure coefficient is extracted at different spanwise locations in the tunnel, where the values refer to the percentage in the tunnel, with zero percent starting at the inboard wall. Generally, the curves exhibit a similar shape of the isobars that are explained in literature, as explained in Section 1.3.4 and shown in Figure 3.1. The isobars curve forward on the side of the wing more downstream and curve backward at the side of the more upstream part. This manifests in Figure 3.2 by a larger suction peak near the leading edge for the more downstream parts of the wing, i.e., for the higher percentage values of spanwise location. Similarly, the pressure will drop more rapidly towards the trailing edge in these cases, i.e., featuring only small parts of the chord with a favorable pressure gradient. The reason for this behavior is that the flow at the walls does not move in the spanwise direction, which dictates the shape of the isobars, causing them to penetrate the wall perpendicular to it. At the planes closer to the inboard wall, the pressure coefficient peak at the front will be lower, whereas the pressure coefficient will increase faster towards the aft of the chord.

Compared to infinitely swept wing conditions, the pressure coefficient distributions vary significantly. This effect is clearly visible for the two planes closest to the wall. Both pressure distributions on the suction surface of the wing differ significantly from those in the infinitely swept wing case in terms of value and shape. For the pressure side of the wing, this difference is smaller than for the suction side. However, both curves deflect from the infinitely swept wing case and themselves significantly towards the middle and the aft part of the chord.

To quantify the difference in pressure coefficient distributions between the infinitely swept wing case and the other cases, the root mean square error (RMSE) is employed. It is calculated by

$$\text{RMSE} = \sqrt{\frac{1}{N}\sum_{i=1}^{N}\left(C_{p_i} - \hat{C}_{p_i}\right)^2}, \tag{3.1}$$

where C_{p_i} is the reference value, $\hat{C}_{p_i}$ the measured value, and N the number of values compared. The percentage value of the RMSE is then calculated by dividing the RMSE by the maximum absolute value of the reference value and multiplying by 100. For the discussed plot, the results for the RMSE comparing a spanwise plane in the tunnel to the infinitely swept wing conditions are shown in Table 3.2.

The curves between 30 percent and 70 percent of the tunnel feature closer alignment with themselves and the infinitely swept case in terms of shape and value. The difference in the pressure surface is slight. For the suction surface, the difference indicates that the isobars over these parts of the wing follow the wing parallel to the leading edge much closer than is the case close to the test section's walls. In terms of the RMSE, the difference between the 30 percent and 70 percent planes is 4.17% for the suction surface and 2.47% for the pressure surface. For comparison, the RMSE between the 10 percent and 30 percent planes is 4.31% for the suction and 2.63% for the pressure surface. That shows that, if experiments are conducted in the KRG without further adaptations, the measurements should be performed only in the middle of the test section to avoid flow conditions not aligning with the rest of the flowfield when approaching the tunnel walls, as the RMSE between the middle 40 percent tunnel width is smaller than the RMSE of 20 percent tunnel width towards the walls. As a remark, it should be noted that a small RMSE between the 30 and 70 percent planes only indicates a large symmetry and not necessarily a large spanwise homogeneity. Nevertheless, the behavior of the pressure in this case allows using the RMSE between two planes not only for assessing symmetry, but also to assess homogeneity. Nevertheless, it remains doubtful that the middle 40 percent of the tunnel width lies close enough to each other and under the infinitely swept wing conditions to facilitate experiments that yield data approximately representing infinitely swept conditions over a significant width of the test section.

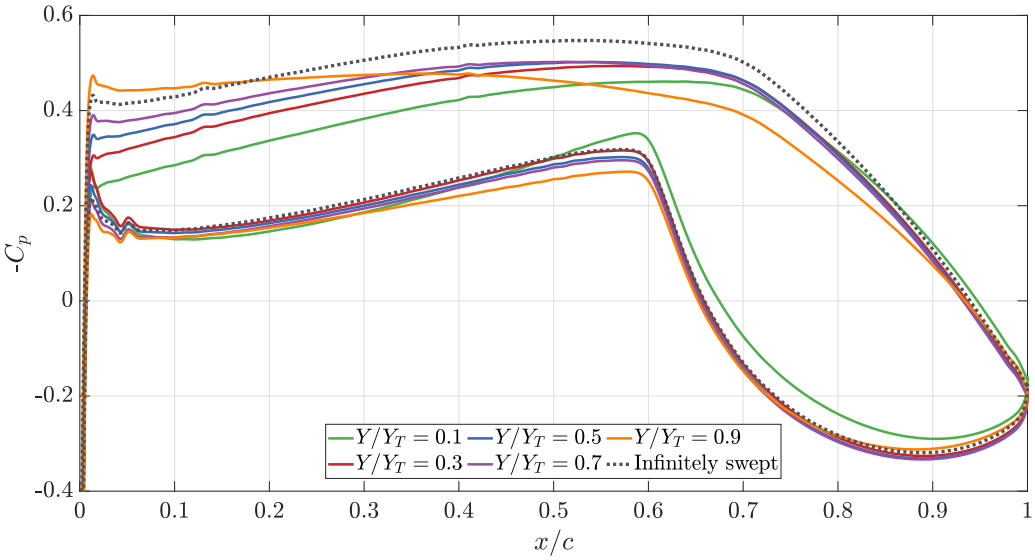

Figure 3.2: Pressure coefficient distributions for different spanwise locations compared to the infinitely swept wing condition. The simulations are performed for $\alpha = 0°$, $\Lambda = 15°$, $c = 150\,\text{mm}$, $Ma = 0.65$, and $Re = 7 \times 10^6$.

The behavior of the pressure coefficient curves and the RMSE indicates that the flowfield towards the walls differs significantly from the infinitely swept wing conditions and features strong spanwise gradients, i.e., a substantial variation of the flowfield in the spanwise direction. However, the curves in the middle of the tunnel feature similarity with each other and with the infinitely swept wing case. This suggests that improving the testing conditions, for example, by introducing deformed side walls, can yield a significant

improvement in the spanwise homogeneity of the flowfield and align the pressure coefficient with infinitely swept wing conditions more closely.

Table 3.2: Root mean square error of the pressure coefficient distributions at a certain spanwise plane compared to the infinitely swept wing case. The simulations are performed for $\alpha = 0°$, $\Lambda = 15°$, $c = 150\,\text{mm}$, $Ma = 0.65$, and $Re = 7 \times 10^6$.

Tunnel Width	10%	30%	50%	70%	90%
RMSE suction side	11.77%	7.33%	5.16%	3.70%	6.05%
RMSE pressure side	3.45%	2.12%	1.43%	1.46%	2.48%

To compare the conditions of infinite swept wing simulations with those in the tunnel, studying the boundary-layer edge velocity in the body-fixed spanwise direction is of interest. Figure 3.3 shows that the boundary-layer edge velocity in spanwise direction, v_z, is constant over the chord length for the infinitely swept wing case, which is explained in Section 1.3. Thus, the more constant v_z for the different spanwise planes in the tunnel, the more homogeneous the flow conditions across the wing. The results are non-dimensionalized with respect to the infinitely swept condition to make differences between the various cases independent of the absolute value of spanwise velocity. It can be found that at both planes closest to the walls, the variation in spanwise boundary-layer edge velocity is significant. In alignment with what is presented in Figure 3.2, the planes close to the wall are not representative of infinitely swept conditions, as the deviation from the infinitely swept case is significant. The planes, approaching the middle of the tunnel, approach the constant velocity closely. However, the absolute maximum and minimum spanwise velocities of one section still differ by 5.70%, 3.30%, and 3.19% for the 30 percent, 50 percent, and 70 percent planes, respectively. Generally speaking, an increase in spanwise velocity can be noted in the forward parts of the wing for all spanwise locations. This is attributed to the shape of the isobars shown in Figure 3.1, which are not aligned with the leading edge, but rather curved. The velocity component perpendicular to the leading edge is thus not only accelerated perpendicular to the leading edge, but also parallel to it, in contrast to an infinitely swept wing, where the isobars are aligned with the leading edge. The large deviation from the infinitely swept conditions near the walls is caused by the complex flowfield. While the reversed flow region at the trailing edge of the inboard wall causes the flow to increase its spanwise velocity, the reversed flow region at the outboard wall causes the spanwise velocity to decrease.

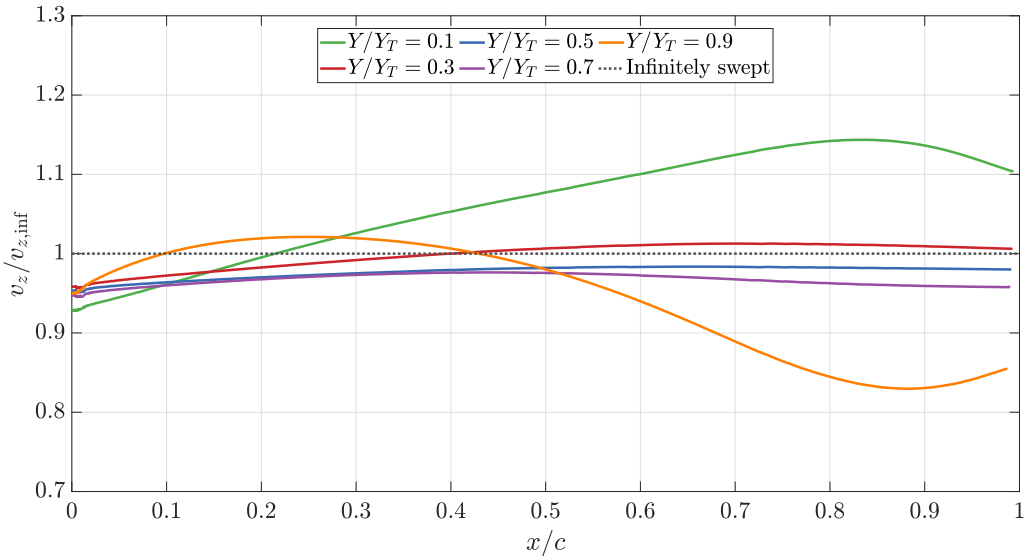

Figure 3.3: Boundary-layer edge velocity on the suction side of the wing in body-fixed spanwise direction for different spanwise locations compared to the infinitely swept wing condition. The simulations are performed for $\alpha = 0°$, $\Lambda = 15°$, $c = 150\,\text{mm}$, $Ma = 0.65$, and $Re = 7 \times 10^6$.

Similar effects to what was found for the angle of attack of zero can be observed for the case with $\alpha = 2°$, whose spanwise velocities at the boundary-layer edge non-dimensionalized with the spanwise velocity of the infinite swept case are shown in Figure 3.4. While the velocity for the infinitely swept wing case is the same as for the previous case with $\alpha = 0°$, the oscillations of the spanwise velocities in the tunnel are higher. Again, for the planes close to the walls, the difference to the infinitely swept case is so substantial that the flow conditions are significantly different from the infinitely swept wing case. For the planes towards the middle of the tunnel, the difference between the absolute maximum and minimum velocities of one section is larger than for the smaller angle of attack. Specifically, the percentages are 8.55%, 4.83%, and 4.29% for the 30 percent, 50 percent, and 70 percent planes, respectively. The same flow conditions dictate the general shape as for the previous case.

The comparison of both cases shows that reducing the angle of attack yields flow conditions that lie closer to each other and the infinitely swept wing conditions. It is deemed more realistic to achieve flow conditions that allow for experiments at a smaller angle of attack. Thus, no further investigation is performed in the case with $\alpha = 2°$. However, it must be noted that for being able to conduct experiments in the tunnel, even in the presented case with $\alpha = 0°$, it is advised to incorporate measures to improve the homogeneity of the flow conditions.

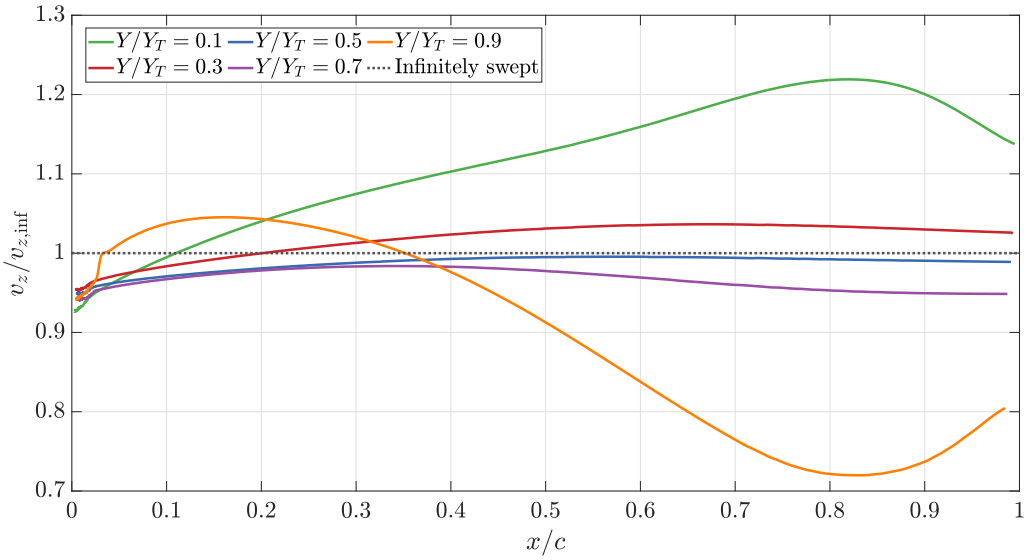

Figure 3.4: Boundary-layer edge velocity on the suction side of the wing in body-fixed spanwise direction for different spanwise locations compared to the infinitely swept wing condition. The simulations are performed for $\alpha = 2°$, $\Lambda = 15°$, $c = 150\,\mathrm{mm}$, $Ma = 0.65$, and $Re = 7 \times 10^6$.

3.1.2. Influence of the Sweep Angle

Figure 3.5 shows the spanwise velocity at the boundary layer edge in the body-fixed coordinate system for three different sweep angles and the suction surface of the wing, non-dimensionalized with the infinite swept condition. The case for a sweep angle of $\Lambda = 15°$ is already shown in the section above. Hence, to isolate the effect of sweep on the results, this case is compared alongside a higher sweep angle of $\Lambda = 25°$ and a lower sweep angle of $\Lambda = 5°$. The velocities are extracted in the midplane of the tunnel (50 percent) and at a plane near the outboard wall (90 percent). As already shown in the previous section, the oscillation in cases close to the wall indicates that the flow conditions are not suitable for representing flow over an infinite swept wing, which is caused by the complex three-dimensional effects introduced by the walls. The maximum relative difference between the velocity in the infinitely swept case and the velocity at the 90 percent plane is over 100% for the smallest sweep angle. For the midplane of the tunnel, the difference from the infinitely swept conditions is reduced. The rates for the absolute value of velocities are 1.75% for the largest sweep angle, 1.65% for the middle, and 1.32% for the smallest sweep angle. This indicates that a smaller sweep angle yields results closer to those of infinite swept wing conditions for the middle of the test section. As already shown in Figure 3.3, which presents experiments under the same conditions as the results for $\Lambda = 15°$ in this section, the spanwise velocity in the tunnel midplane is far

from constant along the chord. This makes a representation of infinite swept wing conditions improper with the current setup of the test section, which was already found in the previous section on simulations with $\Lambda = 15°$. Surprisingly, the non-dimensionalized deviation of the spanwise velocities at the 90 percent plane is highest for the lowest sweep angle. This can be explained with Figure 3.6, where the friction coefficient for the suction side of the simulation for $\Lambda = 5°$ and $\Lambda = 25°$ is shown. Red regions indicate a friction coefficient greater than zero, while blue regions indicate a friction coefficient of zero or less. Although the sweep angle in Figure 3.6b is significantly larger, the region of reversed flow does not scale by the same amount. Without the non-dimensionalization, the difference in spanwise velocity at the 90 percent plane to infinite swept conditions for the three sweep angles is roughly the same. Since the infinite swept spanwise velocity is highest in the case with the highest sweep angle, the non-dimensionalization yields this drastic difference. Nevertheless, this analysis demonstrates that it is crucial to avoid regions close to the walls when measuring, as the results differ significantly from those obtained under infinite swept conditions, mainly caused by the recirculation at the walls.

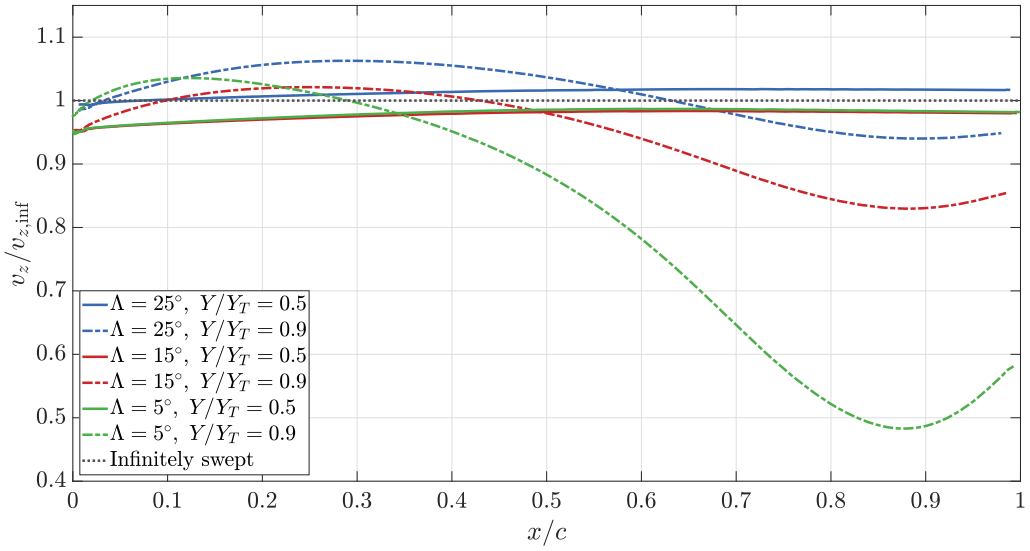

Figure 3.5: Boundary layer edge velocity in body-fixed spanwise direction for different sweep angles on the suction side of the wing. Two different locations within the tunnel width are compared to the infinitely swept wing conditions. The simulations are performed for $\alpha = 0°$, $c = 150\,\mathrm{mm}$, $Ma = 0.65$, and $Re = 7 \times 10^6$.

Figure 3.7 shows the spanwise velocity component at the boundary-layer edge for the pressure side of the wing. As shown above, the non-dimensional difference to the infinite swept conditions is most significant for the smallest sweep angle. Surprisingly, even in the middle of the test section, the spanwise velocity aligns closest with the infinite swept conditions for the highest sweep angle. This is contrary to what is shown for the suction side in Figure 3.5. Nevertheless, the pressure distribution shown in Figure 3.6 indicates that the conditions for the smaller angle of attack of $\Lambda = 5°$ align closer to infinite swept conditions, where the isobars are parallel to the leading edge, than for the case with a sweep angle of $\Lambda = 25°$.

In conclusion, even for smaller sweep angles, the difference from infinite swept conditions is significant. Especially toward the walls, the flowfield differs significantly due to the flow separation towards the trailing edge. It remains uncertain whether the measures to improve flow homogeneity, such as deformed vertical walls, can reduce the size of recirculating flow at the walls. Even in the midst of the test section, conducting experiments in the KRG without adapting the setup will most likely not yield flow conditions that align with those of an infinite swept wing. Reducing the sweep angle seems to have a beneficial effect on the homogeneity of the pressure distribution, but not on the spanwise velocity. It is recommended to incorporate measures that reduce the influence of the vertical walls on the flowfield and to evaluate these measures for various sweep angles.

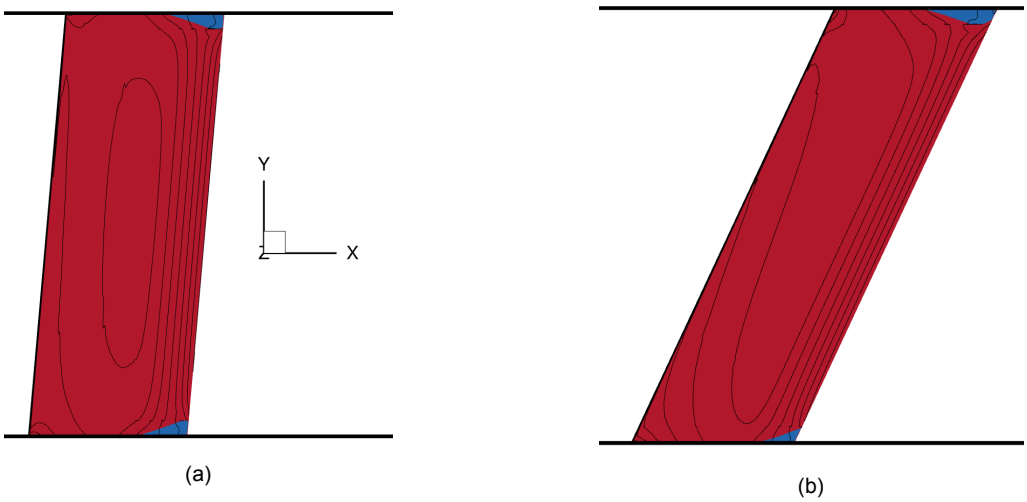

Figure 3.6: Friction coefficient for the suction side of two wings, regions with friction coefficients smaller than or equal to 0 are marked blue, friction coefficients larger than 0 are marked red. The black lines indicate lines of constant pressure. The simulations are performed for $\alpha = 0°$, $c = 150\,\text{mm}$, $Ma = 0.65$, and $Re = 7 \times 10^6$. (a) For $\Lambda = 5°$. (b) For $\Lambda = 25°$.

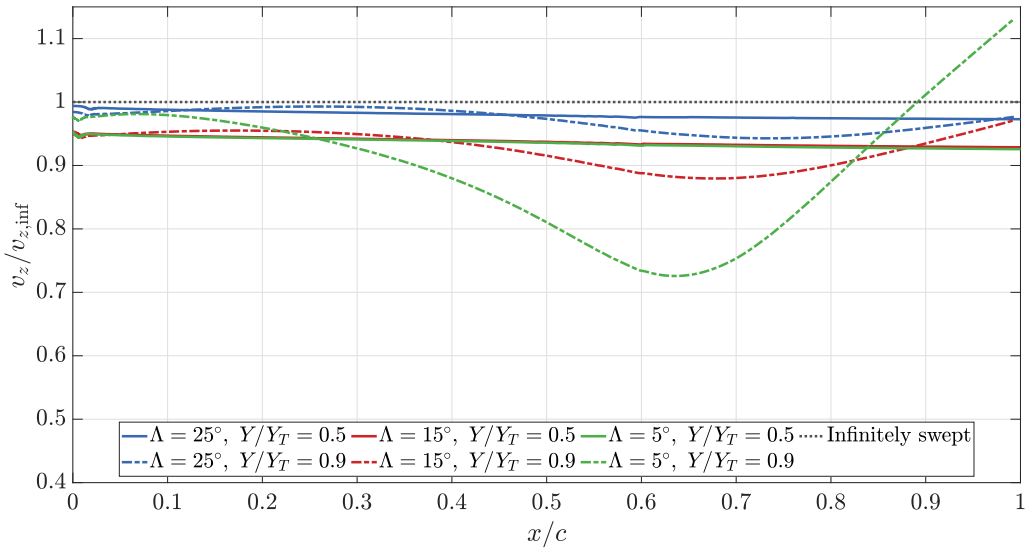

Figure 3.7: Boundary layer edge velocity in body-fixed spanwise direction for different sweep angles on the pressure side of the wing. Two different locations within the tunnel width are compared to the infinitely swept wing conditions. The simulations are performed for $\alpha = 0°$, $c = 150\,\text{mm}$, $Ma = 0.65$, and $Re = 7 \times 10^6$.

3.1.3. Influence of the Chord Length

This section examines the impact of varying chord lengths on the flow field in the tunnel. The case for $c = 150\,\text{mm}$ was already shown in the previous sections. To show the isolated effect of a change in chord length, results acquired under the same conditions as in the previous sections but with different chord lengths of $c = 100\,\text{mm}$ and $c = 50\,\text{mm}$ are presented. As observed for the change in angle of attack and sweep angle, the differences between the infinite swept wing cases and the simulations in the tunnel are significant. This only changes marginally for a variation in chord length, as shown in Figure 3.8. For this plot, only the tunnel midplane is shown. The differences from the infinite swept wing cases are significant, and conducting experiments in the KRG will not yield the same flowfield. Even when reducing the chord length from $150\,\text{mm}$ to $100\,\text{mm}$ to $50\,\text{mm}$, the differences from the infinite swept wing conditions reduce only

marginally. Specifically, the RMSE between the pressure coefficient in the infinite swept conditions and in the middle of the tunnel decreases from 5.16%, to 4.72%, to 4.56% on the suction side, but increases from 1.43%, to 1.46%, to 1.73% on the pressure side, when decreasing the chord length. This indicates the current setup yields significant differences from the infinitely swept wing conditions. Although the aspect ratio of the wing is increased by a factor of three when reducing the chord length from $c = 150\,\text{mm}$ to $c = 50\,\text{mm}$, no significant improvement of the pressure coefficient distribution can be found. The effect of a reduction in chord length is also only marginally visible at planes outside the middle of the test section. Thus, even for a reduced chord length, it is advised that additional measures are taken to improve the flowfield. It should be noted that the chord-based Reynolds number decreases by a factor of three when choosing the smallest chord over the largest. When decreasing the chord length too much, this may negate the advantage of using a cryogenic tunnel altogether. Additionally, from a structural perspective, it is advisable to maintain a high chord length to prevent decreasing the trailing edge's thickness and thus to keep the model's bending at an acceptable level. This also makes it easier to incorporate instrumentation, such as pressure taps, inside the model. Hence, it is suggested to decrease the chord length only when strictly necessary.

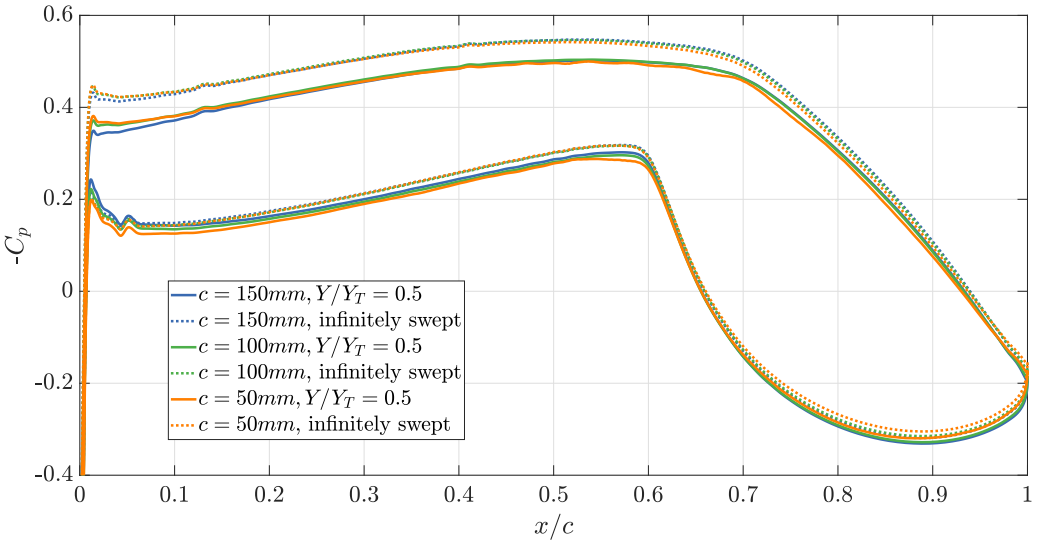

Figure 3.8: Pressure coefficient distribution for different chord lengths. The pressure coefficient is extracted at the middle of the tunnel and compared to that of an infinitely swept wing. The simulations are performed for $\alpha = 0°$, $\Lambda = 15°$, $Ma = 0.65$, and $Re = 7 \times 10^6$.

3.1.4. Influence of the Mach Number

The effect of a variation in Mach number on the evolution of pressure coefficient is shown in Figure 3.9, where a Mach number of $Ma = 0.65$ resulting in a subsonic flowfield, and a Mach number of $Ma = 0.78$ resulting in a transonic flowfield are compared. The pressure coefficients are compared in the middle of the test section to the infinite swept conditions. The pressure coefficient for the smaller Mach number is already shown and analyzed in the previous sections. Hence, this case is presented alongside the results for the higher Mach number to determine the influence of a shock in the flowfield. As can be found from Figure 3.9, the pressure coefficient curve for the transonic case is significantly worse than for the subsonic case. In this case, an increase in Mach number from 0.65 to 0.78 results in conditions that no longer align with the infinitely swept case. While the infinitely swept wing case features a shock on the suction surface at approximately 65% of the chord length, the shock is significantly reduced in strength and shifted upstream by $\Delta x/c = 0.07$ for the three-dimensional case in the tunnel. However, it can be noted that the main deviation is in the region of the shock on the suction surface, whereas the other regions follow a more aligned trend. Hence, depending on the measurement goals, it might be possible that even the region of a favorable pressure gradient on the suction surface can be used for measurements, e.g., regarding transition. Figure 3.10 displays the pressure coefficient for the suction surface of the wing in a continuous color map, allowing for a more precise visualization of the shock location and strength. Towards the walls,

the flow in the tunnel is subsonic and hence no shock is forming. This is caused by the interaction of the flow with the viscous walls of the wind tunnel. When moving towards the middle of the test section, the influence of the walls reduces, and a shock forms above the suction surface of the wing. The strength of the shock can be estimated by the gradient in the pressure coefficient and is largest in the middle, with a slight increase towards the outboard wall. However, the location of the shock inside the test section differs greatly and follows the trend of the isobars, as discussed in previous sections. While the shock tends to move aft for the inboard wall, it moves forward for the outboard wall. Compared to infinite swept conditions, the supersonic region forming above the wing is much smaller. This is compensated for by a higher density in the vicinity of the wing. Due to the interaction of the flow with the walls, the overall size of supersonic regions is smaller, and hence the shock strength is reduced.

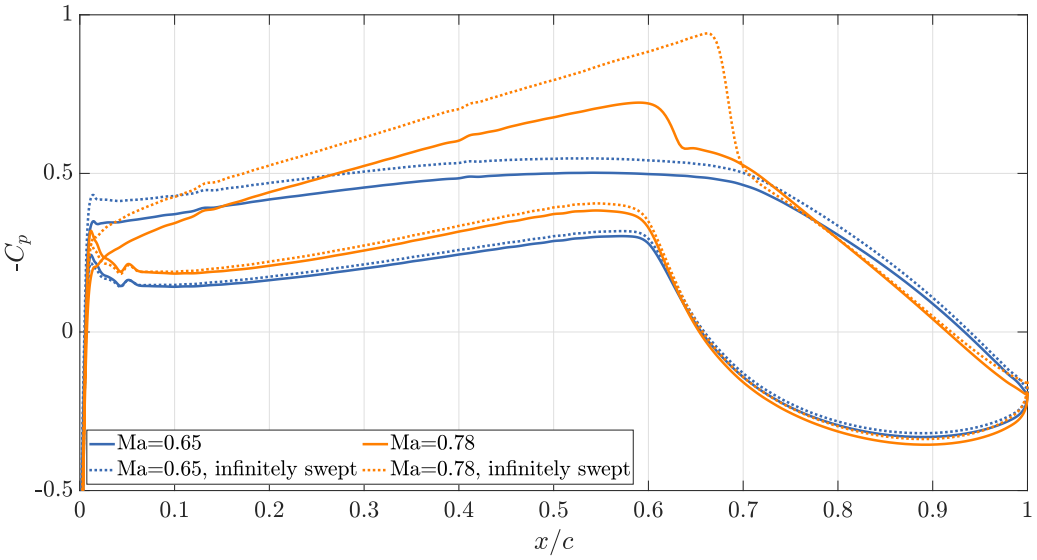

Figure 3.9: Pressure coefficient distribution for two different Mach numbers, extracted at 50 percent of the tunnel width, compared to the infinitely swept wing conditions. The simulations are performed for $\alpha = 0°$, $\Lambda = 15°$, $c = 150\,\text{mm}$, and $Re = 7 \times 10^6$.

It can be concluded that when testing swept wings in the KRG, the influence of the test section walls on the flowfield can be reduced when no shocks are present in the flow. For the presented case, the flowfield differs from infinite swept conditions tremendously when a shock is present.

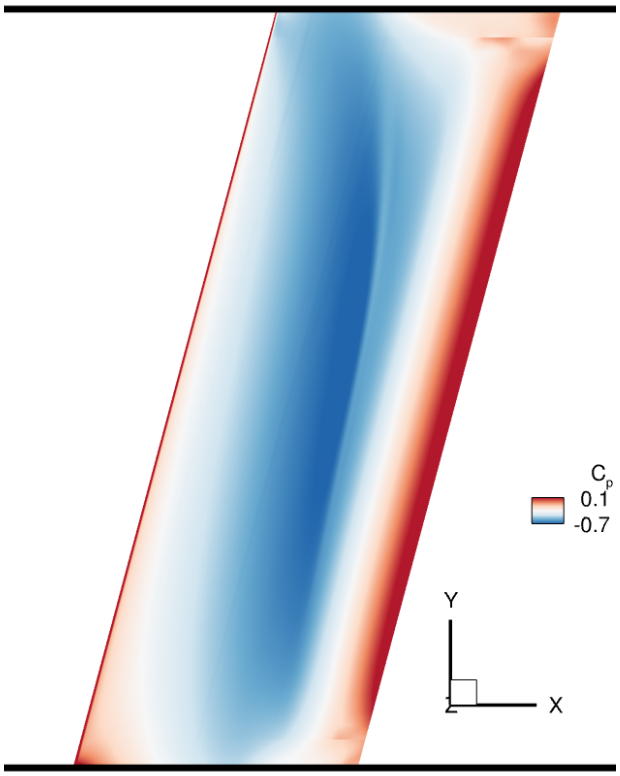

Figure 3.10: Pressure coefficient distribution for the suction side of the wing. The simulations are performed for $\alpha = 0°$, $\Lambda = 15°$, $c = 150\,\text{mm}$, and $Re = 7 \times 10^6$.

3.1.5. Concluding Remarks

The previous sections demonstrate that the current setup of the KRG's test section yields flow conditions that do not align with the infinitely swept conditions in most cases. These conclusions are based on simulations performed on Domain 1. The main findings are presented here in an itemized form.

- The current setup of the KRG yields flow conditions that do not align with the infinitely swept conditions in most cases.
- The difference between the infinite swept conditions and the flowfield in the tunnel is usually larger for the wing's suction than for the pressure surface.
- With the right choice of geometric and freestream parameters, the differences from infinitely swept wing conditions can be minimized, and the flow conditions kept approximately constant over the middle part of the tunnel width.
  - Köhler (2023) identified that angles of attack larger than $\alpha = 2°$ result in a transonic flowfield, even for the lower Mach number studied in this thesis. Hence, the analysis is limited to angles of attack smaller than $\alpha = 2°$. The difference to the flow around an infinite swept wing is significantly increased for $\alpha = 2°$, especially towards the tunnel walls, where flow separation is pronounced. Additionally, the spanwise homogeneity of the flow is reduced due to the influence of the separated flow on the flowfield.
  - The sweep angle is identified as the cause of spanwise gradients in the flowfield. The spanwise homogeneity of the flow can be significantly increased when reducing the sweep angle. Nevertheless, the region of separated flow at the junction of the trailing edges and the walls does not significantly increase in size when the sweep angle is increased. Thus, it is found that the non-dimensionalized spanwise velocity deviates more from the infinite swept conditions for smaller sweep angles.
  - It is found that a change in chord length does not have a considerable influence on the flowfield. The improvements towards infinite swept conditions are fairly small, even for an increase in

aspect ratio by a factor of three. Hence, to keep the chord-based Reynolds number high during the experiment and to be able to build a stiff model that can fit instrumentation within the body, it is recommended to only reduce the chord length when strictly necessary.

  - The Mach number has a significant impact on the flowfield. For subsonic Mach numbers, the pressure distribution for the three-dimensional cases follows the infinite swept conditions to a certain extent. When transonic conditions are studied, the flowfield in the tunnel differs significantly from the unbounded case due to the interaction of the flow with the walls. The location and strength of the shock differ significantly from those in infinite flow conditions. However, this deviation is mainly attributed to the region of the shock. When limiting the measurement region to the favorable pressure gradient on the suction surface, it is possible to arrive at data that does not significantly differ from infinite swept conditions, yet, only after taking measures to reduce the deviation in this region, too.
  - As found by Köhler (2023), the Reynolds number does not have a significant impact on the flow, which is why it is kept constant in the subsequent analysis to reduce the number of parameter combinations.
- Although the offset to infinite swept conditions can be reduced and the spanwise homogeneity of the flow increased by the right choice of geometric and freestream conditions, it is strongly recommended to incorporate measures to mitigate the impact of the vertical walls. Otherwise, depending on the measurement goals, a correct representation of free flight will not be possible in the tunnel's test section, even in the middle of the tunnel, where the influence of the vertical walls is usually smallest.

These findings are supported by Figure 3.11 and Figure 3.12. Figure 3.11 shows the region of flow separation at the outboard tunnel wall in dark gray for a simulation with the highest angle of attack, chord length, and Mach number studied in this thesis. In contrast, Figure 3.12 shows the region of flow separation at the outboard wall in dark gray for a simulation with reduced angle of attack, chord length, and Mach number. This contrast highlights the cumulative effect of various parameters on the flowfield and demonstrates how the choice of parameters has a significant impact on the flowfield. The sweep angle and Reynolds number are kept constant between the two cases, as their influence on flow separation was found to be negligible. The comparison of both figures clearly illustrates the impact of the choice of freestream and geometric parameters on the flow separation. It is found that the larger the region of separated flow, the smaller the spanwise homogeneity of the flow, as the streamlines are deviated around the separation region.

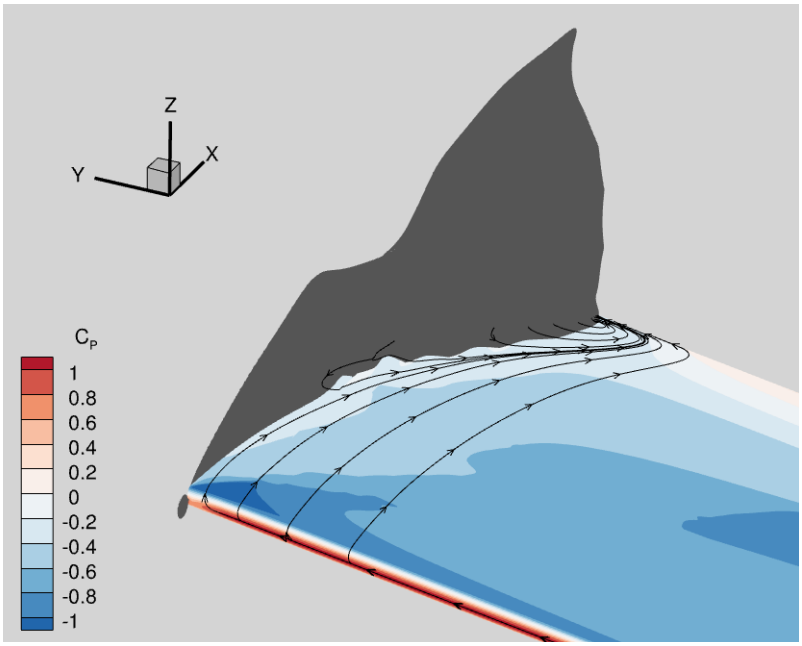

Figure 3.11: Large region of reversed flow at the junction on the outboard wall shown in dark gray. The streamlines around the reversed flow region are shown. The simulations are performed for $\alpha = 2°$, $\Lambda = 15°$, $c = 150\,\text{mm}$, $Ma = 0.78$, and $Re = 7 \times 10^6$.

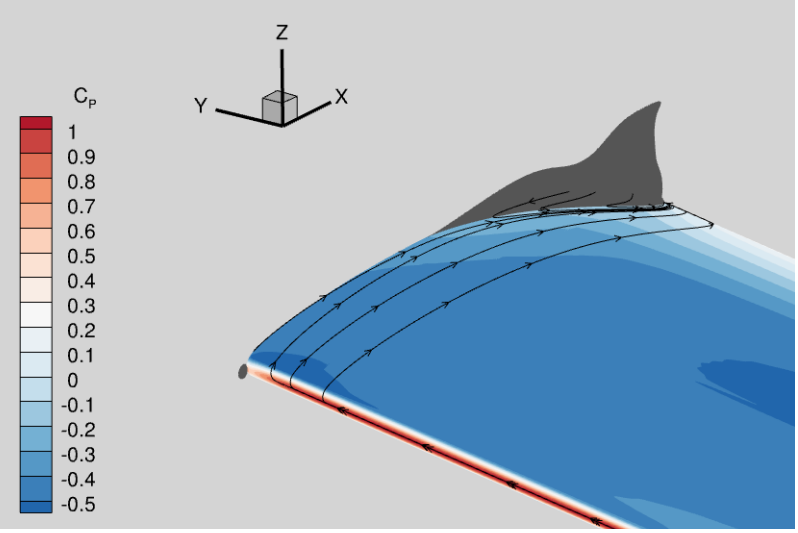

Figure 3.12: Small region of reversed flow at the junction at the outboard wall shown in dark gray. The streamlines around the reversed flow are shown. The simulations are performed for $\alpha = 0°$, $\Lambda = 15°$, $c = 100\,\text{mm}$, $Ma = 0.65$, and $Re = 7 \times 10^6$.

3.2. Results with Two-Dimensionally Deformed Horizontal Walls

Section 3.1 showed results for simulations performed on Domain 1, shown in Figure 2.8a, to give insight into the isolated effect of the side walls of the test section. These, however, are not precisely identical to the conditions that the current setup in the KRG can achieve. Hence, this section presents results for undeformed side walls and two-dimensionally deformed upper and lower walls, which represent the possibilities that can currently be achieved in the KRG's test section. Domain 2, which is shown in Figure 2.8b, is used for the simulations presented in this section.
It is expected that the flow conditions presented in this section deviate even further from infinite swept conditions than the results from the previous section. This is because for a swept wing, the upper and lower tunnel walls should be adapted three-dimensionally to be able to get rid of their influence on the flow. Nevertheless, this is not possible in the KRG's test section, why a deformation that adapts the horizontal walls according to the flowfield in the middle of the test section is used, i.e., the deformation is based on fitting the streamlines in the middle of the test section, but deviates from the ones towards the side walls. Thus, it is expected that the flow towards the middle lies closest to the results presented in Section 3.1, while the flow towards the tunnel walls deviates further. Nevertheless, an influence of the regions at the walls on the middle of the tunnel is expected, which is why analyzing the effect of a combination of side and horizontal walls is studied.

To show the effect of the upper and lower wall on the flowfield pronounced but without a shock, a simulation with $\alpha = 0°$, $\Lambda = 25°$, $c = 150\,\text{mm}$, and $Ma = 0.65$ is presented in Figure 3.13, for which the difference between different spanwise planes and the infinite swept wing was already explained in Section 3.1.2. In contrast to the previous sections, a higher sweep angle is chosen for this simulation to increase the difference in pressure coefficients between the planes, thereby making it easier to detect the differences between them. As expected, there is a significant difference between the results with and without the horizontal tunnel walls. The RMSE at different spanwise planes between the results on Domain 1 without horizontal tunnel walls and Domain 2 with two-dimensionally deformed tunnel walls is shown in Table 3.3. Surprisingly, the difference is least for a spanwise position of $Y/Y_T = 0.1$ and increases as the position moves outboard, reaching its maximum near the outboard tunnel wall in the front part of the wing. Although the deformation of the horizontal walls is based on the plane in the middle of the tunnel, the pressure coefficient aligns better for the plane at the inboard wall. This is likely caused by the smaller perceived angle of attack at the inboard wall and, thus, a smaller suction peak near the leading edge, which decreases the susceptibility to variations in the freestream. The region of flow separation at the junction of the trailing edge and the walls remains unchanged in size. Equally, the regions of favorable and adverse pressure gradients on the wing do not deviate dramatically, which can be an indication that the laminar-to-turbulent transition mechanism does not change between both cases.

In conclusion, the results presented in this section demonstrate that deforming the upper and lower walls two-dimensionally to eliminate their influence on the three-dimensional flowfield is not feasible. This aligns well with findings in the literature.

Table 3.3: Root mean square error of the pressure coefficient distributions at different spanwise planes, comparing the difference between the results of both domains. The simulations are performed for $\alpha = 0°$, $\Lambda = 25°$, $c = 150\,\text{mm}$, $Ma = 0.65$, and $Re = 7 \times 10^6$.

Tunnel Width	10%	50%	90%
RMSE suction side	1.17%	2.71%	4.89%
RMSE pressure side	1.48%	2.64%	4.18%

This chapter has shown that the flowfield in the KRG's test section can deviate substantially from that of the infinite swept wing. Hence, it is advisable to implement measures that reduce the influence of the side walls on the spanwise homogeneity of the flowfield, which is presented in the next chapter by introducing deformed side walls.

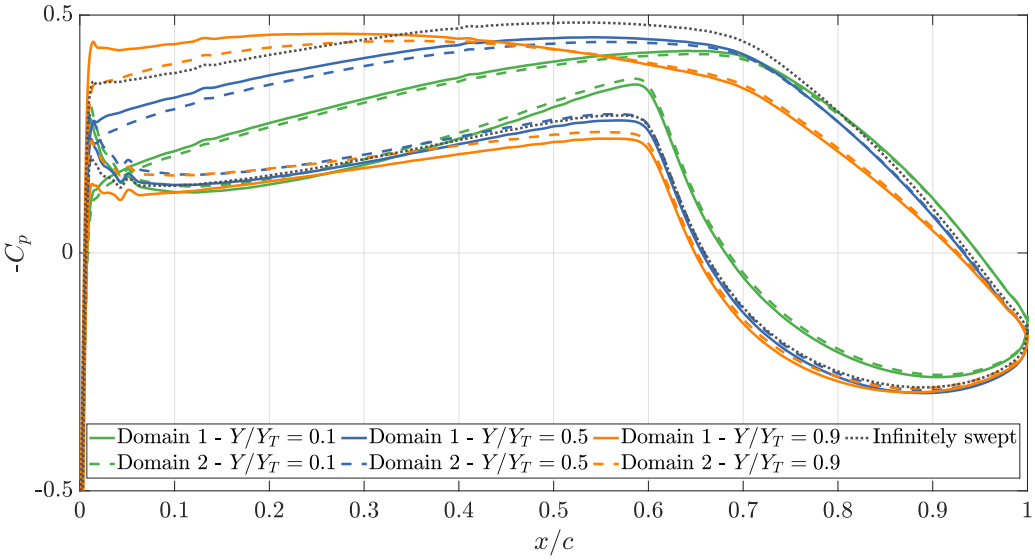

Figure 3.13: Pressure coefficient distribution for different spanwise locations in the test section. The results for two domains are compared: Domain 1, featuring undeformed horizontal walls at a large distance, and Domain 2, which has two-dimensionally deformed horizontal walls. The simulations are performed for $\alpha = 0°$, $\Lambda = 25°$, $c = 150\,\text{mm}$, $Ma = 0.65$, and $Re = 7 \times 10^6$.

4

Results with Deformed Side Walls

Chapter 3 showed that swept-wing simulations in the KRG without the deformation of side walls yield results that deviate from infinitely swept wing conditions significantly. Additionally, the spanwise flow homogeneity is low, making the measurement results highly sensitive to the measurement location. Hence, this chapter introduces deformed side walls and presents results showing the beneficial effect of side wall deformation, whose procedure is explained in Section 2.4, on the spanwise flow homogeneity. In the following section, each simulation is performed with a different deformation of the side walls, i.e., the wall deformation is adapted for any change in freestream and geometric parameter.

Initially, results are presented for deformed inviscid side walls, but without horizontal walls, to provide motivation for the choice and effectiveness of deformed side walls in improving spanwise flow homogeneity. Thereafter, results with deformed viscous walls and without horizontal walls are presented to show how deformed walls improve the spanwise flow homogeneity compared to the results presented in Chapter 3. Finally, a combination of deformed side walls and horizontal walls is shown to indicate expected flow conditions in the test section after installing contoured wall liners.

4.1. Results with Deformed Inviscid Side Walls and without Horizontal Walls

Initially, inviscid tunnel walls are used to determine the effect of deformed side walls on the flow within the test section. The trends examined in these simulations are indicative of the significant improvement in flow conditions that adaptive walls provide. Nevertheless, it is essential to note that the results are obtained with inviscid tunnel walls, and, for example, no flow separation occurs under the tested conditions, which was found as a severe driver of spanwise inhomogeneities in Chapter 3. Domain 1, as shown in Figure 2.8a, is used for simulations with deformed side walls and no horizontal walls, isolating the effect of the side walls on the flow from the effect of the horizontal walls.

To determine a feasible deformation that yields an improvement of flow homogeneity, two- and three-dimensional deformations are tested for inviscid tunnel walls. To determine how well the deformations work, a comparison is made with the undeformed side walls and the infinitely swept wing case in Figure 4.1 for two spanwise planes close to the inboard and outboard tunnel walls. Nevertheless, the middle of the test section shows the same trends, albeit less pronounced. The freestream and geometric conditions are chosen to feature a high sweep angle, resulting in a significant deformation, but a moderate Mach number to exclude effects related to shocks.

The two-dimensional deformation follows only one streamline extracted from the infinitely swept wing simulations at $Z = 0.06\,\text{m}$, i.e., roughly $1/3c$ above the suction surface of the wing. This deformation is applied to all Z-locations of the tunnel side walls. As the deformation is only two-dimensional, there is no discontinuity that the deformation tool has to handle, as was explained in Section 2.4. However, the deformation will be only a rough approximation, as it only fits the flowfield $1/3c$ above the suction surface of the wing. Specifically, a higher deviation from infinitely swept conditions is expected on the pressure side of the wing.

In Figure 4.1, the flowfield with undeformed side walls, two-dimensional deformed walls, and three-dimensional deformed walls is compared. The presented parameters differ from the baseline case in a

higher sweep angle. This sweep angle is chosen to increase the difference in pressure coefficients between the planes and different cases, thereby making the effect of different deformations more pronounced. The difference in shape between the pressure coefficients for both planes is expected, since the more upstream part of the wing induces an upwash of the fluid on the more downstream part of the wing. This effect is well known, and in aircraft, it is accounted for by employing washout on the wings (Obert 2009). Even for a perfectly deformed tunnel wall, this difference would not be eliminated completely.
As could already be found in Chapter 3, the results with straight side walls differ substantially from the infinite swept wing. Regarding the two-dimensional deformed walls (dotted lines) on the suction surface, they generally improve the results, i.e., result in a flowfield closer to the infinitely swept wing case. For the pressure side of the wing, only a slight improvement for the $Y/Y_T = 0.1$ plane can be found, while for the $Y/Y_T = 0.9$ plane, the pressure coefficient is even more deviating from infinitely swept conditions than for the straight side walls. This difference between the suction and pressure surfaces is explained by the two-dimensional deformation, where a streamline from above the wing is chosen in the infinitely swept conditions for all Z-locations. Hence, the shape of the side wall below the wing is shaped based on a streamline from above the wing, which improves the flowfield only on the suction and not necessarily on the pressure side.
To compensate for this inaccuracy, a three-dimensional deformation is chosen, as it was explained in Section 2.4. The dashed lines in Figure 4.1 show a significant improvement of the pressures on the suction side towards infinite swept conditions. The RMSE between the suction side's pressure coefficient for the three-dimensionally deformed cases and the infinitely swept conditions is roughly half as high as the RMSE between the suction side's pressure coefficient for the undeformed cases compared to the infinitely swept conditions. For the pressure side of the wing, this improvement is slightly smaller, yet noticeable. It can be observed that for both planes, particularly on the suction side of the wing, the favorable pressure gradient is reduced. Thus, the deformation will not only influence the flowfield in terms of pressure but also have an effect on the laminar-to-turbulent transition.

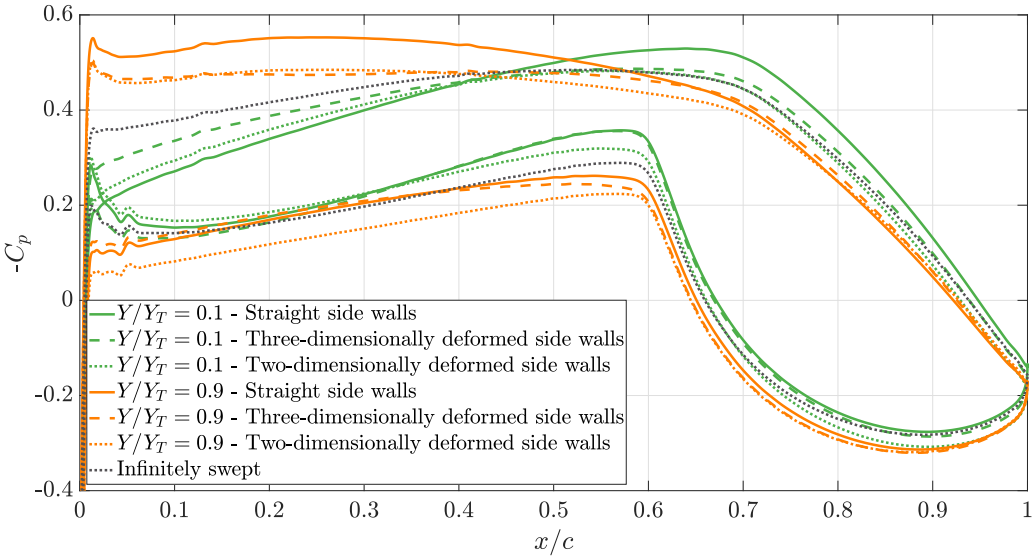

Figure 4.1: Pressure coefficient distributions for different deformations. The spanwise locations in the tunnel are close to the inboard and outboard walls. The simulations are performed for $\alpha = 0°$, $\Lambda = 25°$, $c = 150$ mm, $Ma = 0.65$, and $Re = 7 \times 10^6$.

Following, a three-dimensional deformation of the side walls is chosen for the subsequent analysis. Deforming the side walls yields a flowfield that aligns more closely with infinitely swept conditions in two aspects. First, the difference in pressure coefficient distributions to the infinitely swept case is reduced, and second, an increase in spanwise homogeneity is achieved. These effects are explained by the flow, which can, especially at the tunnel walls, move more according to its natural, unbounded way. The movement of the streamlines at the tunnel walls is not impeded by the walls as strictly as for the straight tunnel walls, which can be seen in Figure 4.2. It shows the spanwise offset of the boundary-layer edge streamline for

different tunnel widths. The offset is calculated by subtracting the Y-coordinate of the most downstream end of the streamline at the boundary layer edge, i.e., at the trailing edge, from the Y-coordinate of the most upstream point of the streamline, i.e., at the trailing edge. By employing this method, it is possible to get a rather quick assessment of the movement of the streamlines at the boundary layer edge. A shortcoming of this method is that it neglects the exact curvature of the streamlines and only considers the start and end points of the streamlines. This figure illustrates the spanwise offset of the boundary layer edge streamline on the suction surface of the wing, as the spanwise offsets on the pressure side are relatively small compared to those on the suction surface.
For this figure, it can be observed that the spanwise offset for the simulations performed in the tunnel decreases towards the walls and reaches a maximum at the midplane of the tunnel. This is a natural behavior, since the streamlines at the walls must follow their contour and are less influenced by the walls in the middle of the test section. Thus, the spanwise offset of the streamlines is zero at the walls in the case of straight walls and reaches a value closer to infinitely swept wing conditions towards the middle of the test section. It is observed that the simulations without a deformation of the side walls fail to achieve an offset close to infinitely swept wing conditions. When deformed side walls are used, two notable features can be observed. Both effects will later be demonstrated for simulations with viscous side walls as well, and are essential for experiments in the tunnel that aim to represent infinitely swept wing conditions.
First, the curves tend to flatten out towards the walls. This is, to no surprise, caused by the requirement that the streamlines at the walls need to follow their contour. As the contour of the walls features a spanwise offset, so will the streamlines close to them. This achieves a flatter curve towards the middle of the test section. This effect is a promising result, as the more constant the flow conditions over a large width of the test section, the better different measurements can be performed in the tunnel and the less dependent the measurements are on location.
Secondly, the curves shift upwards and closer to infinitely swept wing conditions, especially towards the middle of the test section. It indicates that, concerning the spanwise offset of the boundary layer edge streamline, reaching infinitely swept wing conditions is achievable when deformed side walls are employed. The described trend holds true for all three presented sweep angles. However, the higher the sweep angle, the more pronounced the benefit of the side wall deformation is, as the offset of the inviscid streamlines is higher for increasing sweep angles.

After this brief introduction of the effects that deformed side walls generate, a more thorough analysis of the flowfield with deformed side walls will be performed in the following section.

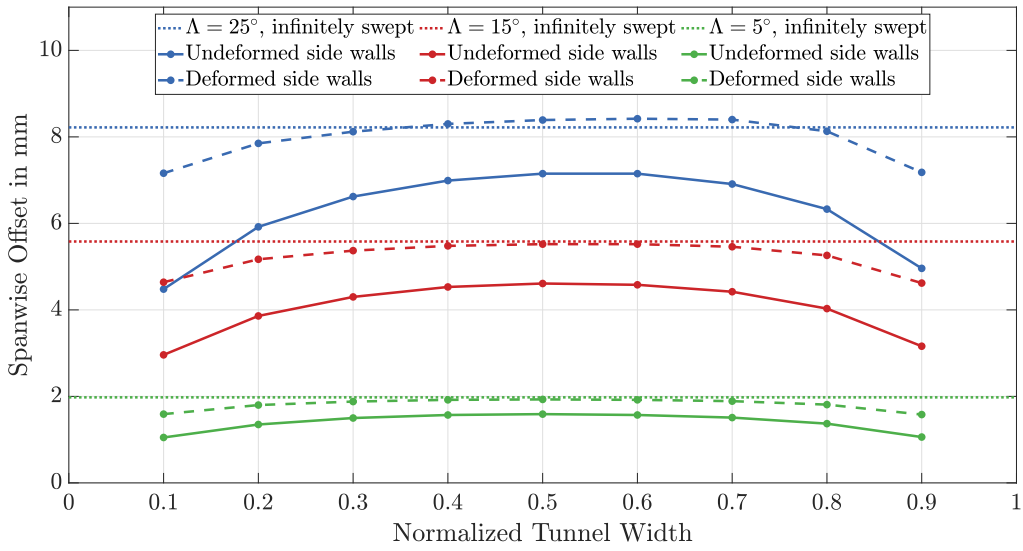

Figure 4.2: Spanwise offset of the boundary layer edge streamline for undeformed and three-dimensionally deformed vertical tunnel walls compared with infinitely swept wing conditions. Domain 1 with extended horizontal walls is used. The simulations are performed for $\alpha = 0°$, $c = 150\,\text{mm}$, $Ma = 0.65$, and $Re = 7 \times 10^6$.

4.2. Results with Deformed Viscous Side Walls and without Horizontal Walls

After the results in Chapter 3 have demonstrated that experiments in the KRG under current conditions yield results that significantly deviate from swept conditions, adjusting the setup in the test section is recommended to achieve improved flow conditions. Section 4.1 introduced the effects of deformed tunnel walls on the flowfield for the simulation with inviscid tunnel walls. To gain a more detailed understanding of the actual conditions in the flowfield, simulations with viscous tunnel walls are performed, whose results are presented in this section. The simulations presented in this section utilize Domain 1, as shown in Figure 2.8a. Hence, an isolated analysis of the vertical wall's influence on the flowfield is performed. The scope of this section is to show the possibilities of achieving conditions in the KRG's test section that align closely with the infinitely swept wing conditions for a significant width of the test section, i.e., featuring a large spanwise homogeneity.

Figure 4.3 shows alongside the friction and pressure coefficients for two simulations performed at $\Lambda = 25°$. The results of this simulation with the highest sweep angle are chosen to present the differences between the undeformed side walls, shown in Figure 4.3a, and the deformed side walls, shown in Figure 4.3b. As can be found from both friction coefficients, the region of reversed flow is not significantly reduced in size for the deformed side walls. Following from the observations of the results presented in Chapter 3, this is a first indication that the flow close to the walls will likely not align with infinite swept wing conditions due to the displacement of the flow towards the junction of the trailing edge and the walls. Nevertheless, when comparing the black lines, which indicate lines of constant pressure coefficient, it is observed that, especially towards the middle of the test section, the shape of the lines is more aligned with the leading edge in the deformed case. This indicates a flowfield that closely follows the conditions of an infinite swept wing. Only to the walls, the effect is reduced, and the isobars do not follow the leading edge any longer. From this first comparison, it seems feasible to significantly improve the flowfield towards achieving infinite swept wing flow conditions, despite the separated flow at the tunnel walls.

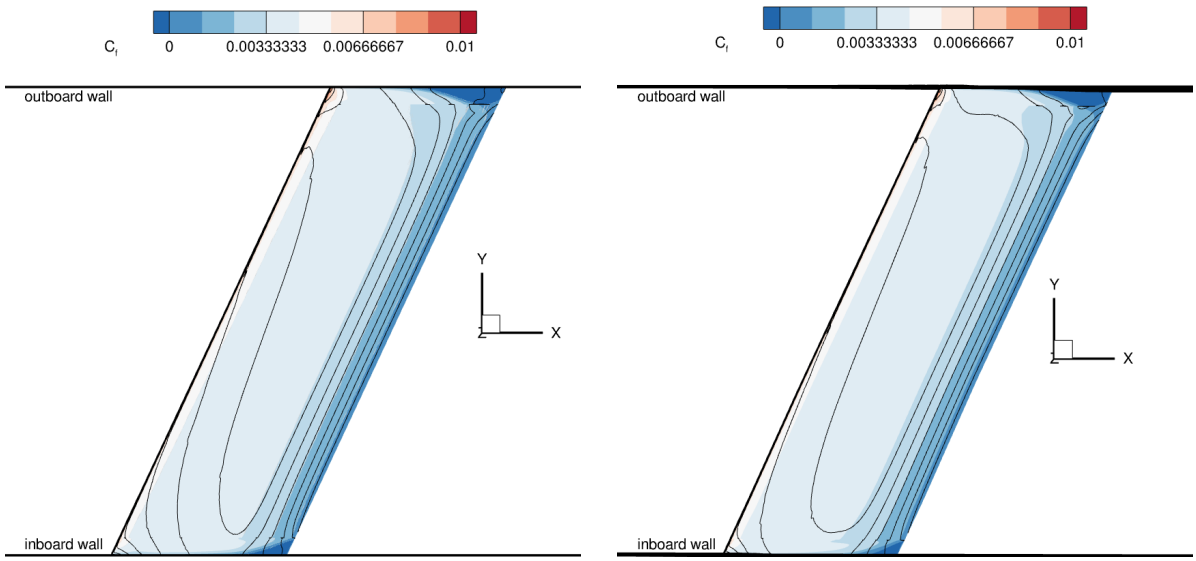

Figure 4.3: Comparison of friction and pressure coefficients. The colormap shows the friction coefficient, and the black lines show lines of constant pressure coefficient for the suction side of the wing. The simulations are performed for $\alpha = 0°$, $\Lambda = 25°$, $c = 150\,\text{mm}$, $Ma = 0.65$, and $Re = 7 \times 10^6$. (a) For undeformed side walls. (b) For deformed side walls.

4.2.1. Effect of the Turbulence Model

As introduced in Section 2.2.3, different turbulence models can be used to model the Reynolds stresses. The simulations used in this thesis are based on the Spalart-Allmaras turbulence model. As the simulations with viscous, deformed tunnel walls make up the majority of the work performed in this thesis, the comparison

of results obtained using the SA model with those obtained using the $k-\omega$ turbulence model is presented in this section.

Figure 4.4 shows the pressure coefficients for two simulations with the baseline parameter combination. The colormap is the result of a simulation performed with the $k-\omega$ turbulence model; the black lines indicate constant pressure for a simulation performed with the SA turbulence model. It can be observed that the differences in pressure coefficients are slight but recognizable, especially near the inboard wall. Additionally, Figure 4.5 shows the regions of separated flow in red for a simulation performed with the $k-\omega$ turbulence model and in blue for a simulation performed with the SA turbulence model. The walls are shown in light gray. As can be found from Figure 4.5a, the region of flow separation is slightly larger when using the $k-\omega$ turbulence model. At the outboard wall, the location of the flow separation is not distributed equally, as Figure 4.5b shows.
Finally, the comparison of the lift and drag coefficients between the two simulations reveals that the one performed with the SA turbulence model predicts a slightly higher lift and a higher lift-to-drag ratio ($L/D = 26.96$) compared to the simulation performed with the $k-\omega$ model ($L/D = 25.77$).

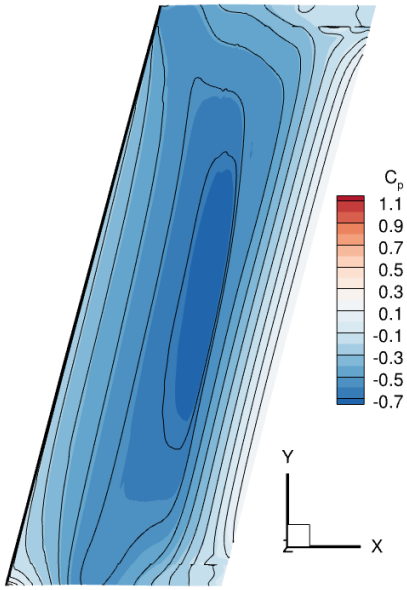

Figure 4.4: Pressure coefficient for the suction side of the wing. The colormap displays the results of simulations conducted using the $k-\omega$ turbulence model, while the black lines represent results obtained with the Spalart-Allmaras turbulence model. The simulations are performed for $\alpha = 0°$, $\Lambda = 15°$, $c = 150\,\text{mm}$, $Ma = 0.65$, and $Re = 7 \times 10^6$.

This section demonstrates that the choice of turbulence model can impact the simulation results. It seems that although different measures to compare the results of the turbulence model yield slightly different results, it is unlikely that the minor differences will affect the overall outcome and conclusions of this thesis. To conserve computational resources, the SA turbulence model is employed in this thesis. Nevertheless, it is essential to note that the choice of turbulence model has an impact on the results and can affect the outcome of certain simulations.

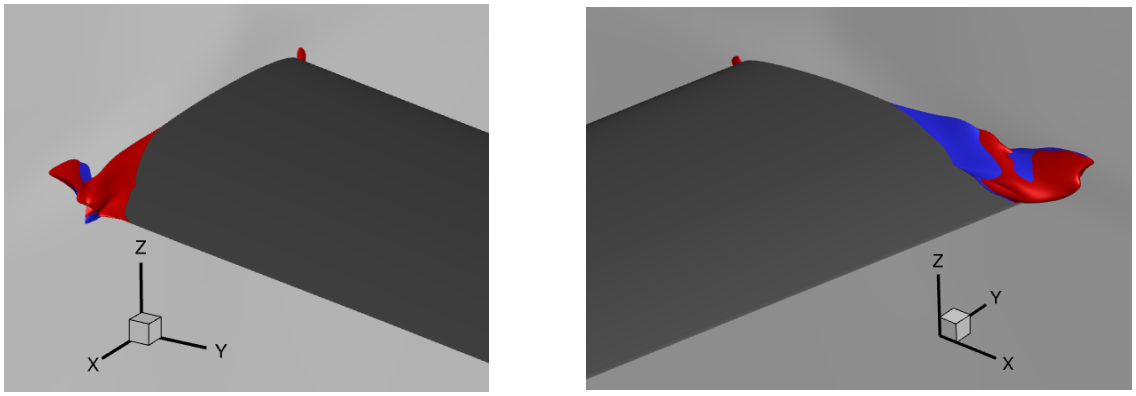

(a) (b)

Figure 4.5: Region of flow separation shown in blue for simulations performed with the Spalart-Allmaras turbulence model and in red for simulations performed with the $k-\omega$ turbulence model. The tunnel walls are indicated in light gray. The simulations are performed for $\alpha = 0°$, $\Lambda = 15°$, $c = 150\,\text{mm}$, $Ma = 0.65$, and $Re = 7 \times 10^6$. (a) For the inboard tunnel wall. (b) For the outboard tunnel wall.

4.2.2. Influence of the Angle of Attack

As shown in Chapter 3, a higher angle of attack increases the difference to the infinitely swept wing conditions, mainly caused by the large recirculation region at the walls and the higher offset of streamlines around the wing in general. This section presents results for angles of attack of $\alpha = 0°$ and $\alpha = 2°$ for undeformed and deformed side walls. Figure 4.6 shows the pressure coefficients for both angles of attack at 30 and 70 percent of the tunnel width. The results are presented for deformed and undeformed side walls. It can be found that the difference to the infinite swept wing condition on the suction side is reduced for both angles of attack when the walls are deformed. The pressure side does not show a significant improvement. In general, the suction side of the wing is more susceptible to a change in wall shape, as the gradients over the suction side are higher than over the pressure side. Also, the spanwise homogeneity is increased for both angles of attack and the deformed side walls. It is found that the pressure coefficients for 30 and 70 percent planes of the tunnel width lie closer to each other than for the undeformed side walls. This can also be found when examining the RMSE, which is presented in Table 4.1. For both angles of attack, the difference in the suction side's pressure coefficients between the 30 percent and 70 percent planes is reduced significantly when the side walls are deformed. This increase in spanwise homogeneity aligns with what is found in Section 4.1. Despite the recirculation regions influencing the flowfield, the deformation of the side walls allows the flow to develop in a less constrained manner, resulting in a more homogeneous flowfield in the spanwise direction. However, it should be clearly pointed out that the RMSE between the 30 and 70 percent planes for $\alpha = 2°$ and deformed side walls is still almost 5% for the suction side of the wing. This is caused by the large region of recirculating flow, which is shown in Figure 4.7. This recirculation region forces the flow to channel towards the middle of the test section, hence influencing the flowfield in this region significantly more than for the less pronounced recirculation regions and the smaller angle of attack of $\alpha = 0°$. Depending on the measurement goals in the test section, the difference of 4.93% between the 30 and 70 planes might be too large to achieve a significant width to measure data repeatedly.

In conclusion, the deformation of the side walls increases the alignment with the infinite swept wing conditions and the spanwise homogeneity significantly, although it remains uncertain if the improvement for the case with $\alpha = 2°$ is significant enough to measure precise data repeatedly. This depends primarily on the measurement goals.

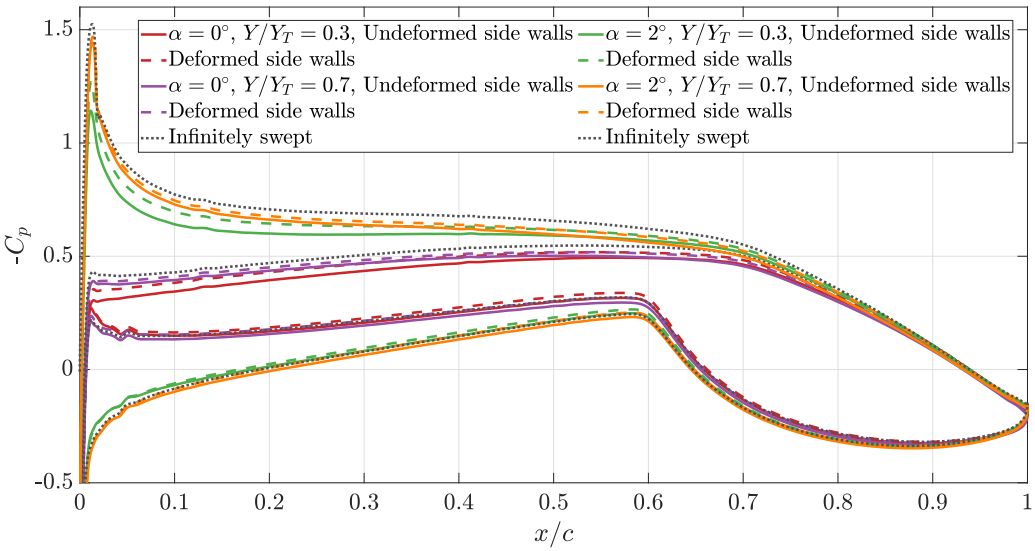

Figure 4.6: Pressure coefficient distribution for deformed side tunnel walls, extracted at different planes of the tunnel width, compared to the infinitely swept wing conditions for two angles of attack. The simulations are performed for $\Lambda = 15°$, $c = 150\,\text{mm}$, $Ma = 0.65$, and $Re = 7 \times 10^6$.

Table 4.1: Root mean square error of the pressure coefficient distributions at the 30 percent plane compared to the 70 percent plane for two different angles of attack and for undeformed and deformed side walls. The simulations are performed for $\Lambda = 15°$, $c = 150\,\text{mm}$, $Ma = 0.65$, and $Re = 7 \times 10^6$.

	Suction side	Pressure side
	$\alpha = 0°$	
Undeformed side walls	4.17%	2.47%
Deformed side walls	2.27%	1.61%
	$\alpha = 2°$	
Undeformed side walls	8.24%	3.06%
Deformed side walls	4.93%	3.15%

Figure 4.7: Friction coefficient on the wing's suction side at the outboard wall for simulations with two angles of attack. The colormap shows the friction coefficient for $\alpha = 0°$, where red indicates regions with positive friction coefficient, and blue indicates regions with zero or negative friction coefficient. The black line indicates the line of zero friction coefficient for $\alpha = 2°$. The simulations are performed for $\Lambda = 15°$, $c = 150\,\text{mm}$, $Ma = 0.65$, and $Re = 7 \times 10^6$.

4.2.3. Influence of the Sweep Angle

Figure 4.8 shows the pressure coefficient distribution at different spanwise planes for deformed tunnel walls and a sweep angle of $\Lambda = 15°$. The corresponding results for the undeformed case are presented in Figure 3.2. The comparison shows that the difference between the pressure coefficient curves is reduced significantly when employing deformed side walls. Quantitatively, the RMSE between the 10 percent and the 90 percent planes for the suction surface is reduced from 11.82% for the undeformed to 7.37% for the deformed case. For the pressure surface, this value decreases less from 4.94% to 4.30%. Comparing the two cases with undeformed and deformed side walls demonstrates the effectiveness of using deformed tunnel walls to achieve more uniform conditions across the tunnel width. Especially towards the tunnel walls, the difference in pressure between the deformed and undeformed walls is significant. Such an effect is expected because the flowfield close to the walls can more closely follow the infinitely swept wing conditions, which are almost independent of the recirculation region, as the size remains roughly constant when deformed side walls instead of undeformed side walls are used. The beneficial effect towards the middle of the tunnel decays, but remains effective. Following that logic, it is found that the difference in pressure coefficient distribution between the 10 percent and 30 percent planes is larger (2.89% for the suction and 2.70% for the pressure side) than that between the 30 percent plane and the 70 percent plane (2.27% for the suction and 1.61% for the pressure side). Compared to the RMSE between the 30 percent and 70 percent planes in the undeformed case, which is 4.17% for the suction side and 2.47% for the pressure side, this represents a significant improvement. That comparison impressively shows how the flow conditions remain more homogeneous in the middle of the tunnel than towards the walls. Not only does the RMSE indicate a small difference between the 30 percent and 70 percent planes, but their shapes are also similar, which reinforces the impression of similar flow conditions. This is explained by a combination of the improved deformation, which yields an overall more homogeneous flowfield, and the recirculation close to the wall. This recirculation significantly affects the flow near the wall and substantially alters the pressure distributions. Spanwise positions close to the middle of the tunnel benefit from the deformation because the flow is more homogeneous, and are, due to their distance to the walls, influenced less by the alternation of the flow around the recirculating region.

Compared to infinitely swept wing conditions, an improvement over the undeformed case is also observed. Table 4.2 shows the RMSE between different planes in the tunnel and the infinitely swept conditions. The results for the simulations with straight walls are presented in Table 3.2. The numbers presented above indicate that deformed side walls improve both the spanwise flow homogeneity and the alignment with infinitely swept wing conditions in the tunnel. Nevertheless, a significant difference remains between the infinite swept wing and the planes close to the tunnel walls, which can be attributed to the presence of recirculation regions at the junction of the trailing edge with the walls. This is supported by the findings for the smaller sweep angle of $\Lambda = 25°$, which will be presented and explained later in this section.

Table 4.2: Root mean square error of the pressure coefficient distributions at a certain spanwise plane compared to the infinitely swept wing case. The simulations are performed for $\alpha = 0°$, $\Lambda = 15°$, $c = 150\,\text{mm}$, $Ma = 0.65$, and $Re = 7 \times 10^6$ with deformed side walls.

Tunnel Width	10%	30%	50%	70%	90%
RMSE suction side	7.23%	4.34%	3.12%	2.41%	5.42%
RMSE pressure side	3.44%	2.18%	1.48%	0.75%	1.35%

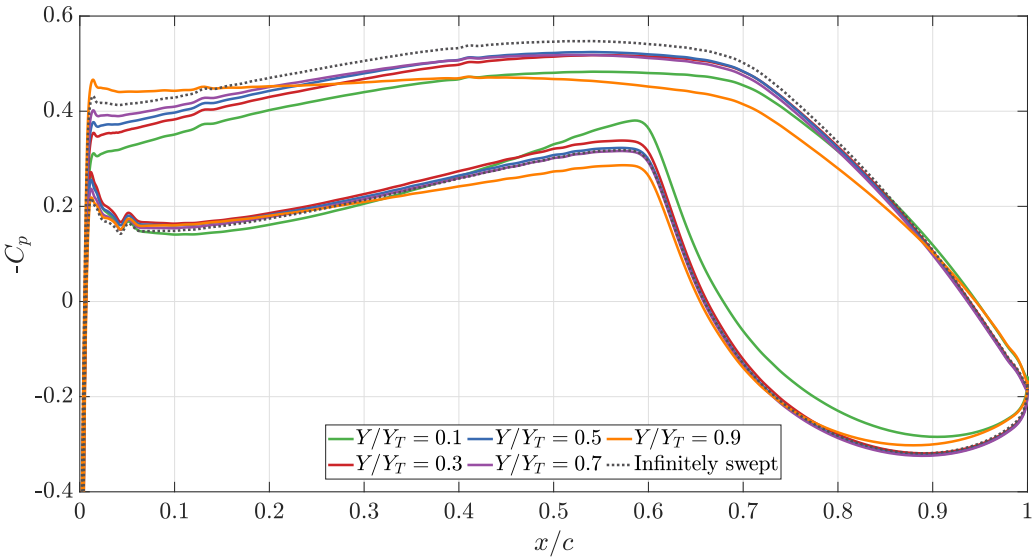

Figure 4.8: Pressure coefficient distribution for deformed side tunnel walls, extracted at different spanwise planes of the tunnel, compared to the infinitely swept wing conditions. The simulations are performed for $\alpha = 0°$, $\Lambda = 15°$, $c = 150$ mm, $Ma = 0.65$, and $Re = 7 \times 10^6$.

When the sweep angle is increased, the difference in pressure coefficient distributions between different planes becomes larger. For the deformed case, the pressure coefficient distributions are shown in Figure 4.9. The contrary is observed for a reduction in sweep angle, as shown in Figure 4.10. Both cases show that the planes close to the inboard (10 percent) and outboard (90 percent) walls exhibit pressure coefficient distributions that vary significantly in shape and magnitude from the remaining pressure coefficient distributions towards the middle of the tunnel and from the infinitely swept wing case. As one approaches the midplane of the tunnel, the difference in shape and magnitude between the pressure coefficient curves decreases. These discrepancies have various reasons, with the main driver being the influence of the upstream parts of the wing by the more downstream parts, and vice versa. The upwash generated by the upstream parts of the wing results in a higher perceived angle of attack for the downstream parts of the wing. However, the misalignment of the pressures in the region of the adverse pressure gradient is significantly influenced by the flow separation at the trailing edges. Even for a small sweep angle of $\Lambda = 5°$, the discrepancy between the infinite swept wing and the 10 and 90 percent planes is large. This suggests that the difference cannot be attributed solely to improper deformation, as the specified deformation for a case with a low sweep angle is only marginal.

Nevertheless, the behavior towards the test section's walls and midplane is differently pronounced for a variation in sweep angle. Where the RMSE between the 10 percent and 90 percent planes is 10.05% for the suction and 9.96% for the pressure side in the case with a sweep angle of $\Lambda = 25°$, it reduces to 2.83% for the suction and 1.51% for the pressure side for the sweep angle of $\Lambda = 5°$. This observation is indicative that even with deformed tunnel walls, a higher sweep angle will yield flow conditions close to the wall that are not indicative of unbounded cases. As shown for the case with a sweep angle of $\Lambda = 15°$, the RMSE between the 30 percent and 70 percent planes was determined to be 2.27% for the suction side and 1.61% for the pressure side. This difference decreases even further when the sweep angle is decreased to $\Lambda = 5°$. It is then determined to be 0.85% for the suction side and 0.55% for the pressure side. This is a strong indication that the sweep angle is a major driver of spanwise inhomogeneities and that a decrease in sweep angle results in a dramatically more homogeneous spanwise flowfield, especially in the middle of the test section.

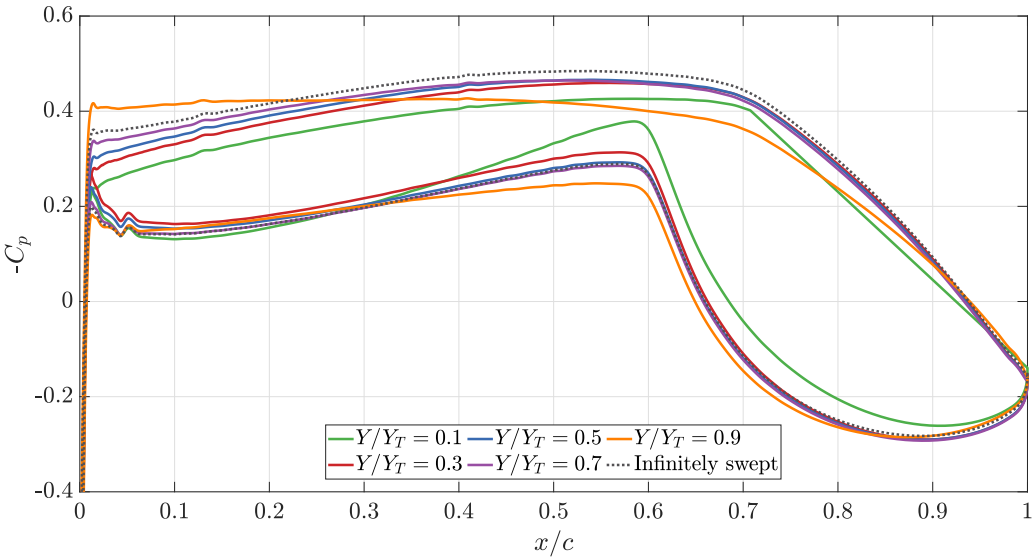

Figure 4.9: Pressure coefficient distribution for deformed vertical tunnel walls, extracted at different spanwise planes of the tunnel width, compared to the infinitely swept wing conditions. The simulations are performed for $\alpha = 0°$, $\Lambda = 25°$, $c = 150$ mm, $Ma = 0.65$ and $Re = 7 \times 10^6$.

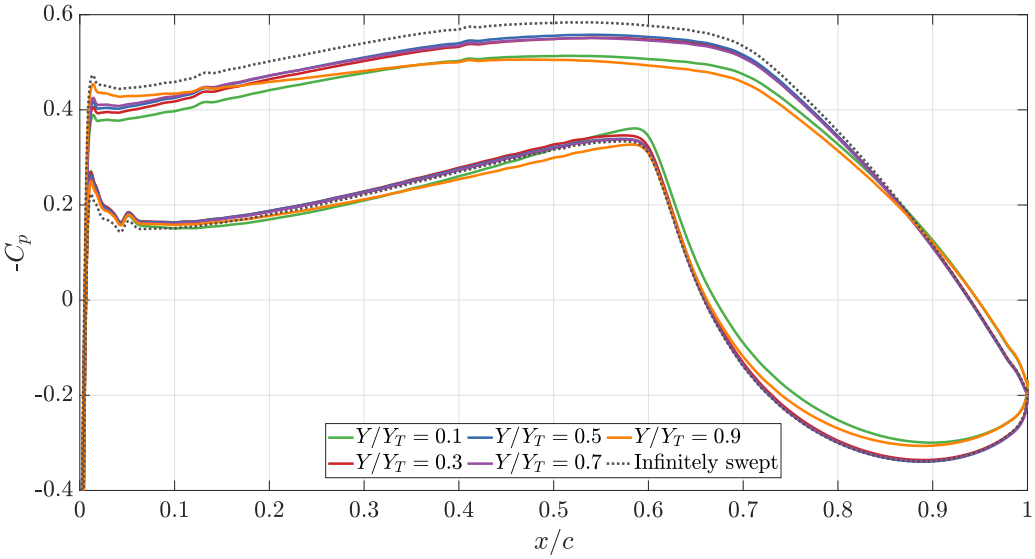

Figure 4.10: Pressure coefficient distribution for deformed vertical tunnel walls, extracted at different spanwise planes of the tunnel width, compared to the infinitely swept wing conditions. The simulations are performed for $\alpha = 0°$, $\Lambda = 5°$, $c = 150$ mm, $Ma = 0.65$ and $Re = 7 \times 10^6$.

The non-dimensionalized boundary layer edge velocity in spanwise direction is shown in Figure 4.11 for the reduced sweep angle of $\Lambda = 5°$. This figure shows again how the difference from the infinite swept wing is noticeable, especially when moving away from the middle of the test section. It also shows that the spanwise velocity in the middle of the tunnel is roughly constant along the chord, indicating conditions aligning with the infinitely swept wing case. However, the alignment with the infinite swept conditions is only improved in terms of shape, i.e., homogeneity of the flow along the chord, but not in terms of absolute numbers.

In conclusion, the trend observed in the simulations in Chapter 3 remains. A decrease in sweep angle typically results in lower deviations of the flowfield from the infinite swept wing case in the middle of the

tunnel. This is primarily caused by the distance to the separated flow, which alters the direction of the flow in the tunnel. Using deformed walls instead of undeformed walls improves the spanwise homogeneity of the flow to an extent, where experiments representing infinitely swept wing conditions seem possible. The flow homogeneity in the middle of the tunnel is increased to an extent where a significant tunnel width can be used to acquire data during measurements. As the walls are deformed according to inviscid streamlines from the infinite swept case and the displacement thickness of the boundary layer, the non-uniform blockage that arises due to the sweep angle is not accounted for in the deformation. This is an additional factor that explains why an increase in sweep angle increases the difference from infinite swept wing conditions. However, due to the complexity of accounting for non-uniform blockage in an iterative procedure, the deformation performed in this work does not take it into consideration. Additionally, the influence of the non-uniform blockage is less than in a closed test section, as Domain 1 has the upper and lower walls placed at a considerable distance from the wing, allowing the flow to deviate to the top and bottom.

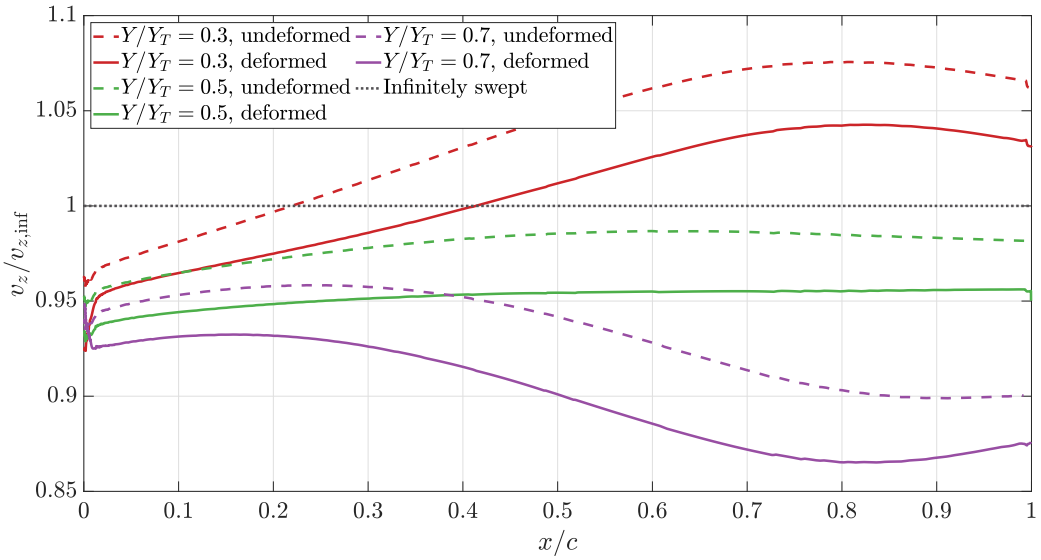

Figure 4.11: Boundary layer edge velocity of the suction side in body-fixed spanwise direction for different locations within the tunnel width is compared. The velocities for deformed and undeformed tunnel walls are shown. The simulations are performed for $\alpha = 0°$, $\Lambda = 5°$, $c = 150\,\mathrm{mm}$, $Ma = 0.65$, and $Re = 7 \times 10^6$.

4.2.4. Influence of the Chord Length

The effect of the deformation on the difference in pressure coefficient distribution is also clearly noticeable for the reduced chord length of $100\,\mathrm{mm}$. Table 4.3 shows the RMSE for different spanwise planes in the tunnel compared to the infinitely swept case. The results are presented for simulations with a chord length of $c = 150\,\mathrm{mm}$, as already shown in the previous sections, and for a reduced chord length of $c = 100\,\mathrm{mm}$. As shown for the larger chord length in the previous sections, the difference from the infinite swept wing conditions is reduced when using deformed side walls.

However, when comparing the increase in alignment between the two chord lengths, no meaningful difference can be spotted. It seems as if the improvement from the undeformed to the deformed tunnel walls impacts both chord lengths in roughly the same manner. In accordance with Chapter 3, it can be said that reducing the chord length yields results more closely aligning with the infinitely swept wing conditions, especially for the suction surface of the wing. The smaller chord length benefits the flow homogeneity in two ways. First, the region of separated flow is smaller for the reduced chord length. Thus, the spanwise influence of the separated region on the flow in the middle of the tunnel is reduced. Secondly, the spanwise movement across a smaller chord, in an absolute sense, is reduced. Both effects show the benefit of using a smaller chord when trying to achieve infinite swept wing conditions, despite the improvements being small.

The relative improvement for both cases is roughly the same, yet slightly better for the case with a chord length of $c = 150$ mm, when comparing the RMSE values in Table 4.3. A possible explanation lies in the deformation of the tunnel walls. While the chord length is decreased, the same Z-location as for the larger chord length is used to determine the streamline closest to the wing, which is used for the deformation. For the reduced chord length, this results in a deformation less closely aligned with the infinitely swept wing conditions. A possible reduction of this inaccuracy is to use streamlines closer to the airfoil, as explained in Section 2.4. However, this approach is not employed in this thesis due to issues with mesh quality resulting from the use of the TAU deformation tool. Most likely, when using fully three-dimensional deformations, the effect explored in Chapter 3 would continue for the deformed cases as well, and a reduction in chord length would yield results with more homogeneous flow conditions.

Table 4.3: Root mean square error of the pressure coefficient distributions at a certain spanwise plane compared to the infinitely swept wing case. The simulations are performed for $\alpha = 0°$, $\Lambda = 15°$, $Ma = 0.65$, and $Re = 7 \times 10^6$.

Tunnel Width Chord length	$Y/Y_T = 0.3$ $c = 100/150$ mm	$Y/Y_T = 0.5$ $c = 100/150$ mm	$Y/Y_T = 0.7$ $c = 100/150$ mm
Undeformed Side Walls			
Suction side	6.88% / 7.33%	4.72% / 5.16%	3.32% / 3.70%
Pressure side	2.26% / 2.12%	1.46% / 1.43%	1.71% / 1.46%
Deformed Side Walls			
Suction side	4.11% / 4.34%	2.57% / 3.12%	1.58% / 2.41%
Pressure side	2.40% / 2.18%	1.24% / 1.48%	0.42% / 0.75%

4.2.5. Influence of the Mach Number

The increase of Mach number from 0.65 to 0.78, i.e., from subsonic to transonic conditions, has shown that the flowfield does not align with the infinitely swept wing conditions any longer in Chapter 3. Even in the midplane of the test section, the difference in, for example, shock location, is significant. This was shown in Figure 3.9 and Figure 3.10. The simulations with the deformed vertical walls fail to significantly increase the spanwise homogeneity of the flowfield, as demonstrated in Figure 4.12. The shock location and strength vary considerably with the spanwise location and differ significantly from the infinitely swept wing conditions.
Figure 4.13 shows the pressure coefficients for the suction surface of the wing for the undeformed side walls (Figure 4.13a) and the deformed side walls (Figure 4.13b). It can be observed that, although the shock does not represent the strength and location of the infinite swept case, an improvement occurs from the undeformed to the deformed side walls. This is not a result of the separation that occurs at the trailing edges, as the regions of separated flow are similar in size for both the undeformed and deformed tunnel walls. The reason for the straightening of the shock is the interaction of the flow with the walls, which results in a more homogeneous flowfield when deformed walls are used.

Although the shock strength and location do not align with those from the infinite swept wing simulations, the region of a favorable pressure gradient aligns to a certain extent with that of the infinite swept wing. If only the forward half of the wing is of interest, the subsonic flowfield might still yield valuable results, for example, regarding experiments for laminar-to-turbulent transition. For example, the RMSE for the pressure coefficient of a simulation with undeformed side walls between the infinite swept case and the midplane of the test section is 7.99% for the suction and 1.88% for the pressure side of the wing, when only using values for $0 < x/c < 0.5$. With deformed side walls, these numbers are reduced to 4.27% and 2.07%, respectively. For the plane at 70 percent of the tunnel width, these numbers further reduce to 2.64% and 1.51%, respectively. It shows that the deformation yields a significant improvement of the alignment with infinite swept wing conditions in the region of a favorable pressure gradient. When an appropriate spanwise location is chosen, the RMSE for this plane compared to infinite swept wing conditions can be reduced to less than 3%, which can be low enough to conduct experiments that yield results representing the infinite swept wing results appropriately.
The difference between the region of favorable and adverse pressure gradients is likely to be caused by the abrupt change of direction of the streamlines at the shock. To yield results close to those of the infinite

swept wing, the contour of the walls must closely represent the streamlines of the infinite swept wing at the shock location.

It is consequently deemed infeasible to conduct experiments for Mach numbers resulting in shocks in the flowfield in the KRG while achieving a flowfield similar to the infinitely swept wing case, when the entire flowfield, and especially the location and strength of the shock, is considered. However, when only the region of a favorable pressure gradient is taken into account, the deformation yields results that align decently with infinite swept conditions, which can be interesting to achieve for experiments regarding transition. Additionally, it is essential to note that due to the deformation method, an exact representation of the wall contour is not possible. Especially in cases where shocks alter the direction of streamlines in the flowfield, this can result in significant influences. Section 4.2.6 explores this effect in more detail.

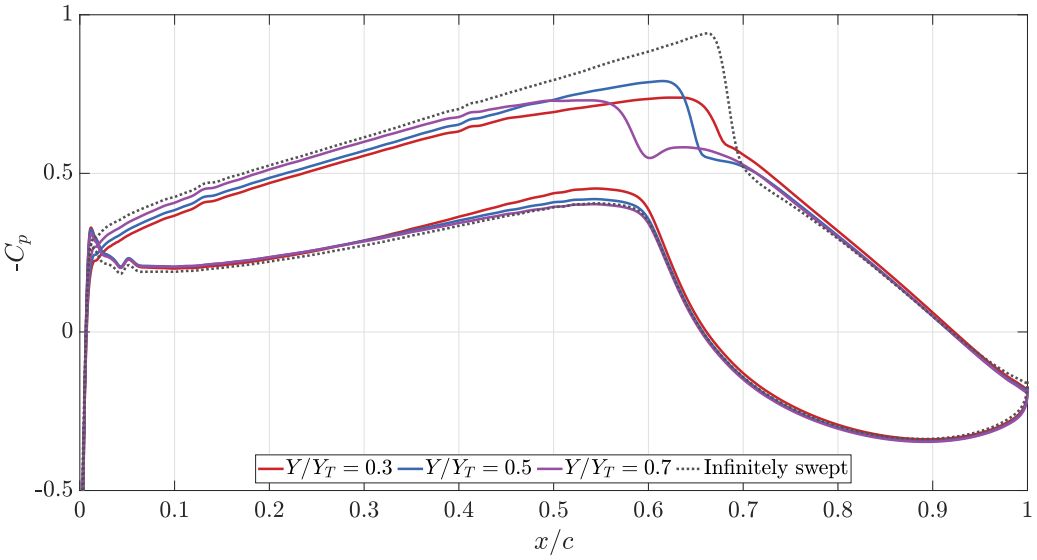

Figure 4.12: Pressure coefficient distribution for deformed vertical tunnel walls, extracted at different spanwise planes of the tunnel width, compared to the infinitely swept wing conditions. The simulations are performed for $\alpha = 0°$, $\Lambda = 15°$, $c = 150\,\text{mm}$, $Ma = 0.78$ and $Re = 7 \times 10^6$.

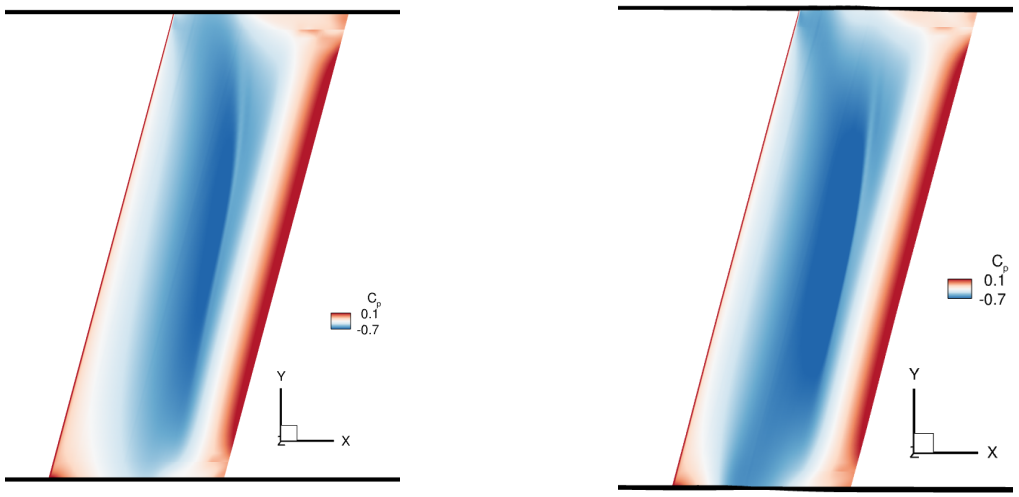

Figure 4.13: Pressure coefficient for the suction side of the wing. The simulations are performed for $\alpha = 0°$, $\Lambda = 15°$, $c = 150\,\text{mm}$, $Ma = 0.78$, and $Re = 7 \times 10^6$. (a) For undeformed side walls. (b) For deformed side walls.

4.2.6. Results with Off-Design Deformation

As introduced in Section 4.2.5, the presence of shocks within the test section poses challenges in maintaining a flowfield close to infinitely swept wing conditions, even with a deformation of the side walls, as shown in Figure 4.13. However, as the presence of shock waves leads to an abrupt change of the shape of the streamlines around the wing, special attention must be paid to cases involving a shock, as explained in Section 4.2.5. This section examines the dependence of the deformation choice on cases with and without a shock in the flowfield.

Figure 4.14 shows the pressure coefficient distributions for a simulation performed for the baseline parameter combination at $Ma = 0.65$, where in the infinitely swept case, no shock is present in the flowfield. For the case with the regular deformation, the deformation is the tailored deformation used for this case, whose results were presented in Figure 4.8. The deformation of the walls for the off-design deformation case is based on the streamlines from a case with a Mach number of $Ma = 0.78$, where in the infinitely swept case, a shock is present in the flowfield at about $x/c = 0.65$. As can be seen from the results, the use of deformed side walls with the shock contour, rather than the actual simulation conditions, appears to be uncritical. The curves for the regular and off-design cases are aligning well.
From this limited case, it can be concluded that a single deformation can be used for testing over a variety of Mach numbers, as long as no shock occurs. Whether this trend holds for a change in geometric parameters, like the angle of attack, was not studied in this thesis and remains uncertain.

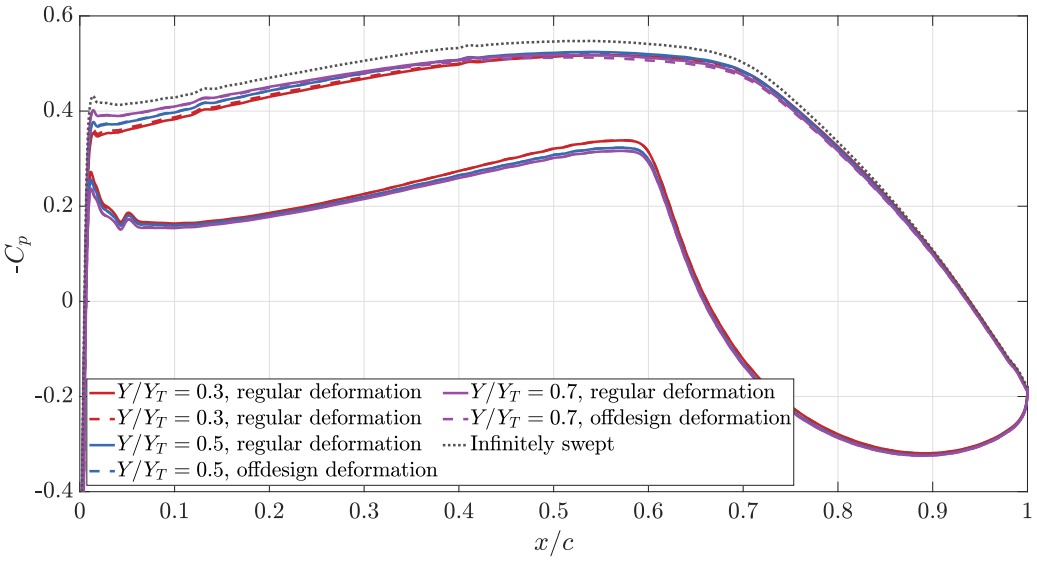

Figure 4.14: Pressure coefficient distribution extracted at different planes of the tunnel width. The off-design walls are shaped to match the case with a Mach number of 0.78. The simulations are performed for $\alpha = 0°$, $\Lambda = 15°$, $c = 150\,\text{mm}$, $Ma = 0.65$ and $Re = 7 \times 10^6$.

Figure 4.15 shows the pressure coefficient distributions for a simulation with a Mach number of $Ma = 0.78$, where in the infinitely swept wing case, a shock is present at $x/c \approx 0.65$. The regular deformation is based on a simulation with the matching parameters, whose results were discussed in Figure 4.12. The off-design deformation is based on the streamlines from a simulation with a Mach number of $Ma = 0.65$, where no shock is present in the infinite swept wing case. From the results at two spanwise planes, it can be found that the pressure for both deformations does not align. The deformation procedure can explain this mismatch. Neither the deformation from the original nor the off-design conditions represents the geometry of a streamline with an abrupt change in shape due to a shock. A first reason for this is the choice of the streamline closest to the wing, which is located at $Z = 0.06\,\text{m}$. At this location, the flowfield is already different from what it would be near the wing. Secondly, the deformation in TAU can only follow continuous shapes and can thus only approximate locations with a sharp change in direction. The difference to the infinitely swept wing conditions shown in Figure 4.12 and the differences between two different deformations shown in Figure 4.15 make it clear that for a presence of shocks in the test section,

a closer representation of the deformation than performed in this thesis is necessary to yield a flowfield where the strength and location of the shock align with infinite swept conditions. It is highly important to use tailored deformations for cases with shocks in the flowfield and not to use deformations at off-design conditions.

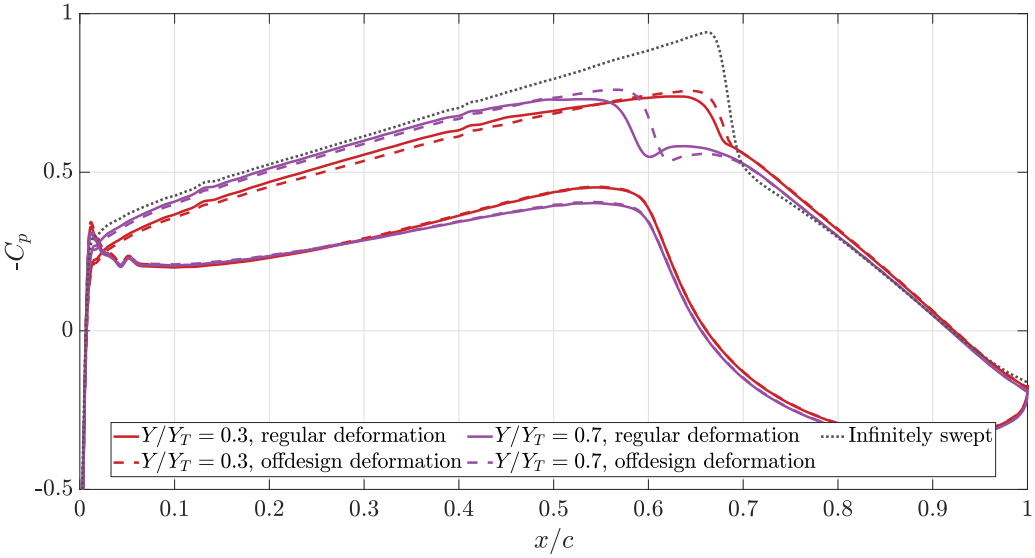

Figure 4.15: Pressure coefficient distribution extracted at different planes of the tunnel width. The deformed walls are shaped to match the results presented in Figure 4.12. The off-design walls are deformed to match the case with a Mach number of 0.65. The simulations are performed for $\alpha = 0°$, $\Lambda = 15°$, $c = 150\,\text{mm}$, $Ma = 0.78$ and $Re = 7 \times 10^6$.

4.3. Results with Deformation of Viscous Side Walls and Horizontal Walls

The preceding sections have shown results based on the deformation of the side walls of Domain 1 with extended horizontal walls, as shown in Figure 2.8a. By that, an isolated study of the vertical wall's effects was possible. In this section, a combination of side and horizontal walls is implemented, utilizing Domain 2, as shown in Figure 2.8b. Therefore, the side walls are deformed using the same procedure as was applied to Domain 1. The horizontal walls are deformed based on a streamline that is applied to fit the midplane of the tunnel. As shown in Section 3.2, this results in a flowfield that is not ideally suited for all spanwise locations in the tunnel. Nevertheless, this is inevitable because the horizontal walls in the KRG can only be adapted in two dimensions.

Figure 4.16 shows results for a simulation performed on Domain 1 and on Domain 2 with two-dimensionally deformed horizontal walls for the baseline parameter combination in this thesis. Three different spanwise planes are compared. As expected, the difference for the suction side is minor for the midplanes of the test section compared to infinite swept wing conditions and grows towards the tunnel walls. For the pressure side, the results from simulations based on Domain 2 overlap almost entirely with each other in the region of a favorable pressure gradient. Equally to what was found in Section 3.2, the results for Domain 2 feature a much higher spanwise homogeneity than the results for Domain 1. Specifically, the RMSE for the pressure coefficients between the 30 and 70 percent planes is reduced from 2.26% to 1.20% for the suction side and from 1.61% to 1.02% for the pressure side when using Domain 2 instead of Domain 1. The difference to the infinite swept wing case is not significantly altered for the suction surface, but increased for the pressure surface.

It can be concluded that for subsonic conditions, the flow homogeneity is increased when using Domain 2 with two-dimensionally deformed horizontal walls instead of Domain 1. This is contrary to what is expected, as additional walls constraining the flow, not as in the unbounded case, should yield flow conditions deviating more from the infinite swept wing than for the less bounded case, as is the case for Domain 1. The increase in spanwise homogeneity can be attributed to an increase in flow velocity in the

vicinity of the wing, which forces the flow to straighten and thereby enhances its homogeneity. It remains uncertain whether this effect is reproducible for other combinations of geometric parameters. In contrast to the results shown for the 10 and 90 percent planes in Figure 4.1, the region of the favorable and adverse pressure gradient does not change significantly.

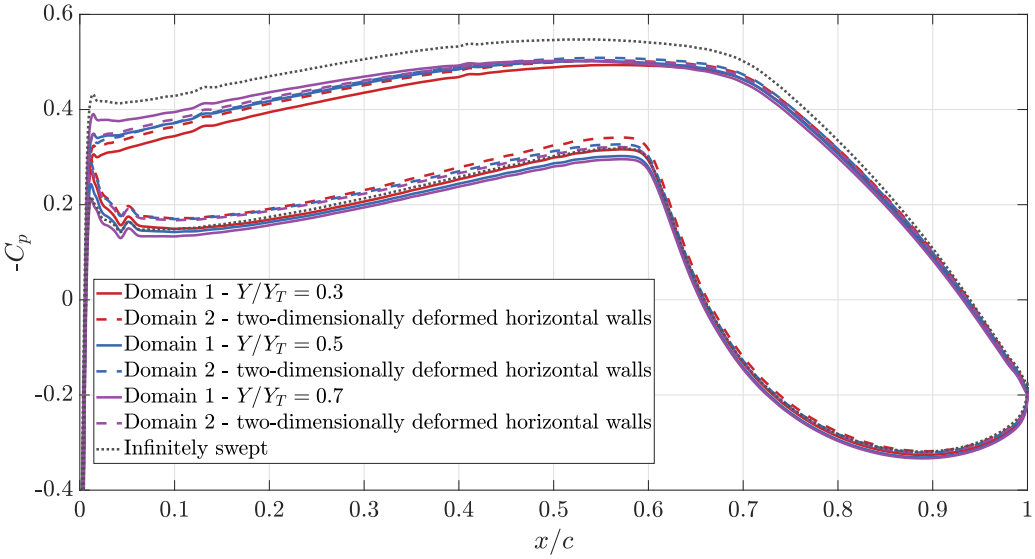

Figure 4.16: Pressure coefficient distribution extracted at different spanwise planes of the tunnel width. The two-dimensional deformation of the horizontal walls for Domain 2 follows the midplane of the tunnel. The simulations are performed for $\alpha = 0°$, $\Lambda = 15°$, $c = 150\,\text{mm}$, $Ma = 0.65$ and $Re = 7 \times 10^6$.

Figure 4.17 shows the plot for the transonic Mach number. It can be observed that the pressure coefficients align slightly more closely with the infinite swept conditions for the pressure side when using Domain 2, which features two-dimensionally deformed horizontal walls, rather than Domain 1. However, the flowfield for the suction side of the wing differs significantly between the two domains. When using Domain 2, the shock is almost eliminated completely, which, as already explained in Section 4.2.5, is caused by the interaction of the flow and the shock with the walls of the tunnel. However, for the favorable pressure gradient, as shown in the case with a subsonic Mach number, the spanwise homogeneity is increased. The reasons for this behavior are thought to be the same as for the previous case.

Concluding, the region of a favorable pressure gradient is increased in its homogeneity, whereas the location and strength deviate even further from infinite swept wing conditions when using Domain 2 with two-dimensionally deformed upper and lower walls instead of Domain 1.

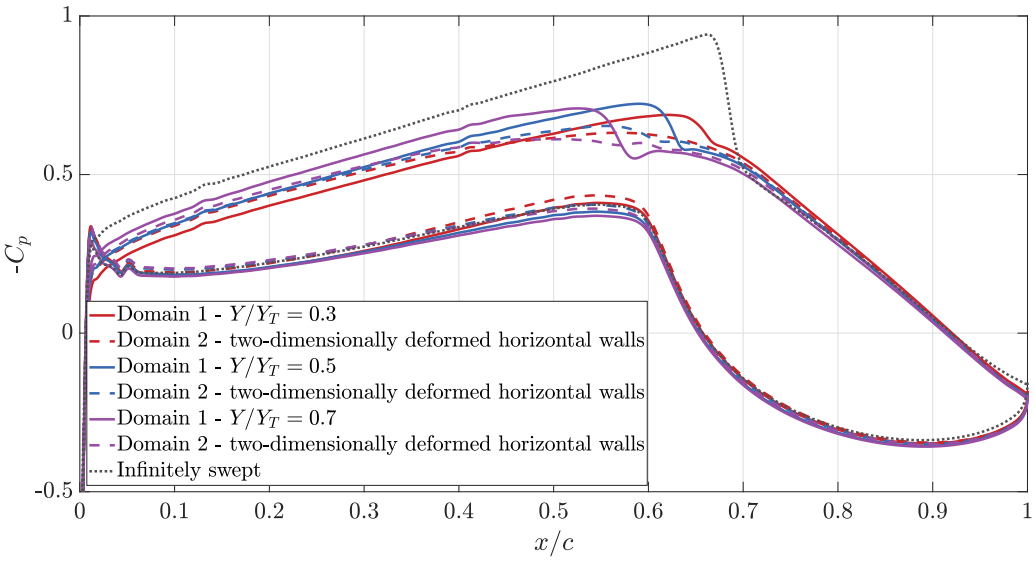

Figure 4.17: Pressure coefficient distribution extracted at different spanwise planes of the tunnel. The two-dimensional deformation of the horizontal walls for Domain 2 follows the midplane of the tunnel. The simulations are performed for $\alpha = 0°$, $\Lambda = 15°$, $c = 150\,\text{mm}$, $Ma = 0.78$ and $Re = 7 \times 10^6$.

4.4. Results for a Rotated Wing

Section 4.1 and Section 4.2 have shown that a proper deformation of the side walls can reduce the influence of the walls on the flowfield significantly. Spanwise, a more homogeneous flowfield can be established, which makes it easier to approach infinitely swept wing conditions. Nevertheless, this deformation is a complicated procedure that requires the manufacturing of so-called liners, which are inserted into the tunnel's test section to enable the straight walls to take the shape needed for the deformation. Hence, this section briefly explores another possibility to reduce the influence of the side walls without adding contoured liners to the test section.

One possible way to reduce the effort of producing and installing deformed side walls is to use adaptive horizontal tunnel walls as a means to mitigate the flow inhomogeneities introduced by the sweep angle of the model. Therefore, the possibility of rotating the wing in the test section is explored. The wing is rotated by 90 degrees around the X-axis, so that the leading edge is no longer oriented in the X-Y plane but in the X-Z plane. The setup is shown in Figure 4.18. The idea is that the horizontal walls reduce the spanwise inhomogeneities, while the side walls will not negatively impact the flowfield. This is more likely the case for the non-rotated wing, as the cross-section of the tunnel is not quadratic; hence, the distance of the tunnel walls to the wing's surface is increased by rotating the wing. Still, it is essential to consider how to mount the wing on the adaptive horizontal walls instead of the straight vertical walls. One possibility is to mount the wing on a rake and place it in the tunnel in a way that it does not touch the horizontal walls. In this case, it is essential to consider how to close the gaps between the model and the horizontal walls or to assess the impact of these gaps on the flowfield if they cannot be eliminated.

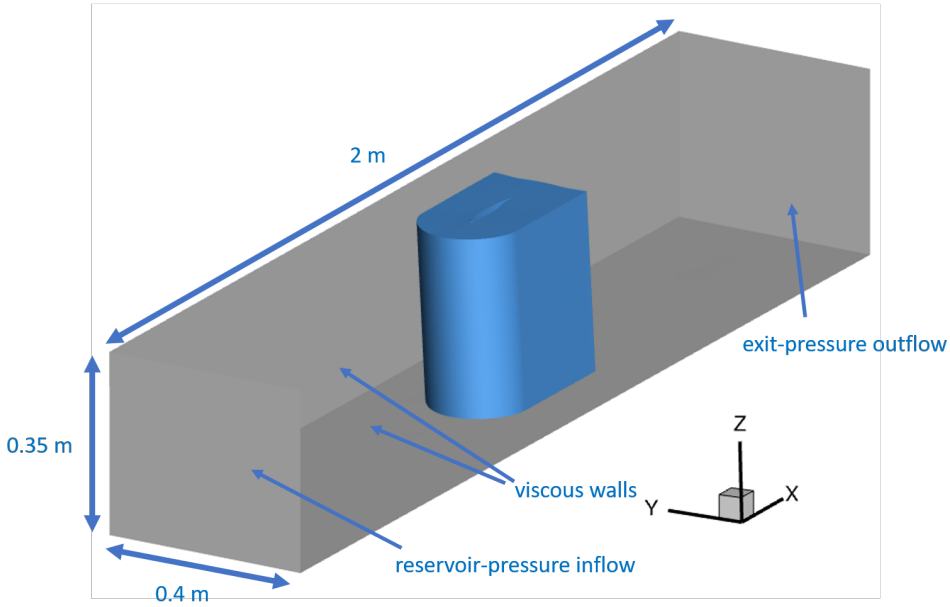

Figure 4.18: Computational domain used for the simulations with the rotated wing. The horizontal walls can be deformed two-dimensionally, and the vertical walls are straight.

Figure 4.19 shows the pressure coefficient distributions for different spanwise planes for two cases compared to the infinitely swept wing conditions. The computational domain shown in Figure 4.18 is used for the simulations with the rotated wing. Domain 2, as shown in Figure 2.8b, is used for simulations with straight side walls and two-dimensionally deformed horizontal walls. In both cases, the side walls remain straight, while the horizontal walls are deformed in a two-dimensional manner. It can be observed that the RMSE of the pressure coefficient distributions between the 30 percent and 70 percent planes for the case with the rotated wing is 3.45% for the suction side and 2.33% for the pressure side. For the case with straight side walls and deformed horizontal walls, these percentages are 3.28% and 2.36%, respectively. Hence, achieving flow conditions with a larger spanwise homogeneity is not possible when the wing is rotated. However, the difference to infinitely swept conditions is reduced when the wing is rotated. The root mean square error of the pressure coefficient at the midplane compared to the infinitely swept wing conditions is 3.52% for the suction side and 1.21% for the pressure side. In contrast, these values are 5.96% and 1.85%, respectively, for the case with the original wing placement. This indicates that the spanwise length of roughly constant flow conditions remains essentially unchanged, but the difference to the infinitely swept wing conditions is significantly reduced when the wing is rotated in the test section. Thus, when a small width of the test section is enough to measure the determined quantities and an alignment with infinitely swept conditions is of higher interest, rotating the wing may result in significantly improved measurement data. The spanwise homogeneity is most likely not increased because the deformation in the rotated case is based on the streamline located at $Z = 0.06\,\mathrm{m}$ and thus only two-dimensional. However, it remains unclear why conditions closer to the infinite swept wing can be achieved, although the side walls are not deformed.

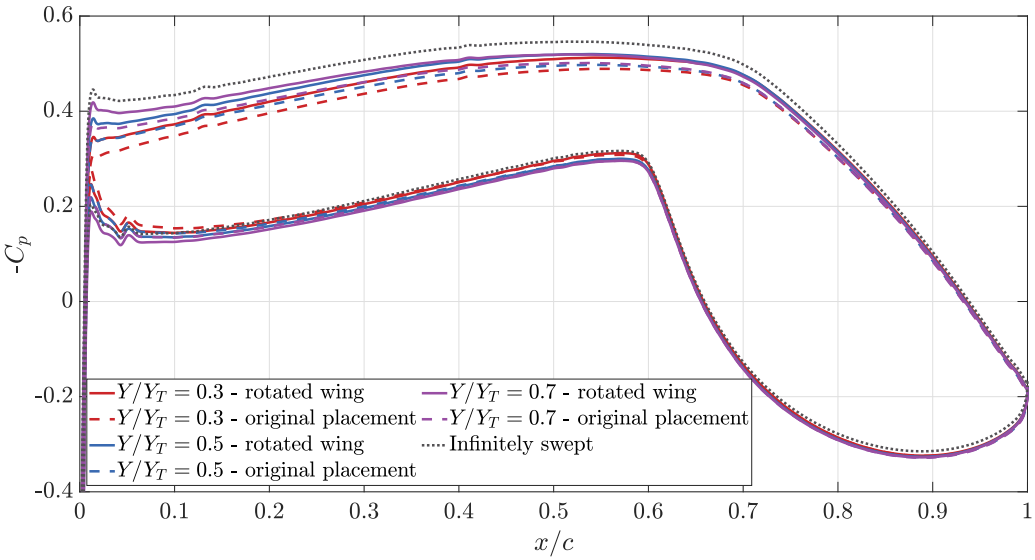

Figure 4.19: Pressure coefficient distribution extracted at different spanwise planes of the tunnel width. The deformation of the rotated wing follows the domain shown in Figure 4.18. The deformation of the horizontal walls for the second domain follows the midplane of the tunnel. The simulations are performed for α=0°, Λ=15°, c=100 mm, Ma=0.65 and Re=7e6.

Figure 4.20 shows the pressure coefficient distributions at different spanwise planes compared to the infinitely swept wing conditions. In contrast to the previous plot, this figure shows the rotated wing compared to a simulation based on Domain 2, where the side walls are deformed three-dimensionally and the horizontal walls are deformed two-dimensionally. It is found that the RMSE between the pressure coefficient distributions of the infinitely swept conditions and the midplane of the tunnel is 3.52% for the suction side and 1.21% for the pressure side if the wing is rotated. For the case with all walls deformed, these percentages increase to 4.07% and 1.98%. This effect is counterintuitive, as the deformed walls always showed a better alignment with the infinitely swept wing conditions than the undeformed cases in Section 4.2. Nevertheless, it should be noted that the RMSE of the pressure coefficient between the 30 percent and 70 percent planes is reduced from 3.45% for the suction side and 2.33% for the pressure side in the case of the rotated wing to 1.80% and 1.58% for the case with all walls deformed. That shows that the flow conditions with all walls deformed feature a larger spanwise section with constant flow conditions than simply rotating the wing in the current test section setup. The closer alignment to the infinitely swept wing conditions in the case where the wing is rotated may be due to an inaccurate deformation procedure. Based on the results in Section 4.2 it is not considered realistic that undeformed walls achieve conditions closer to the infinitely swept wing conditions than a deformation based on the inviscid streamlines of the infinitely swept simulations would.

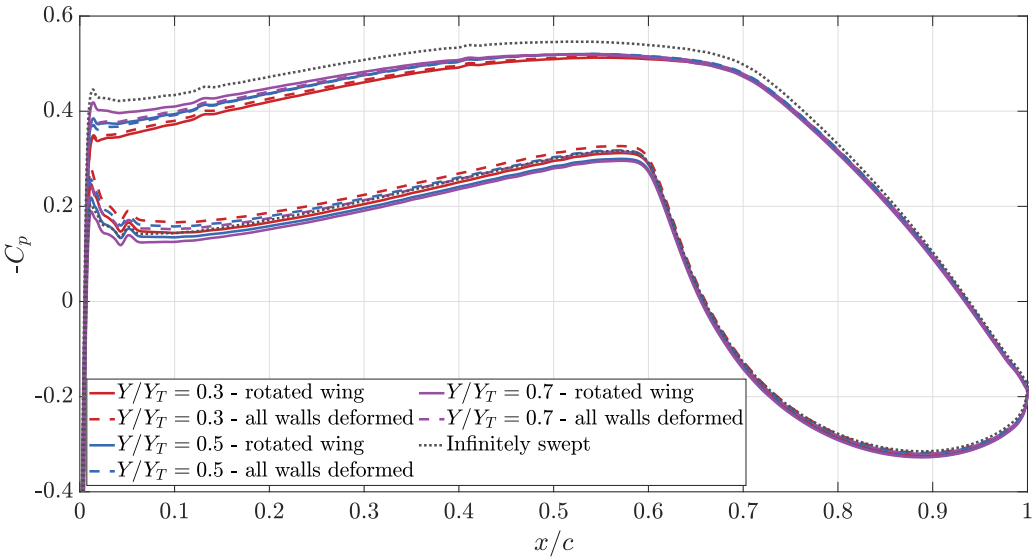

Figure 4.20: Pressure coefficient distribution extracted at different spanwise planes of the tunnel width. The deformation of the rotated wing follows the domain shown in Figure 4.18. The deformation of all walls is performed for the second domain. The simulations are performed for α=0°, Λ=15°, c=100 mm, Ma=0.65 and Re=7e6.

5

Conclusion and Recommendations

This chapter draws conclusions from the work performed in this thesis, followed by recommendations for future work.

5.1. Conclusion

This thesis investigated the aerodynamic effects of test section vertical walls on the spanwise homogeneity of the flow with swept-wing configurations in a transonic, high-Reynolds-number facility, the Cryogenic Ludwieg Tube Göttingen (KRG). By using Reynolds-Averaged Navier-Stokes (RANS) simulations with the DLR TAU code, this work has provided a quantitative assessment of how wall interference affects flow uniformity and shock structures across the span of a finite swept wing. The computational setup employed overset grids to accurately resolve the wing geometry within the tunnel domain, enabling high flexibility in geometric variations. The Spalart–Allmaras turbulence model was used throughout the study to model turbulent effects while maintaining computational efficiency. For comparison, the $k-\omega$ model was used, which did not produce significantly different pressure distributions on the suction side of the wing, nor did it reveal significant differences in the region of separated flow. Mesh deformation techniques based on radial basis functions were applied to adapt the tunnel walls according to streamlines that replicate unbounded flow conditions. Spatial and temporal grid convergence studies are performed, and the results of simulations with unswept wings are compared to those of previous numerical work by Köhler (2023) to ensure verification of the work. Validation is performed by comparing simulations with unswept wings to experimental data gathered by Koch et al. (2008). The impact of flow parameters, such as angle of attack, sweep angle, chord length, and Mach number, was systematically analyzed across various domain configurations, including both deformed and undeformed tunnel wall setups. Comparisons to reference conditions, representing an infinitely swept wing, served as the benchmark for evaluating wall interference and the effectiveness of the mitigation strategies.

The numerical simulations carried out in this study have provided a detailed understanding of the aerodynamic influence of wind tunnel walls on swept-wing configurations under transonic conditions in the KRG. One of the most notable findings is the substantial impact of side walls on the development of spanwise flow. The root mean square error of a pressure coefficient distribution on the suction side of the wing at 10 percent of the tunnel width compared to infinitely swept wing conditions can be as high as 11.77% for the baseline parameter combination of this thesis, making accurate representations of the unbounded flowfield impossible. The presence of these walls introduces spanwise pressure gradients and flow reversal near the wing–wall junction. These phenomena are especially pronounced at high angles of attack and high sweep angles. The application of adaptive wall deformation is a highly effective strategy for mitigating these adverse wall effects. Deforming the vertical sidewalls based on inviscid streamlines substantially reduced the spanwise inhomogeneity of the pressure coefficient distribution and improved the flow's similarity to the idealized infinitely swept wing case. The root mean square error between the suction side's pressure coefficient distributions at 30 percent and 70 percent of the tunnel width were reduced from 4.17% to 2.27% when deforming the vertical tunnel walls for a simulation with $\alpha = 0°$, $\Lambda = 15°$, $c = 150\,\text{mm}$, $Ma = 0.65$, and $Re = 7e6$. This marks a significant improvement in flow homogeneity.

The influence of several key parameters was also systematically assessed. The sweep angle emerged as the dominant factor governing wall influences, with higher sweep angles increasing spanwise non-uniformity. One reason for the dominance of sweep can be found in the non-uniform blockage, as the

inboard and outboard walls are deformed based on the same streamline from the infinite swept wing case. A reduction in chord length has minor beneficial effects on flow uniformity, but it must be adapted with care to avoid eliminating the advantage of testing under cryogenic conditions, i.e., at high Reynolds numbers. Changes in Mach number influenced the strength and location of shocks and their interaction with the boundary layer, making an accurate representation of infinite swept wing conditions impossible for transonic Mach numbers. However, when only the region of a favorable pressure gradient is examined at this Mach number, the results align much closer to infinite swept wing conditions. An increase in the angle of attack significantly increases the region of flow separation, thereby making it challenging to achieve homogeneous conditions near the tunnel walls. Additional results indicate that using wall deformations at Mach numbers for which they are not designed can yield good results, provided the flowfield remains subsonic. This makes it easier to choose a deformation that can then be applied to multiple test points. Additionally, rotating the wing to utilize the longer side of the non-quadratic cross-section of the tunnel more efficiently and using the adaptive upper and lower walls as boundary for the wing can improve alignment with infinite swept wing conditions, but cannot enhance spanwise flow homogeneity.

While the numerical approach presented in this thesis has provided valuable insights into the influence of wind tunnel walls on swept-wing aerodynamics in transonic, high-Reynolds-number flows, several limitations inherent to the methodology must be acknowledged. First, the work was conducted using steady RANS simulations with the Spalart–Allmaras turbulence model. Although this approach offers a practical balance between computational cost and accuracy, it inherently relies on time-averaged quantities. Furthermore, the computational domain itself includes several geometric idealizations. While this work only models the test section of the KRG, the influence of the flow upstream and downstream of the test section was neglected. A significant influence on the results was the deformation procedure with the TAU deformation tool. Following this approach, only an approximation of the ideal deformation was provided. Especially for flows in the transonic regime, the accuracy of the results can be significantly improved when a perfect deformation is provided tailored for each flow condition.

While the discussion of the results is oriented towards achieving infinite swept wing conditions in the tunnel to simulate airfoil aerodynamics, the results can be interpreted differently when the focus is instead placed on investigating transition. In this case, it is possible to find a configuration that achieves a minimum of spanwise velocity variations, while at the same time achieving a suitable favorable pressure distribution over the wing that enables the study of CFI-driven transition. In this case, the flowfield does not need to be the same as in the infinite swept wing case, which is why this is not the focus of this work.

This thesis makes a significant contribution to the ongoing effort to improve the interpretability of transonic wind tunnel experiments involving swept-wing configurations in the KRG. Specifically, the work provides a comprehensive numerical investigation into the aerodynamic impact of wind tunnel walls and introduces practical strategies to mitigate these effects through domain-specific wall deformation. By demonstrating that carefully tailored wall geometries can effectively reproduce the flowfield of an unbounded, infinitely swept wing, the study provides a validated computational toolset for pre-test planning in swept-wing experiments. This approach can be readily applied to a variety of wind tunnel test sections beyond the Cryogenic Ludwieg Tube Göttingen (KRG), making the methodology broadly relevant for other transonic facilities.

5.2. Recommendations

The results of this study highlight the significant impact of wind tunnel wall interference on the aerodynamics of swept-wing configurations. While this thesis employed numerical simulations to evaluate and mitigate these effects, the ultimate goal is to translate these findings into improved experimental practices. The following recommendations are therefore directed toward future experimental wind tunnel testing, drawn directly from the conclusions of this work.

The most immediate recommendation is the experimental realization of wall deformation geometries derived from the simulations. Specifically, the wall contours optimized to match the streamlines of an unbounded flowfield should be used to fabricate removable wall liners for wind tunnel test sections, such as the Cryogenic Ludwieg Tube in Göttingen. The most promising results, characterized by a large amount of spanwise homogeneous flow and a low difference from infinitely swept conditions, are achieved for a specific combination of parameters. It is advised to use a small angle of attack, close to $\alpha = 0°$, to keep the difference to infinitely swept wing conditions small. Since the study has shown that the flowfield

with shocks is highly sensitive to the deformation of vertical and horizontal walls, freestream conditions should be chosen that do not result in shocks in the test section. If that cannot be avoided, it is advised to manufacture the liners precisely according to the streamlines of the infinitely swept wing case to keep the deviation from this ideal case small. Furthermore, reducing the chord length is an appropriate measure to increase the flow homogeneity, if possible, to still maintain the desired Reynolds numbers. Finally, the sweep angle has the most considerable effect on reducing spanwise flow inhomogeneities. Thus, it should be chosen as small as possible for a specific application. Sweep angles of up to $\Lambda = 25°$ seem to be reasonable when appropriate measures are taken to reduce the wall's influence. For example, the pressure coefficient of a case with $\alpha = 0°$, $\Lambda = 25°$, $c = 150\,\text{mm}$, $Ma = 0.65$, and $Re = 7 \times 10^6$ with deformed side walls and without horizontal walls, yields a RMSE between the midplane and the infinite swept wing of 3.57% for the suction side. In contrast, the same case with undeformed side walls and without horizontal walls yields a RMSE of 5.37%. This is an increase of over 50 percent. The RMSE between the 30 and 70 percent planes of the tunnel is 3.35% in the deformed case and 6.35% for the undeformed case, which is an increase of almost 90 percent.

Once implemented, the performance of deformed wall configurations must be validated experimentally. This should involve detailed flow diagnostics, including pressure-sensitive paint (PSP) and pressure taps for surface pressure distribution, as well as temperature-sensitive paint (TSP). These measurements are crucial for verifying that the intended reduction in flow distortion has been achieved and for enhancing numerical models used for test planning and post-processing. Given the central importance of laminar-to-turbulent transition in swept-wing aerodynamics and the fact that wall effects strongly influence boundary-layer development, it is recommended that future experiments incorporate transition-sensitive instrumentation and design methodologies to map transition locations and validate predictions.

In addition to the suggested experimental work, further numerical work can be performed to identify alternative options to reduce the influence of the test section walls on the spanwise flow homogeneity:
As the region of separated flow at the wall-wing junction decreases the spanwise flow homogeneity significantly, measures to reduce flow separation in the tunnel are likely to improve the flowfield. One such option is to place only a part of the wing inside the test section, either mounted on one of the walls or mounted on a boom, not touching the walls at all. Another option can be the suction or blowing of nitrogen through porous walls, which after a modification of the side walls could achieve.
Finally, especially when examining a transonic flowfield, it can be helpful to perform simulations with a more accurate deformation of the side walls, which can be achieved by not using the TAU deformation tool, to gain a better understanding of the improvements possible when employing an accurate deformation. This accurate deformation would also include considering the non-uniform blockage that emerges from the swept wing.

These recommendations provide a pathway for transforming the computational findings of this thesis into practical experimental methodologies. By implementing optimized wall geometries and customizing test section design for specific flow regimes, future wind tunnel campaigns can more faithfully reproduce real-flight conditions. This is especially critical for ongoing efforts in laminar flow control, where even minor discrepancies in flow uniformity can significantly impact transition behavior and, by extension, aerodynamic performance. By addressing wall interference, experimental data can achieve a higher standard of accuracy, directly supporting the development of next-generation, low-drag swept-wing designs.

References

Adler, A. (1947). *Effects of Combinations of Aspect Ratio and Sweepback at High Subsonic Mach Numbers*. Tech. rep. Langley Memorial Aeronautical Laboratory, Langley Field, Va.: National Advisory Committee for Aeronautics.

Advisory Group for Aerospace Research and Development (AGARD) (1992). *Special Course on Skin Friction Drag Reduction*. Tech. rep. AGARD Report No. 786. Neuilly-sur-Seine, France: NATO Science & Technology Organization.

Anderson, J.D. (1995). *Computational Fluid Dynamics*. Aeronautical and Aerospace Engineering. McGraw-Hill, Inc.

Anderson Jr., J.D. (2017). *Fundamentals of Aerodynamics.* Sixth Edition. McGraw-Hill Education. ISBN: 978-1-259-12991-9.

Barlow, Rae, and Pope (1999). *Low-Speed Wind Tunnel Testing*. Third Edition. New York: John Wiley & Sons.

Bippes, H. (1999). "Basic experiments on transition in three-dimensional boundary layers dominated by crossflow instability". In: *Progress in Aerospace Sciences* 35.4, pp. 363–412. DOI: 10.1016/S0376-0421(99)00002-0.

Birkemeyer, J. (1999). "Adapted Wind Tunnel Walls for a Swept Wing Experiment". In: *New Results in Numerical and Experimental Fluid Mechanics II*. Ed. by W. Nitsche H.-J. Heinemann R. Hilbig. Vol. 72. Notes on Numerical Fluid Mechanics. Vieweg, pp. 44–51.

Blasius, H. (1908). "Grenzschichten in Flüssigkeiten mit kleiner Reibung". PhD thesis. Universität Göttingen.

Boussinesq, J. (1903). *Theorie analytique de la chaleur mise en harmonie avec la thermodynamique et avec la theorie mecanique de la lumiere: Refroidissement et chauffage par rayonnement, conductibilite des tiges, lames et masses cristallines, courants de convection, theorie mecanique de la lumiere*. Paris: Gauthier-Villars.

Britcher, Colin and Landman (2023). *Wind Tunnel Test Techniques. Design and Use at Low and High Speeds with Statistical Engineering Applications*. Academic Press. ISBN: 978-0128180990.

Brodersen, O. (1999). "Das Netzgenerierungssystem MegaCads". In: *MEGAFLOW-Abschlusskolloquium, Braunschweig*.

de Boer, A., M.S. van der Schoot, and H. Bijl (2007). "Mesh deformation based on radial basis function interpolation". In: *Computers Structures* 85.11, pp. 784–795. DOI: https://doi.org/10.1016/j.compstruc.2007.01.013.

DLR (2024). *Technical Documentation of the DLR TAU-Code Release 2024.1.0*. Tech. rep. Institute of Aerodynamics and Flow Technology.

Eckert, M. (2023). *Ludwig Prandtl und die moderne Strömungsforschung*. Klassische Texte der Wissenschaft. Springer Spektrum. ISBN: 978-3-662-67461-1.

Egami, Y. et al. (2012). "Development of new two-component temperature-sensitive paint (TSP) for cryogenic testing". In: *Measurement Science and Technology* 23.11. DOI: 10.1088/0957-0233/23/11/115301.

Ferziger, J.H. and M. Peric (2002). *Computational Methods for Fluid Dynamics*. Third Edition. Springer-Verlag Berlin Heidelberg GmbH. ISBN: 978-3-540-42074-3.

Fischer, M.C. and R.L. Ash (1974). *A General Review of Concepts for Reducing Skin Friction, Including Recommendations for Future Studies*. Washington, D.C.

Ganzer, U. (1985). “A review of adaptive wall wind tunnels”. In: *Progress in Aerospace Sciences* 22.2, pp. 81–111. DOI: 10.1016/0376-0421(85)90007-7.

Ganzer, U., E. Stanewsky, and J. Ziemann (1984). “Sidewall Effects on Airfoil Tests”. In: *AIAA Journal*. DOI: 10.2514/3.48443.

Gibson, Soucheleau, and Rogers (2021). “BLADE - Natural Laminar Flow Flight Testing”. In: International Council of the Aeronautical Sciences. ISBN: 978-393218291-4.

Goethert, B.H. (1961). *Transonic Wind Tunnel Testing*. Bristol: Pergamon Press. ISBN: 978-0-521-66219-2.

Hansen, H. (2010). “Laminar flow technology - the Airbus view”. In: *Congress of the International Council of the Aeronautical Sciences*. 27th Congress of the International Council of the Aeronautical Sciences 2010, ICAS 2010, pp. 453–461. ISBN: 978-161782049-6 (ISBN).

Hirt, S.M. (2015). “Experimental study of fillets to reduce corner effects in an oblique shock-wave/boundary-layer interaction”. In: AIAA Paper 2015-1239. American Institute of Aeronautics and Astronautics Inc, AIAA. DOI: 10.2514/6.2015-1239.

Hoang, N.T.B. and B.V. Bui (2019). “Investigation of wind tunnel wall effect and wing-fuselage interference regarding the prediction of wing aerodynamics and its influence on the horizontal tail”. In: *Journal of Mechanical Science and Technology* 33.6, pp. 2737–2746. DOI: 10.1007/s12206-019-0520-x.

Johnson, R. (1951). *Minimum Drag Coefficient of Wings*. Tech. rep. RM-604. Santa Monica.

Joslin, R.D. (1998). “Aircraft laminar flow control”. In: *Annual Review of Fluid Mechanics*, pp. 1–29. DOI: 10.1146/annurev.fluid.30.1.1.

Koch, S. et al. (2008). *Analysis of transition experiments on the LV2F airfoil in the Cryogenic Ludwieg-Tube Göttingen DNW-KRG*. Tech. rep.

Köhler, P. (2023). “Numerische Untersuchung der Umströmung eines schiebenden Flügelmodells im Kryo-Rohrwindkanal Göttingen”. Master thesis. Leibniz Universität Hannover.

Liepmann, H.W. and D.M. Nosenchuck (1982). “Active control of laminar-turbulent transition”. In: *Journal of Fluid Mechanics* 118, pp. 201–204. DOI: 10.1017/S0022112082001037.

Malik, M.R. and D.M. Bushnell (2012). *Role of Computational Fluid Dynamics and Wind Tunnels in Aeronautics RD*. Tech. rep. NASA/TP-2012-217602. NASA Langley Research Center.

Meier, H.U. (2005). *Die Pfeilflügelentwicklung in Deutschland bis 1945*. First Edition. Bernard & Graefe. ISBN: 978-3-7637-6130-2.

Obert, E. (2009). *Aerodynamic Design of Transport Aircraft*. IOS Press. ISBN: 978-1586039707.

Pope, S.B. (2000). *Turbulent Flows*. Cambridge: Cambridge University Press. ISBN: 978-0-521-59125-6.

Prandtl, L. (1921). “Bemerkungen über die Entstehung der Turbulenz”. In: *ZAMM - Journal of Applied Mathematics and Mechanics / Zeitschrift für Angewandte Mathematik und Mechanik* 1.6, pp. 431–436.

Rius-Vidales, A.F. (2022). “Influence of a forward-facing step on crossflow instability and transition. An experimental study in a swept-wing boundary-layer.” PhD thesis. Delft University of Technology.

Rius-Vidales, A.F. and M. Kotsonis (2021). “Impact of a forward-facing step on the development of crossflow instability”. In: *Journal of Fluid Mechanics* 924. DOI: 10.1017/jfm.2021.497.

Rogers and Hall (1960). “An Introduction to the Flow about Plane Swept-back Wings at Transonic Speeds”. In: *The Journal of the Royal Aeronautical Society* 64.596, pp. 449–464. DOI: 10.1017/S0368393100073259.

Romano, D.G. et al. (2013). “Design and tests of wind-tunnel sidewalls for receptivity experiments on a swept wing”. In: *Applied Mechanics and Materials*, pp. 96–102. DOI: 10.4028/www.scientific.net/AMM.390.96.

Rosemann, H. (1995). *The Cryogenic Ludwieg-Tube Tunnel at Göttingen*. Tech. rep. R812. AGARD, Advisory Group for Aerospace Research & Development.

Ross, J. (2023). “Integration of CFD and Wind Tunnel Testing at NASA”. In: *AIAA SciTech Forum*. National Harbor, MD, USA.

Saric, W.S., J. Muylaert, and C. Dujarric (1999). *AGARD Advisory Report 319: Hypersonic Experimental and Computational Capability, Improvement and Validation. Volume I*.

Schlichting, H. and K. Gersten (2006). *Grenzschicht-Theorie*. Zehnte Auflage. Springer-Verlag Berlin Heidelberg. ISBN: 3-540-23004-1.

Serpieri, J. (2018). “Cross-Flow Instability: Flow diagnostics and control of swept wing boundary layers”. PhD thesis. Delft University of Technology. DOI: 10.4233/uuid:3dac1e78-fcc3-437f-9579-048b74439f55.

Shang, J.S. and W.L. Hankey (1977). “Numerical solution of the Navier-Stokes equations for a three-dimensional corner”. In: *AIAA Journal* 15.11, pp. 1575–1582. DOI: 10.2514/3.60824.

Spalart, P.R. and S.R. Allmaras (1992). “A One-Equation Turbulence Model for Aerodynamic Flows”. In: *Proceedings of the 30th Aerospace Sciences Meeting and Exhibit*. American Institute of Aeronautics and Astronautics (AIAA). Reno, NV.

Taylor, G.I. (1915). “Eddy motion in the atmosphere”. In: *Philosophical Transactions of the Royal Society of London. Series A, Containing Papers of a Mathematical or Physical Character* 215.523-537, pp. 1–26.

Torenbeek, E. (1982). *Synthesis of Subsonic Airplane Design*. Delft University Press. ISBN: 90-247-2724-3.

Van Ingen, J.L. (2008). “The eN method for transition prediction. Historical review of work at TU Delft”. In: AIAA paper 2008-3830. American Institute of Aeronautics and Astronautics Inc. DOI: 10.2514/6.2008-3830.

Vatsa, V.N. and B.W. Wedan (1989). “Effect of sidewall boundary layer on a wing in a wind tunnel”. In: *Journal of Aircraft* 26.2, pp. 157–161. ISSN: 00218669 (ISSN). DOI: 10.2514/3.45738.

Vos, R. and S. Farokhi (2015). *Introduction to Transonic Aerodynamics*. Springer Science+Business Media Dordrecht. ISBN: 978-94-017-9746-7.

Wassermann, P. and M. Kloker (2005). “Transition mechanisms in a three-dimensional boundary-layer flow with pressure-gradient changeover”. In: *Journal of Fluid Mechanics* 530, pp. 265–293. DOI: 10.1017/S0022112005003708.

Wendt, J.F. et al. (2009). *Computational fluid dynamics: An introduction*. Springer Berlin Heidelberg. ISBN: 978-354085055-7 (ISBN).

White, F.M. (1991). *Viscous Fluid Flow*. Second Edition. McGraw-Hill, Inc. ISBN: 0-07-069712-4.

A

TAU Solver Settings

A.1. Two-Dimensional Simulations

Depending on the case No174 and No015, the parameters are specified below, first listing the parameters for the No174 case, followed by the No015 case, separated by a forward slash.

- Reservoir-Pressure Inflow
  - Turbulent intensity: 0.05
  - Total pressure: 263660 / 319167.69
  - Total temperature: 190.47 / 257.22
- Exit-Pressure Outflow
  - Match measured pressure (0/1): 0
  - Matching adjustment factor [0,1]: 0.15
  - Matching iteration period: 2000
  - Matching iteration start: 20000
  - Measured pressure: 190197.99 / 217736.38
  - Measurement coordinates: 0.5 0 0
  - Exit pressure: 190197.99 / 217736.38
- Reference Values
  - Reference Mach number: 0.6993 / 0.7598
  - Reynolds number: 9.01×10^6 / 7.62×10^6
  - Reynolds length: 0.150
  - Grid scale: 1
  - Reference temperature: 173.5 / 230.6
  - Total temperature: 190.47 / 257.22
  - Total pressure: 263660 / 319167.69
- Settings
  - Use wall function (0/1): 1
  - Pressure switch weighting factor: 50 (reduced to 3 during the simulation)
  - Inviscid flux discretization type: Central
  - Central convective turbulence flux: Roe
  - Central dissipation scheme: Matrix dissipation
  - Relaxation solver: Backward Euler
  - Minimum artificial dissipation for acoustic waves: 0.2

  - Minimum artificial dissipation for velocity: 0.2
  - Reconstruction of gradients: Green Gauss
  - CFL number: 2.5
  - CFL number (large grad p): 1.8
  - CFL number (coarse grids): 1.8
  - Turbulence model version: SA / k-w (k-w model version: Menter SST.2003)
- Multigrid
  - MG description filename: v
  - Number of multigrid levels: 2
  - Number of MG-cycle levels: 2
  - Number of relaxation steps between MG-transfers: 4
  - Number of relaxation steps on coarsest grid level: 4
  - SG start up steps (fine grid): 1000

A.2. Three-Dimensional Simulations for Inviscid and Viscous Walls

- Reservoir-Pressure Inflow
  - Turbulent intensity: 0.05
  - Total pressure: 387417.14
  - Total temperature: 296.23
- Exit-Pressure Outflow
  - Match measured pressure (0/1): 0
  - Matching adjustment factor [0,1]: 0.15
  - Matching iteration period: 2000
  - Matching iteration start: 20000
  - Measured pressure: 291659
  - Measurement coordinates: 0.5 0 0
  - Exit pressure: 291659
- Reference Values
  - Reference Mach number: 0.65
  - Reynolds number: 7e6
  - Reynolds length: 0.150
  - Grid scale: 1
  - Reference temperature: 273.15
  - Total temperature: 296.23
  - Total pressure: 387417.14
- Settings
  - Use wall function (0/1): 1
  - Pressure switch weighting factor: 50 (reduced to 3 during the simulation)
  - Inviscid flux discretization type: Central
  - Central convective turbulence flux: Roe
  - Central dissipation scheme: Matrix dissipation
  - Relaxation solver: Backward Euler

  - Minimum artificial dissipation for acoustic waves: 0.2
  - Minimum artificial dissipation for velocity: 0.2
  - Reconstruction of gradients: Green Gauss
  - CFL number: 2
  - CFL number (large grad p): 1.5
  - CFL number (coarse grids): 1.5
  - Turbulence model version: SA
- Multigrid
  - MG description filename: v
  - Number of multigrid levels: 2
  - Number of MG-cycle levels: 2
  - Number of relaxation steps between MG-transfers: 4
  - Number of relaxation steps on coarsest grid level: 4
  - SG start up steps (fine grid): 1000